Morphological design of conjugated polymer thin films for charge transport and energy conversion

by

Anton W. Li

A dissertation submitted in partial fulfillment
of the requirements for the degree of
Doctor of Philosophy
(Materials Science and Engineering)
in the University of Michigan
2016

Doctoral Committee:

Professor Peter F. Green, Chair
Professor Jinsang Kim
Associate Professor Anish Tuteja
Associate Professor Zhaohui Zhong

ACKNOWLEDGMENTS

It is hard to believe that over four years have passed since I first arrived in Ann Arbor to begin my graduate studies. Reflecting upon the road that has led to this point, it becomes all too clear that I would never have made it this far without the help and support of others.

First and foremost, I would like to express my deepest gratitude to my thesis advisor, Professor Peter F. Green. His scientific knowledge and physical intuition has been an invaluable resource in times when I struggled with analyzing or interpreting results. Although he guides and inspires overall directions and approaches to laboratory research, he has always encouraged students to explore interesting problems and chart their own course. His style of mentorship has helped me to grow as an independent researcher and develop critical thinking skills that will be indispensable in any career. I would also like to thank the other members of my dissertation, Professors Jinsang Kim, Anish Tuteja, and Zhaohui Zhong. In addition to teaching graduate courses covering very interesting and highly relevant topics on polymers and solid-state physics, they have provided insightful critique and helpful suggestions for my research.

A large part of my success rests upon the shoulders of former and current members of the Green research group. In particular, my colleagues Dr. Bingyuan Huang, Jojo Amonoo, and Ban X. Dong deserve special recognition, as we worked together as a team on several inter-related projects, combining our skills and expertise to generate several high-impact research findings. Needless to say, all members of the Green group have contributed indirectly to my work, through discussions during weekly lab meetings as well as simple day-to-day interactions; for this, I owe

many thanks to Dr. Emmanouil Glynos, Dr. Aaron Tan, Dr. Chelsea Chen, Dr. Jenny Kim, Dr. Bradley Frieberg, Dr. Hengxi Yang, Dr. Peter Chung, Junnan Zhao, Kyle Johnson, Ravi Sharma, and Jill Wenderott.

One of the greatest assets of the University of Michigan is its large and diverse community and the strong spirit of multidisciplinary collaboration. For a large portion of my degree, the Center for Solar and Thermal Energy Conversion (CSTEC) provided a way for researchers from different departments and groups to come together and forge fruitful partnerships. Thus, besides being the primary funding source of my research, I am grateful to CSTEC for giving me the opportunity to engage with fellow graduate students from different disciplines and backgrounds. I would also like to acknowledge and thank the MCubed program for creating another avenue for interdisciplinary collaboration, funding joint research with members of Professor Kim's and Professor Theodore Goodson's research groups.

As any graduate student will tell you, research can become very tiresome and frustrating, and times we need diversions that remind us that life goes on in the world outside the laboratory. Because of this, I am extremely grateful for the friendships I have formed with my colleagues and other peers. I also want to express special thanks to the wonderful owners and staff of The Lunch Room, Juicy Kitchen, El Harissa, Songbird Café, Exotic Bakeries, and other locally-operated eateries who have provided me with amazing food, drink, and friendly company.

Last but not least, I would like to express my utmost appreciation for the unfaltering love and support from my family: my mother and father, Mei Yong and Shiping Li, and my now not-so-little brother, Edward Li. Despite being hundreds of miles away, their constant encouragement gave me the strength to plow ahead in spite of challenges and setbacks.

TABLE OF CONTENTS

LIST OF TABLES

LIST OF FIGURES

LIST OF APPENDICES

ABSTRACT

Conjugated polymers hold great promise as a versatile class of materials for a wide range of optoelectronic applications, but unlocking their full potential requires deeper understanding of relationships between their complex structure and physical properties at multiple length scales. For polymer/fullerene blends used for thin film photovoltaics, controlling the "bulk heterojunction" morphology is of paramount importance to solar cell performance. By incorporating a small amount of an interfacially-active copolymer, the nano-scale phase separation was enhanced, generating more favorable pathways for transport and collection of photo-generated charges. The copolymer also enriched the region near the electrode, shifting the interfacial work function and suppressing surface recombination. Together these effects yielded up to a 20% increase in power conversion efficiencies.

Even as pure components, conjugated polymers exhibit very diverse morphologies. By aligning the polymer chains, it is possible to borrow their molecular anisotropy and exploit it at the macroscopic level. Highly-aligned films were fabricated consisting of fibers with uniaxial orientation over centimeter-scale regions, and it was experimentally demonstrated that chain alignment could enable photo-excited charges to migrate distances over 400 μm. The measured anisotropy of optical properties, photocurrent migration, and carrier mobilities are all correlated to the morphology of the aligned films. As a contrasting yet complementary study, the effect of structural disorder on different transport mechanisms/regimes was investigated. To this end, a novel vacuum deposition technique was used to fabricate conjugated polymer films with unique

globular morphologies. Despite being more disordered, vacuum-deposited thin film transistors (8.3×10^{-3} $cm^2V^{-1}s^{-1}$) exhibited comparable in-plane mobilities to spin-cast analogues (5.5×10^{-3} $cm^2V^{-1}s^{-1}$). Their out-of-plane mobilities, on the other hand, were nearly an order of magnitude lower. The seemingly contradictory results were rationalized in terms of the morphologies and carrier densities at interfaces versus within the bulk.

Through different approaches to exploring various aspects of structure-property relationships in conjugated polymers, the work presented in this dissertation yields important insights for the future design and application of these materials.

CHAPTER I:
INTRODUCTION

Conjugated polymers are a class of organic (carbon-based) semiconductors of great scientific and technological interest. Although their electrical conductivities are generally inferior to their inorganic counterparts, they possess several key advantages such as mechanical flexibility, low weight, solution-processibility, and highly-tunable optoelectronic properties. These unique combinations of characteristics make conjugated polymers highly attractive candidate materials for a wide range of applications, spanning photovoltaics, transistors, sensors, and more. Beyond their chemistry, the properties of conjugated polymers, and blends/nanocomposites thereof, are critically dependent on their morphologies. Unlike crystalline inorganic semiconductors, whose structure consists of individual atoms arranged in a periodic lattice of long-range order, conjugated polymers exist as distinct molecular entities in the form of long chains with inherently anisotropic characteristics that depend on the orientation in relation to the backbone and attached functional groups. Locally, these chains may pack into regions with well-defined crystal lattices, but at larger length scales, conjugated polymers are semicrystalline, consisting of a mixture of well-ordered crystallites and amorphous regions of varying degrees of structural disorder. These complex, heterogeneous morphologies give rise to correspondingly complex phenomena and behavior.

1.1. CHARGE CONDUCTION IN CONJUGATED POLYMERS

The mechanisms of charge transport in organic semiconductors, including conjugated polymers, are fundamentally different from their crystalline inorganic counterparts. Because they exist as individual atoms are arranged in a lattice with long-range periodic order, crystalline inorganic semiconductors possess well-defined wave functions and energy band structures. Thus, charge transport and other physical properties are uniform and relatively isotropic. As previously mentioned, the molecular nature of polymers gives rise to inherent anisotropy which can be described in terms of relative orientations to the polymer chain as shown in **Figure 1.1**: parallel to the backbone (c-axis), perpendicular to the backbone, but coplanar with the aromatic cores (a-axis), or in the orthogonal to both (b-axis). The defining feature of conjugated polymers is the presence of a continuous series of sp^2-hybridized carbon atoms along the polymer backbone (sometimes represented in chemical drawings as backbones possessing alternating double bonds). The three sp^2 hybrid orbitals form covalent σ bonds with neighboring atoms, but the remaining unhybridized p_z orbital forms a weaker π bond with adjacent sp^2 carbon atoms. Whereas the electrons in the sp^2 orbitals are "locked" into directional σ bonds with neighboring atoms, those within the p_z orbitals can delocalize and form π bonds with electrons in parallel p_z orbitals of adjacent atoms. On a segment of a conjugated polymer where the backbone is straight and free of twists/distortions, electrons can delocalize from one end to the other through the uninterrupted sequence of p_z orbitals, thereby enabling charge conduction. This mode of charge conduction along an individual chain, henceforth referred to as "intrachain" transport, is the most rapid and efficient conduction mechanism in conjugated polymers.

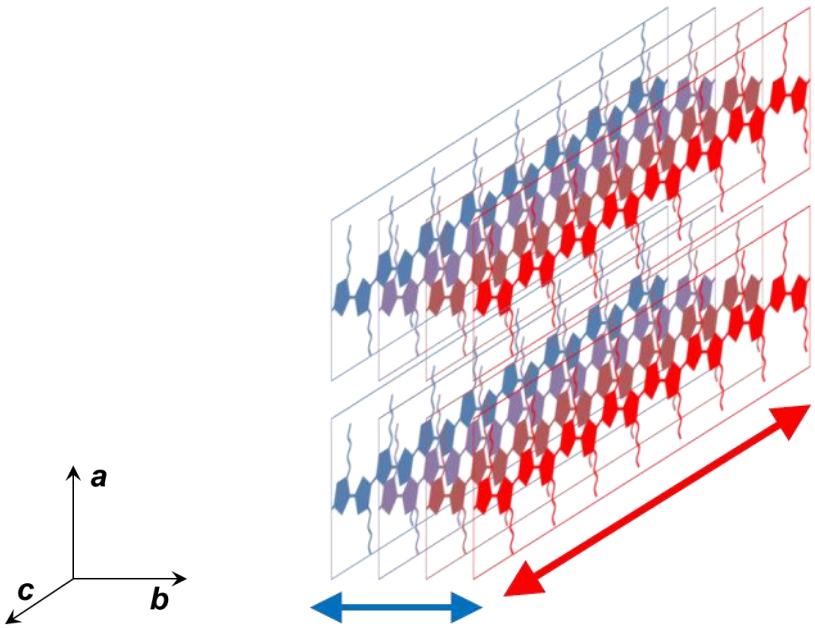

Figure 1.1 Diagram of a crystalline polyalkylthiophene with conventional lattice directions defined. Intrachain transport, indicated by the red arrows occurs along the backbone direction (c-axis), while interchain transport occurs in the π-stacking direction, indicated by the blue arrows (b-axis). The alkyl side chains prevent carrier transport in the lamellar stacking direction (a-axis).

Charges can also hop between different chains. If two adjacent, closely-packed chains are oriented with their p_z orbitals parallel and pointing towards each other, the orbitals may overlap and enable charges to hop from one chain to the other. Because the distance is larger (compared to adjacent carbon atoms on the same molecule), the electronic coupling is weaker and thus "interchain" conduction is less efficient than the intrachain mechanism. The electronic coupling can be improved with closer packing of chains. Transport in the third direction along the a-axis (sometimes called the lamellar direction) is virtually nonexistent; the bulky side chains or other functional groups are generally not conjugated, and thus there are no electronically-coupled pathways between the conjugated backbones.[1]

1.2. ENERGY CONVERSION PRINCIPLES FOR POLYMER SOLAR CELLS

Owing to their low dielectric constant and the localized nature of their molecular orbitals, conjugated polymers and other organic semiconductors do not immediately create free carriers upon photoexcitation; instead, photon absorption initially forms electrostatically-bound electron-hole pairs known as excitons. At room temperature, thermal energy is insufficient to overcome the exciton binding energy; in order to dissociate the electron and hole into free carriers, additional driving force is required. This can be accomplished by incorporating a second material with suitable offsets in molecular orbital energy levels, such that electron transfer from one species to the other is favored while hole transfer is not.[2] The primary light-absorbing species responsible for exciton formation is called the "donor", and the species to which the electron transfers is called the "acceptor". In the work presented in this dissertation, the donor is a conjugated polymer and the acceptor is a modified fullerene small molecule. Although there has been growing interest in all-polymer and all-small molecule blends for solar cells, devices based on polymer/fullerene blends continue to exhibit some of the highest power conversion efficiencies among organic photovoltaics.

The photon-to-electron conversion efficiency η of an organic photovoltaic cell is called the external quantum efficiency (EQE), defined for a specific wavelength of light (λ), and is the product of the photon absorption efficiency (η_{abs}), exciton dissociation efficiency (η_{diss}), and charge collection efficiency (η_{cc}):

$$\eta_{\mathrm{EQE}}(\lambda) = \eta_{\mathrm{abs}}\eta_{\mathrm{diss}}\eta_{\mathrm{cc}}$$

The absorption efficiency is largely determined by the electronic bandgap of the light-absorbing species, which is largely based on chemistry and functional groups. Integrating the EQE over the entire solar spectrum yields the overall power conversion efficiency (PCE) of the device.

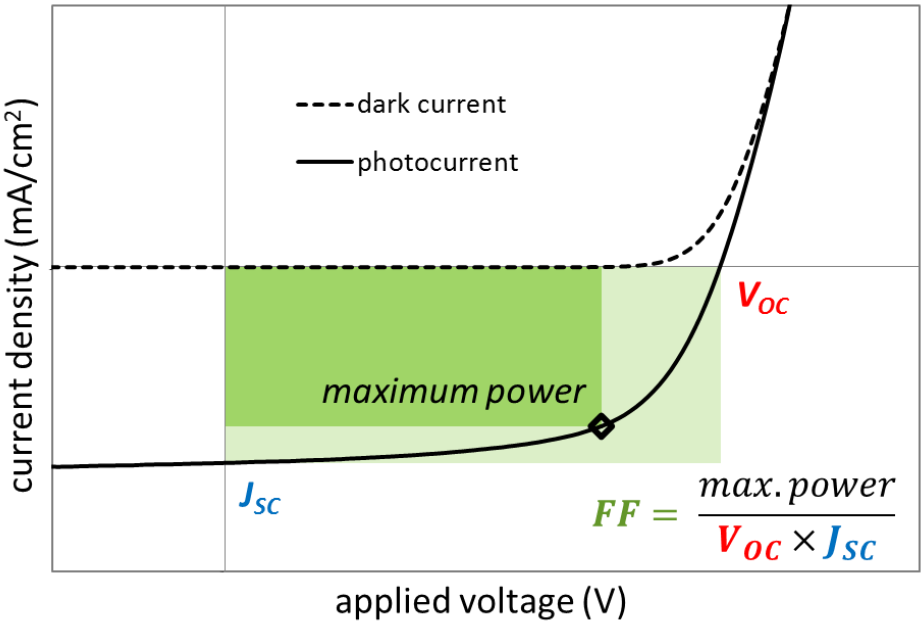

Figure 1.2 Examples of *J*-*V* curves in the dark and under illumination for a typical organic solar cell. Also illustrated are the macroscopic parameters open-circuit voltage (V_{OC}), short-circuit current (J_{SC}), fill factor (FF), and power conversion efficiencies (PCE), in relation to the shape of the *J*-*V* curve.

The basic electrical characterization for solar cells is measuring the current density (*J*) while performing a sweep of applied voltage (*V*). In the dark, a photovoltaic cell behaves as a diode, blocking current until a certain forward bias has been met; under illumination, there will be reverse photocurrent due to the photovoltaic effect until sufficient forward bias reverses the flow. **Figure 1.2** shows *J*-*V* curves for a typical organic solar cell, with points labelled for the open-circuit voltage (V_{OC}), short-circuit current (J_{SC}), and fill factor (FF). Although these macroscopic observables are convoluted products of a number of physical processes, they provide easy metrics for comparison between devices. For a given donor/acceptor blend composition and device architecture, the V_{OC} is usually relatively constant, determined by the HOMO-LUMO offsets between donor and acceptor and the work functions of the electrodes. The J_{SC} is influenced by virtually all steps of photon-to-electron conversion (η_{abs}, η_{diss}, and η_{cc}).

Power output is the product of voltage and current, with the maximum power point on the *J*-*V* curve typically found near the V_{OC}. The FF describes the "squareness" of the *J*-*V* curve; a device exhibiting ideal photodiode characteristics (FF approaching 100%) would maintain reverse photocurrent very close to the J_{SC} with increasing forward bias until abruptly switching to forward direction at V_{OC}.

The basic device architecture for thin film photovoltaics consists of the photoactive layer sandwiched between a two electrodes (one of which must be transparent), but the detailed configuration of the photoactive layer itself can vary. Perhaps the simplest to understand and model is the planar heterojunction configuration, in which the donor and acceptor are kept as two separate layers with a sharp interface (a bilayer), in some ways an analogue to the p-n junction in inorganic semiconductor devices. In this configuration, photons are absorbed in the donor layer, creating excitons which must diffuse to the heterojunction in order to be dissociated at the donor/acceptor interface. Since only those excitons generated within ~10 nm of the planar heterojunction have a chance to be dissociated at the interface, creating a thicker layer to increase η_{abs} would fail to significantly improve photocurrent generation due to a corresponding decrease in η_{diss}. The planar heterojunction configuration does benefit from a high η_{cc}, since separated electrons/holes can easily migrate to the cathode/anode through the pure component acceptor/donor layers.

To address the sub-optimal exciton dissociation efficiency of planar heterojunction devices, the "bulk heterojunction" (BHJ) configuration has been widely adopted for polymer solar cells.[3–5] The BHJ is a relatively disordered morphology consisting of a partially phase-separated blend of donor and acceptor components forming interpenetrated networks of nano-scale domains. Provided that the characteristic domain sizes are on the order of the exciton

diffusion length (~10 nm), an exciton generated anywhere within the active layer has a high probability of reaching a donor/acceptor interface, yielding a very high η_{diss}. This allows the creation of thicker active layers to improve light harvesting and raise η_{abs}. A drawback of the BHJ device configuration is that the prevalence of interfaces throughout the active layer provides many opportunities for free charges to encounter each other and recombine, thereby limiting η_{cc}.[6] Intermixing of donor and acceptor species also typically yields a higher degree of disorder compared to the individual pure components, resulting in the formation of more deeply-trapped localized carrier states which further hinder charge transport.

Therefore, tailoring BHJ morphology is a delicate balancing act of maintaining a large donor/acceptor interfacial area (to ensure high η_{diss}), while driving some degree of phase separation to form efficient carrier transport pathways (to increase η_{cc}). Subtle changes in processing conditions can yield very different morphologies, possessing domain sizes and phase purities, which yield very different device characteristics as shown in **Figure 1.3**.[7] Beyond the macroscopic parameters extracted from *J*-*V* curves, spectroscopic and advanced electrical measurements can provide more physical parameters such as carrier mobilities, densities, and recombination rates. These results confirm that more highly-mixed morphologies can generate very high initial carrier densities due to efficient exciton dissociation, but carriers undergo very rapid recombination resulting in poor photocurrent density and overall power conversion efficiency. Post-processing treatments (such as thermal or supercritical CO_2 annealing)[8] induces phase-separation and formation of more distinctive domains with higher phase purities. As a result, fewer free carriers are created from exciton dissociation, but the improved transport network for carrier collection greatly reduces recombination losses, which ultimately more than compensates for the decrease in initial carrier densities.

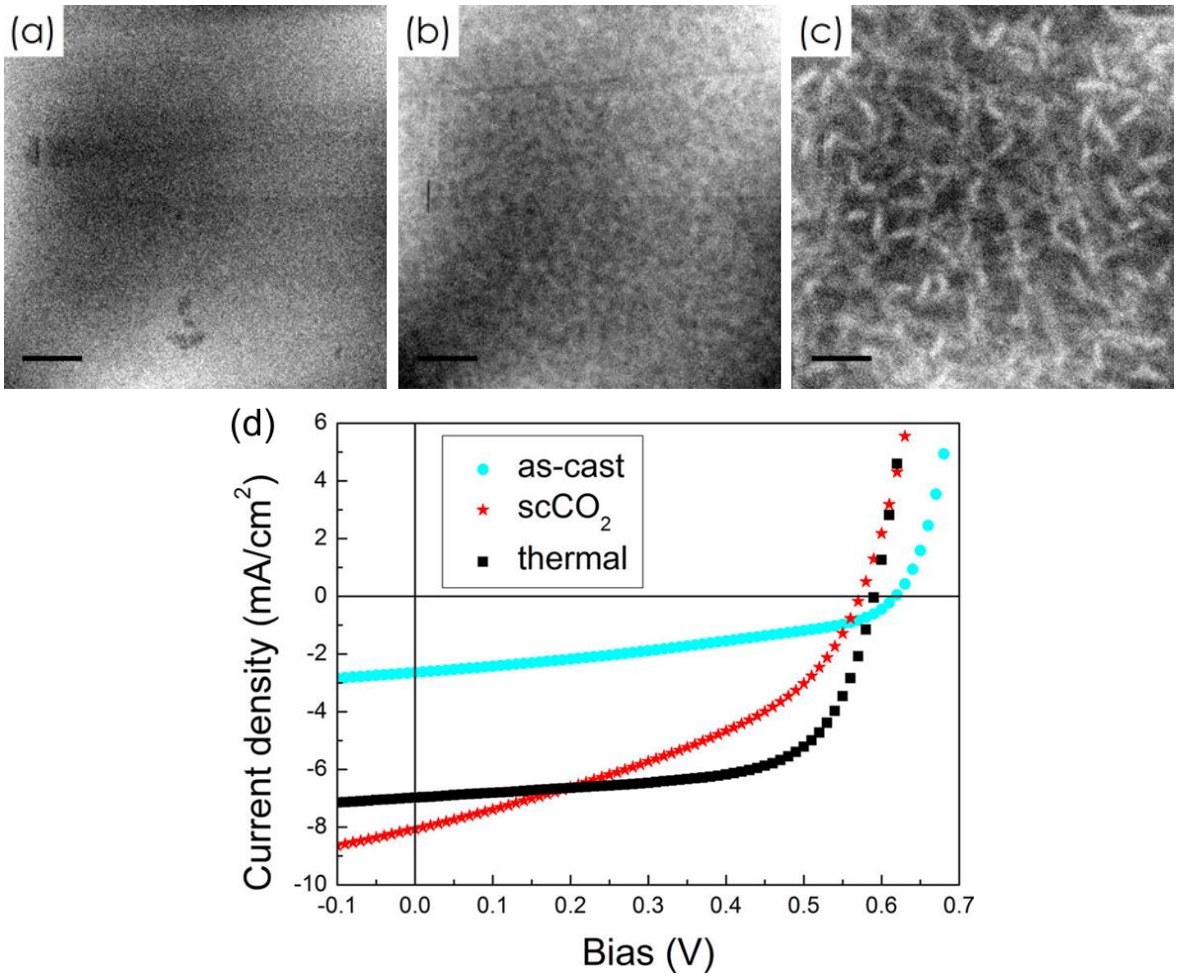

Figure 1.3 Energy-filtered TEM images (scale bar 50 nm) of P3HT:PCBM films: (a) as-cast, (b) processed with supercritical CO2 (scCO2) and (c) thermally annealed. Brighter regions are P3HT-rich and darker regions are PCBM-rich. J-V curves for P3HT:PCBM devices processed under different conditions. Adapted with permission from *J. Phys. Chem. C* **118,** 3968–3975. Copyright (2014) American Physical Society.

1.3. EFFECT OF DISORDER ON CHARGE TRANSPORT

As previously alluded, conjugated polymers form semicrystalline morphologies with a mixture of ordered and disordered regions. Intrachain charge transport along linear segments of chains remains the most rapid conduction mechanism, but to traverse macroscopic distances, it is necessary for charges to hop between chains as well. This occurs most easily within highly-ordered crystallites, although it has been suggested that just a few closely packed short segments is sufficient to enable efficient interchain hopping.[9,10] The understanding of charge transport in

relatively disordered polymeric systems has evolved significantly over the past decade, and the general picture that has emerged is that charge carriers favor the lowest energy routes, and thus remain largely confined ordered aggregates, traversing the amorphous regions only when necessary along interconnecting tie-chains. Under conventional casting/processing techniques, the amorphous chains, and even the ordered domains, are randomly-oriented with respect to one another; the path of least resistance thus involves a highly tortuous route, which further limits the carrier mobility.

As previously discussed, the electrical and other physical properties of conjugated polymers are highly anisotropic, with the most efficient transport occurring along a straight/planar backbone. For many applications, transport is only relevant in one direction, and thus it has been stipulated that directed alignment of polymer chains is one of the most promising strategies to improve their carrier transport capabilities. By exploiting anisotropic behavior to maximize carrier mobility in the direction of interest, it is possible to overcome traditionally inferior "isotropic" mobilities exhibited by polymers in their disordered/randomly-oriented state.[11–13] In doing so, it becomes possible to envision novel device architectures that are not restricted to conventional limitations on layer thicknesses or other dimensions.[14,15] In Chapter 3, the effect of chain alignment will be discussed, in context of long-range carrier collection in organic solar cells.

The term "disorder" can hold a variety of different meanings. For charge transport in disordered semiconductors, the Gaussian Disorder Model (GDM) has been widely applied.[16] Under the GDM, there are both positional and energetic contributions to disorder, which yield carrier transport characteristics with different dependencies on temperature and electric field; nonetheless, both kinds of disorder are inextricably linked to structural/morphological disorder.

Positional disorder is associated with the presence of both fast and slow pathways due to morphological heterogeneity and/or anisotropy. Carriers prefer to follow pathways with low barriers to transport, but strong external fields may force them to take more direct, energetically-unfavorable routes. Energetic disorder, on the other hand, relates to the broadened density of states (DoS) resulting from structural disorder; carriers trapped in tail states may require significant activation energies to mobilize. In this case, however, externally-applied fields lower the barriers against hopping in the forward direction. The different principles of positional and energetic disorder are illustrated in **Figure 1.4**.

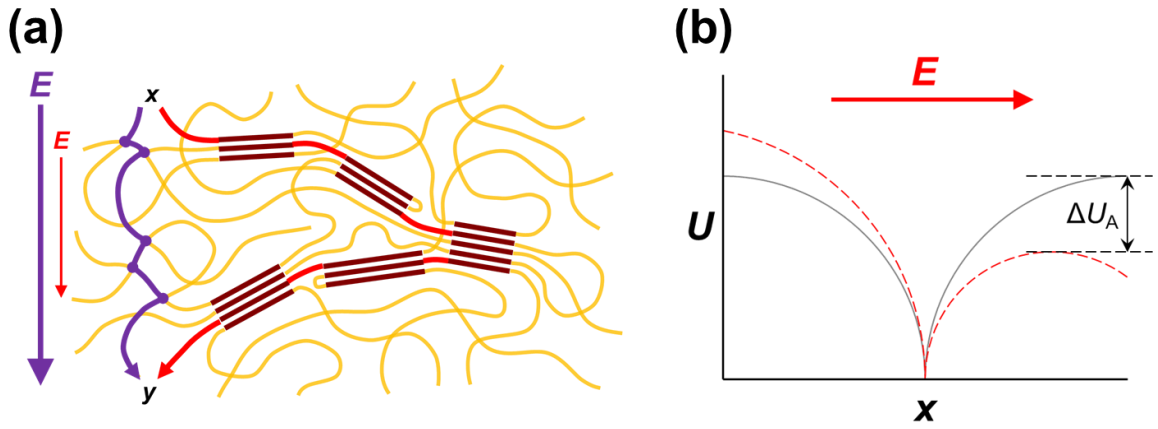

Figure 1.4 Illustrations of the effects of positional and energetic disorder on the field-dependency of mobility within the framework of the GDM. In a system with high positional disorder (a), at low fields carriers can take a longer but faster pathway from *x* to *y* (red), but at high fields they are forced along a more direct but slower pathway (purple). Energetic disorder creates activation energy barriers against hopping to adjacent sites (b), but application of an external field lowers the barrier in the forward hopping direction.

Chapter 4 will cover the topic of charge transport in disordered systems in greater detail, and examine the unequal effects of disorder on different modes of charge transport in conjugated polymer thin films. This is achieved experimentally through the use of different methods to fabricate the thin films – casting from solution versus depositing from vacuum – to create very distinctive model systems possessing very different degrees of disorder.

REFERENCES

1. A. Salleo, R. J. Kline, D. M. DeLongchamp, and M. L. Chabinyc: Microstructural Characterization and Charge Transport in Thin Films of Conjugated Polymers. *Adv. Mater.* **22,** 3812–3838 (2010).
2. C. W. Tang: Two-layer organic photovoltaic cell. *Appl. Phys. Lett.* **48,** 183–185 (1986).
3. J. Peet, A. J. Heeger, and G. C. Bazan: 'Plastic' Solar Cells: Self-Assembly of Bulk Heterojunction Nanomaterials by Spontaneous Phase Separation. *Acc. Chem. Res.* **42,** 1700–1708 (2009).
4. G. Dennler, M. C. Scharber, and C. J. Brabec: Polymer-Fullerene Bulk-Heterojunction Solar Cells. *Adv. Mater.* **21,** 1323–1338 (2009).
5. Y. Liang, Z. Xu, J. Xia, S.-T. Tsai, Y. Wu, G. Li, C. Ray, and L. Yu: For the Bright Future-Bulk Heterojunction Polymer Solar Cells with Power Conversion Efficiency of 7.4%. *Adv. Mater.* **22,** E135–E138 (2010).
6. B. P. Lyons, N. Clarke, and C. Groves: The relative importance of domain size, domain purity and domain interfaces to the performance of bulk-heterojunction organic photovoltaics. *Energy Environ. Sci.* **5,** 7657–7663 (2012).
7. B. Huang, J. A. Amonoo, A. Li, X. C. Chen, and P. F. Green: Role of Domain Size and Phase Purity on Charge Carrier Density, Mobility, and Recombination in Poly(3-hexylthiophene):Phenyl-C61-butyric Acid Methyl Ester Devices. *J. Phys. Chem. C* **118,** 3968–3975 (2014).
8. J. A. Amonoo, E. Glynos, X. C. Chen, and P. F. Green: An Alternative Processing Strategy for Organic Photovoltaic Devices Using a Supercritical Fluid. *J. Phys. Chem. C* **116,** 20708–20716 (2012).
9. R. Noriega, J. Rivnay, K. Vandewal, F. P. V. Koch, N. Stingelin, P. Smith, M. F. Toney, and A. Salleo: A general relationship between disorder, aggregation and charge transport in conjugated polymers. *Nat. Mater.* **12,** 1038–1044 (2013).
10. S. A. Mollinger, B. A. Krajina, R. Noriega, A. Salleo, and A. J. Spakowitz: Percolation, Tie-Molecules, and the Microstructural Determinants of Charge Transport in Semicrystalline Conjugated Polymers. *ACS Macro Lett.* 708–712 (2015). doi:10.1021/acsmacrolett.5b00314
11. H. Sirringhaus, R. J. Wilson, R. H. Friend, M. Inbasekaran, W. Wu, E. P. Woo, M. Grell, and D. D. C. Bradley: Mobility enhancement in conjugated polymer field-effect transistors through chain alignment in a liquid-crystalline phase. *Appl. Phys. Lett.* **77,** 406–408 (2000).
12. M. J. Lee, D. Gupta, N. Zhao, M. Heeney, I. McCulloch, and H. Sirringhaus: Anisotropy of Charge Transport in a Uniaxially Aligned and Chain-Extended, High-Mobility, Conjugated Polymer Semiconductor. *Adv. Funct. Mater.* **21,** 932–940 (2011).
13. B. T. O'Connor, O. G. Reid, X. Zhang, R. J. Kline, L. J. Richter, D. J. Gundlach, D. M. DeLongchamp, M. F. Toney, N. Kopidakis, and G. Rumbles: Morphological Origin of Charge Transport Anisotropy in Aligned Polythiophene Thin Films. *Adv. Funct. Mater.* **24,** 3422–3431 (2014).
14. X. Hu, C. Yi, M. Wang, C.-H. Hsu, S. Liu, K. Zhang, C. Zhong, F. Huang, X. Gong, and Y. Cao: High-Performance Inverted Organic Photovoltaics with Over 1-μm Thick Active Layers. *Adv. Energy Mater.* 1400378 (2014). doi:10.1002/aenm.201400378
15. M. Kim, J. H. Park, J. H. Kim, J. H. Sung, S. B. Jo, M.-H. Jo, and K. Cho: Lateral Organic Solar Cells with Self-Assembled Semiconductor Nanowires. *Adv. Energy Mater.* **5,** 1401317 (2015).

16. H. Bässler: Charge Transport in Disordered Organic Photoconductors a Monte Carlo Simulation Study. *Phys. Status Solidi B* **175,** 15–56 (1993).

CHAPTER II:
USING A COPOLYMER ADDITIVE TO TAILOR THE MORPHOLOGY OF POLYMER/FULLERENE SOLAR CELLS

Reprinted with permission from:

A. Li, J. Amonoo, B. Huang, P. K. Goldberg, A. J. McNeil, P. F. Green: Enhancing photovoltaic performance using an all-conjugated random copolymer to tailor bulk and interfacial morphology of the P3HT:ICBA active layer. *Adv. Func. Mater.* **24(35)**, 5594-5602 (2014).

2.1. INTRODUCTION

Polymer-based organic photovoltaics (OPVs) have garnered great interest due to their potential for low-cost and high-throughput roll-to-roll fabrication. Overall device performance is a product of carrier generation and transport processes which are heavily influenced by the morphology of the photoactive layer and its interfaces. On one hand are the donor/acceptor (D/A) interfaces associated with BHJ structure, which play host to both exciton dissociation and carrier recombination processes. Another type of interface exists between the organic active layer and the typically inorganic electrode, which plays a critical role in carrier collection. In designing "optimal" morphologies for maximum power conversion efficiency (PCE), it is important to consider both the bulk internal morphology as well as interfacial structure/composition.

The morphology of the active layer BHJ is often described as a heterogeneous blend of crystalline aggregates/domains and amorphous phases with varying degrees of intermixing.

Some miscibility between the components is necessary to maintain nano-scale domains and ensure that excitons can migrate to the D/A interfacial region and dissociate into free carriers.[1–3] Excessive intermixing, however, increases the sites and probability for non-geminate recombination and can suppress molecular ordering which facilitates carrier transport. Optimizing BHJ morphology to achieve a balance between carrier generation and transport is highly system-dependent and has been the subject of numerous experimental and computational studies.[4–6] To this end, a wide range of strategies have been developed,[7] including molecular design, choice of solvents and additives,[8–10] and various annealing/post-processing techniques.[11–14] More recently, there have been a number of studies that include blending oligomer/polymer additives with the active components as an alternate means to control the morphology. For example, small concentrations of copolymers have been added to poly(3-hexylthiophene (P3HT):phenyl-C_{61} butyric acid methyl ester (PCBM) blends as compatibilizers or nanostructuring agents. Because the chemical constituents of the copolymers have different affinities for P3HT and PCBM components, the copolymers tend to segregate to the domain boundaries in order to minimize the free energy of the system. Consequently, incorporating them into the polymer/fullerene blend could alter the BHJ morphology (domain size, interfacial structure, extent of phase separation, etc.).[15–19] This strategy has been deployed using rod-coil diblocks,[20–23] and more recently, extended to all-conjugated copolymers of a range of architectures (block, gradient, random).[24,25] Unfortunately, suppressing PCBM aggregate growth and increasing structural order have not always translated into improved device performance, which may be partly due to the inclusion of non-conductive coil blocks.

In addition to the internal BHJ morphology, the nature of the active layer/electrode interfaces plays a vital role in device performance.[26] While the maximum attainable open-circuit

voltage (V_{OC}) of a device is governed by the difference between the energies of the highest occupied molecular orbital (HOMO) of the donor and the lowest unoccupied molecular orbital (LUMO) of the acceptor, voltage losses can be incurred by a variety of mechanisms at the electrode interfaces, which include extraction barriers, band bending, defect/trap states, etc. Typically, these effects also reduce carrier collection efficiency, manifesting as reduced short-circuit current (J_{SC}) and fill factor (FF).[27–29] Thus, it has become widespread practice to insert another material between the active layer and electrodes; these interlayers can serve multiple purposes including work function alignment, selective carrier transport, and dipole formation / internal field enhancement.[30] Traditionally, these interlayers have predominantly consisted of vacuum-deposited inorganic materials, but in recent years there has been a trend towards solution-processible materials compatible for roll-to-roll printing.[31–33] For layer-by-layer deposition, however, the need for orthogonal solvents imposes significant limitations, depending on material solubilities.

Tailoring the BHJ morphology and modifying electrode interfaces have usually been addressed as different questions requiring separate strategies, but in this study we show that altering the active layer composition can involve both aspects simultaneously. Herein, we introduce a fully-conjugated random copolymer additive: poly(3-hexylthiophene-*r*-3-((hexyloxy)methyl)thiophene), P(3HT-*r*-3HOMT), which simultaneously modifies the BHJ morphology and the active layer/electrode interface. We systematically incorporated varying concentrations of the random copolymer (RCP) into a blend of P3HT and indene-C_{60} bisadduct (ICBA),[34–36] and found that device efficiencies improved substantially at optimized loading fractions. Both the internal and interfacial morphology of the active layer are characterized and correlated to the device performance. We conclude that the RCP plays an important role on two

fronts, altering the D/A phase separation within the BHJ as well as segregating to the cathode contact, both of which facilitate collection of photogenerated carriers.

2.2. EXPERIMENTAL

2.2.1. Polymer Synthesis

P3HOMT homopolymer and P(3HT-*r*-3HOMT) were synthesized by a nickel-catalyzed catalyst-transfer polycondensation using the monomers and catalyst described for P8 in ref. [37]. The relative reactivities of the two monomer species are very similar and close to 1, yielding a random distribution along the chain (39:61 3HT:3HOMT ratio). Polymer molecular weights were determined using gel-permeation chromatography (GPC) by comparison with polystyrene standards (Varian, EasiCal PS-2 MW 580-377,400) on a Waters 1515 HPLC instrument equipped with Waters Styragel® (7.8 x 300 mm) THF HR 0.5, THF HR 1, and THF HR 4 type columns in sequence and analyzed with Waters 2487 dual absorbance detector (254 nm). Samples were dissolved in THF (with mild heating) and passed through a 0.2 μm PTFE filter prior to analysis. For P3HOMT, it was found that M_n = 16.2 kDa, PDI = 2.19, and regioregularity = 97%; for P(3HT-*r*-3HOMT), M_n = 38.0 kDa, PDI = 1.99, regioregularity = 98%. ^{1}H NMR and GPC spectra can be found in the Supporting Information.

2.2.2. Device Fabrication

Regioregular P3HT (Rieke Metals, M_w = 50-70 kDa), and $IC_{60}BA$ (Sigma Aldrich, 99% purity) were used as received. ITO-coated aluminosilicate glass slides (Delta Technologies, Ltd.) were cleaned by ultrasonication in acetone and isopropanol for 20 min each, followed by a 10 minute UV-ozone plasma treatment. Poly(3,4-ethylenedioxythiophene) poly(styrenesulfonate (PEDOT:PSS) (H.C. Starck Clevios PH 500) was spin-coated in ambient atmosphere onto the

ITO surface at 4000 rpm for 45 s, then annealed for 20 minutes at 130˚C to produce an approximately 50 nm film. All subsequent fabrication steps were performed in an N_2-filled glovebox. For characterization of the neat polymers, films were spin-cast from chlorobenzene onto the ITO/PEDOT:PSS substrate and annealed for 10 minutes at 150˚C. UV-vis absorption was measured using a PerkinElmer Lambda 750 Spectrophotometer.

Photovoltaic devices were fabricated in the conventional architecture with indium tin oxide (ITO) coated with poly(3,4-ethylenedioxythiophene) poly(styrene-sulfonate) (PEDOT:PSS) as the anode. The active layer consisted of P3HT:ICBA (1:1) as the baseline composition, to which 0 to 20 wt. % of P(3HT-*r*-3HOMT) was added, using 1,2-dichlorobenzene (*o*-DCB) as the common solvent for all blend solutions. These films were spin-coated at 800 rpm for 30 s, and then treated with solvent (c.a. 30 min) and thermal (150˚C for 10 min) annealing to produce active layer thickness of c.a. 180 nm as measured by spectroscopic ellipsometry (M 2000, J.A. Woollam Co.). The cathode consisted of 1 nm LiF and 70 Al deposited by vacuum thermal evaporation (Angstrom Engineering); a shadow mask was used to create 1 mm diameter electrodes. Devices were tested in ambient atmosphere under 1 sun illumination (100 mW cm^{-2}, AM 1.5) using an Oriel solar simulator, and the J-V characteristics were measured using a Agilent 4156C Semiconductor Parameter Analyzer. For photo-CELIV measurements, devices (fabricated in the same manner as described above) were loaded in a cryostat (Janis VPF-100, vacuum pressure 1 mTorr) and exposed to laser pulses (Quantel BrilliantEazy, λ = 532 nm, pulse intensity ca. 20 μJ cm^{-2}). A function generator (BK Precision 4075) applied a linearly increasing voltage to extract the photo-generated current transient, which was passed through a preamplifier (FEMTO DLPCA-200) and recorded by a digital oscilloscope (Tektronix TDS3052C).

2.2.3. Structural Characterization

AFM and KPFM were performed using the Asylum Research MFP-3D. For c-AFM, topography, phase, and dark current were mapped simultaneously in contact mode using a PtIr5-coated probe (NanoWorld) in ambient air, under an applied bias of +3.0 V. KPFM was performed using a platinum silicide-coated probe (Nanosensors) in an argon-filled cell. The probes were calibrated on highly ordered pyrolitic graphite with a work function of 4.6 eV. Surface potentials were measured at a lift height of 10 nm above the sample surface, outside the range of Van der Waals forces.[38,39] To measure the HOMO energies, samples were prepared on the conventional ITO/PEDOT:PSS substrate (high work function); to measure the LUMO energies, samples were prepared on ITO coated with ~10 nm of ethoxylated polyethyleneimine (PEIE), a low work function substrate.[40]

EFTEM was performed using a JEOL 2100F TEM, using an accelerating voltage of 200 kV and a slit width of 8 eV. Thinner films (c.a. 80 nm) were used for TEM sample preparation to reduce thickness convolution of vertically-overlapping domains/phases. Following the same casting and annealing procedures described previously, the films were sectioned using a razor blade and floated from the substrate by immersion in DI water; the sectioned films were collected onto copper grids with supporting mesh (Ted Pella, Inc.). In performing the EELS measurements, the beam covered a sufficiently large area such that this "overall" EELS represented an averaged spectrum approximating that of a homogeneous mixture. Selected-area local EELS were extracted from spots sampled from multiple different P3HT- and ICBA-rich regions (determined from the EFTEM images) to get a statistically significant values for the plasmon peak energies. These values could be compared to that of the overall EELS to semi-quantitatively compare the relative phase purities of the P3HT- and ICBA-rich domains.

XPS and D-SIMS measurements were performed by Dr. Thomas Mates (Microscopy and Microanalysis Facility at UCSB). XPS was performed with the Kratos Axis Ultra X-ray Photoelectron Spectroscopy System. D-SIMS was performed with the Physical Electronics 6650 Dynamic Secondary Ion Mass Spectrometer using the oxygen ion gun.

2.3. RESULTS AND DISCUSSION

2.3.1. Properties and Behaviors of Neat Polymer Films

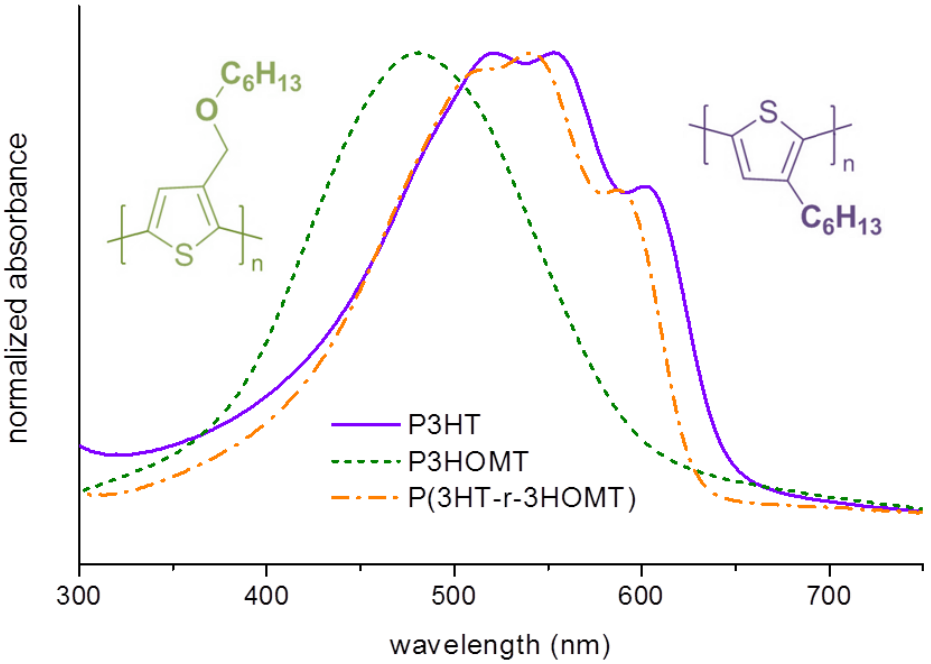

Figure 2.1 UV-vis absorption spectra of P3HT, P3HOMT, and P(3HT-*r*-3HOMT). Chemical structures of the two homopolymers are also shown.

Annealed films of P3HT, P3HOMT, and P(3HT-*r*-3HOMT) were characterized by UV-visible spectroscopy and conductive atomic force microscopy (c-AFM). The absorption profile of P3HOMT was found to be significantly blue-shifted from that of P3HT and the peaks associated with π-aggregation are absent (**Figure 2.1**). The apparent lack of extended π-conjugation in P3HOMT films suggests that the modified side chain disrupts alignment and

packing of polymer chains, thus inhibiting crystallization and long-range ordering.[41] The absorption profile of the random copolymer (RCP), on the other hand, closely resembles that of P3HT but is slightly blue-shifted. This result indicates that the suppressed ordering of P3HOMT chains is mitigated when 3HT units are dispersed along the polymer chain.

As shown in **Figure 2.2**, AFM topographical scans of pure polymer films reveal that P3HOMT has a much smoother surface than P3HT (rms roughness of 0.8 nm versus 5.4 nm) and a comparatively featureless texture based on the friction map in Figure 2.2b. In contrast, the P(3HT-*r*-3HOMT) film exhibits a distinctive surface texture with fine lamellae-like features (Figure 2.2c), along with an intermediate surface roughness of 4.3 nm. These findings corroborate the UV-vis data, showing that P3HOMT remains largely amorphous even after annealing, whereas the RCP is capable of packing and reorganizing to produce a more semicrystalline film, although with a different surface structure from homopolymer P3HT film. The surface features can be seen even more clearly in the dark current maps (Figure 2.2d-f), and by plotting dark current measured at each pixel (under +3.0 V applied bias) in a histogram (Figure 2.2g), it is possible to gain a semi-quantitative sense of the relative carrier mobilities of each polymer. The P3HOMT is found to possess very low conductivity compared to P3HT, reflecting poor carrier transport through the disordered polymer chains of the amorphous film. The intermediate and broad distribution of current for P(3HT-*r*-3HOMT) confirms the ability of its chains to align and pack into some ordered structures that facilitate carrier transport, although to a lesser extent than homopolymer P3HT.

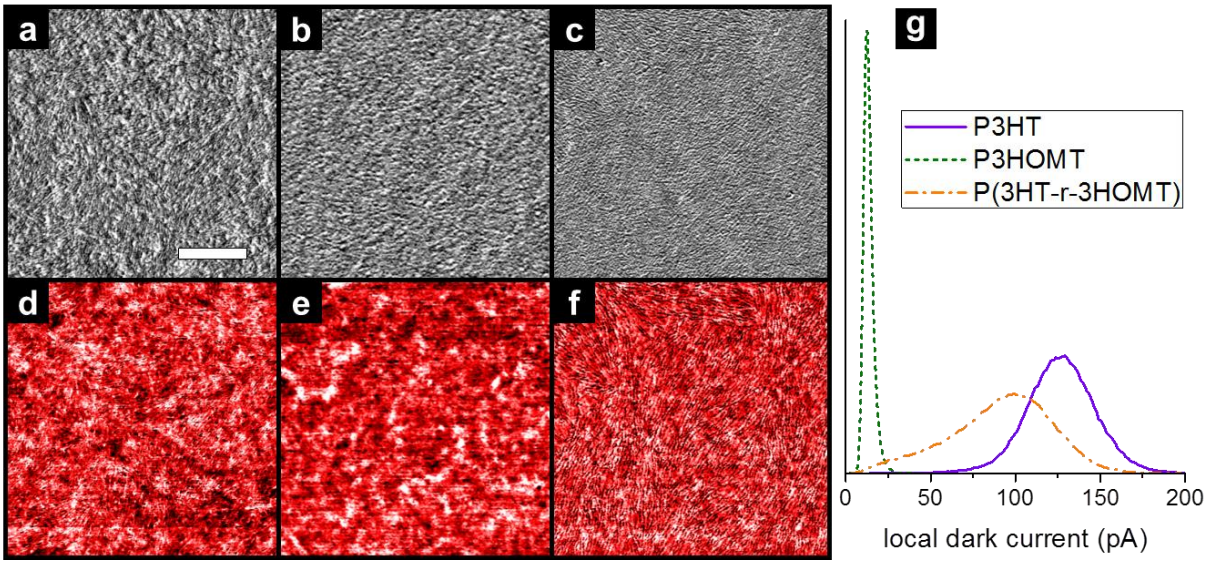

Figure 2.2 Phase (a-c) and dark current (d-f) micrographs for films of pure P3HT (a,d), P3HOMT (b,e) and RCP (c,f) (scale bar = 0.5 µm). The dark current values measured at each pixel of the c-AFM images are plotted in the histogram (g).

Even in the absence of enthalpic driving forces, entropic effects associated with differences between polymer chain flexibilities and crystallization behavior can lead to the preferential segregation of one component to the free surface.[42–44] We evaluated the relative surface segregation affinities of P3HT, P3HOMT and P(3HT-*r*-3HOMT) by comparing the surface morphologies of blends to those of the pure components. As shown in **Figure 2.3**, the surface of the P3HT:P3HOMT blend (Figure 2.3a,c) closely resembles the surface of pristine P3HOMT. Likewise, the surface of the P3HT:RCP blend (Figure 2.3b,d) exhibits a texture nearly identical to that of the pristine RCP film. These findings strongly suggest that P3HOMT and P(3HT-*r*-3HOMT) exhibit a stronger tendency for surface segregation than P3HT, which is consistent with their relatively lower degrees of crystallinity indicated by their optoelectronic properties.

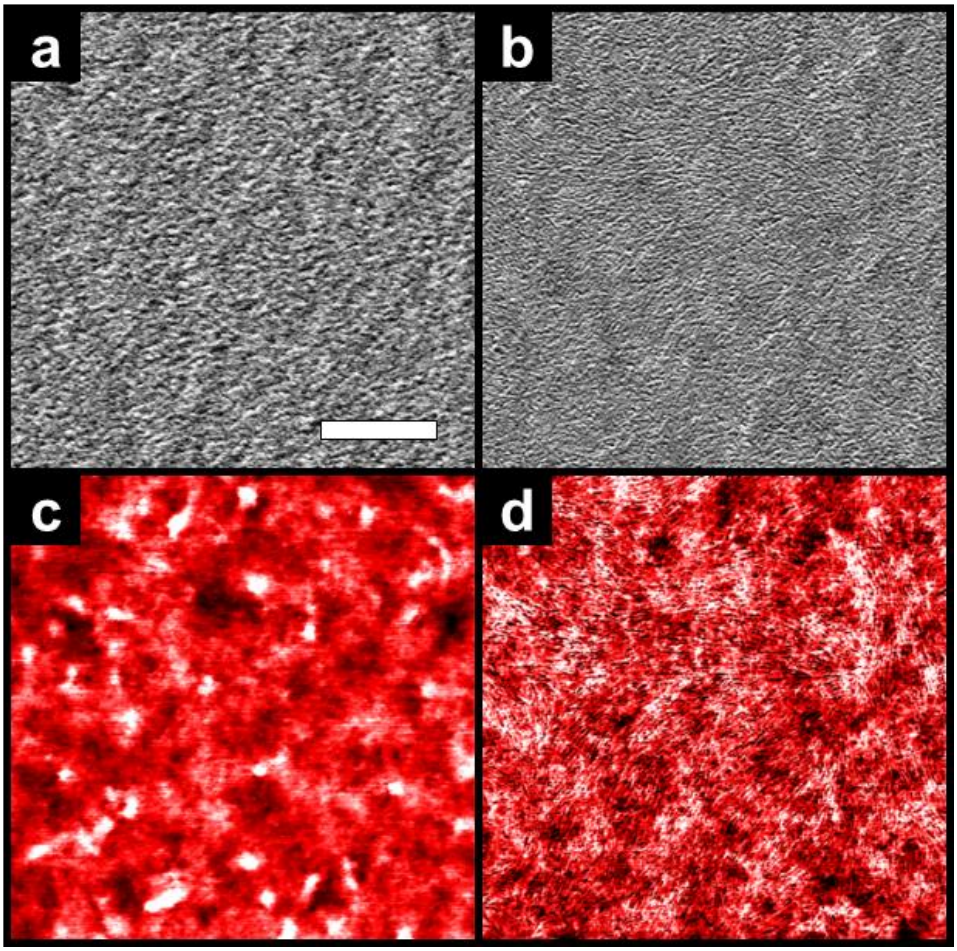

Figure 2.3 Phase (a,b) and dark current (c,d) micrographs for a P3HT:P3HOMT (1:1) blend (a,c) and a P3HT:RCP (3:1) blend (b,d) (scale bar = 0.5 μm).

2.3.2. Bulk Heterojunction Device Measurements

Having established some context for the characteristics and behavior of the RCP, we will now discuss its effect as an additive for P3HT:ICBA bulk heterojunction solar cells. For each RCP loading concentration from 0% to 20%, at least 8 devices were measured; representative J-V curves under illumination are shown in **Figure 2.4**, and the average values for the V_{OC}, J_{SC}, FF, and PCE are summarized in **Table 2.1**. The "champion" device performance was achieved at a RCP loading concentration of 8 wt.%, producing a 20% increase in PCE (from 4.2% to 5.0%) over the reference device (0% RCP). This improvement is due in large part to a higher V_{OC},

which increases monotonically with RCP concentration. J_{SC} and FF show some improvement up to the optimal composition, but they decrease significantly at higher loadings. This deterioration is unsurprising considering the inferior carrier transport properties of P(3HT-*r*-3HOMT); while insignificant at low concentrations, the lower conductivity of the RCP is expected to increase the series resistance of the device more noticeably at higher loadings, hampering carrier transport through the active layer and decreasing photocurrent collection. Furthermore, as more RCP is added to the blend, the corresponding decrease in the total fraction of ICBA may reduce the connectivity of electron-transporting fullerene clusters/domains, leading to a decrease in photocurrent collection.[3]

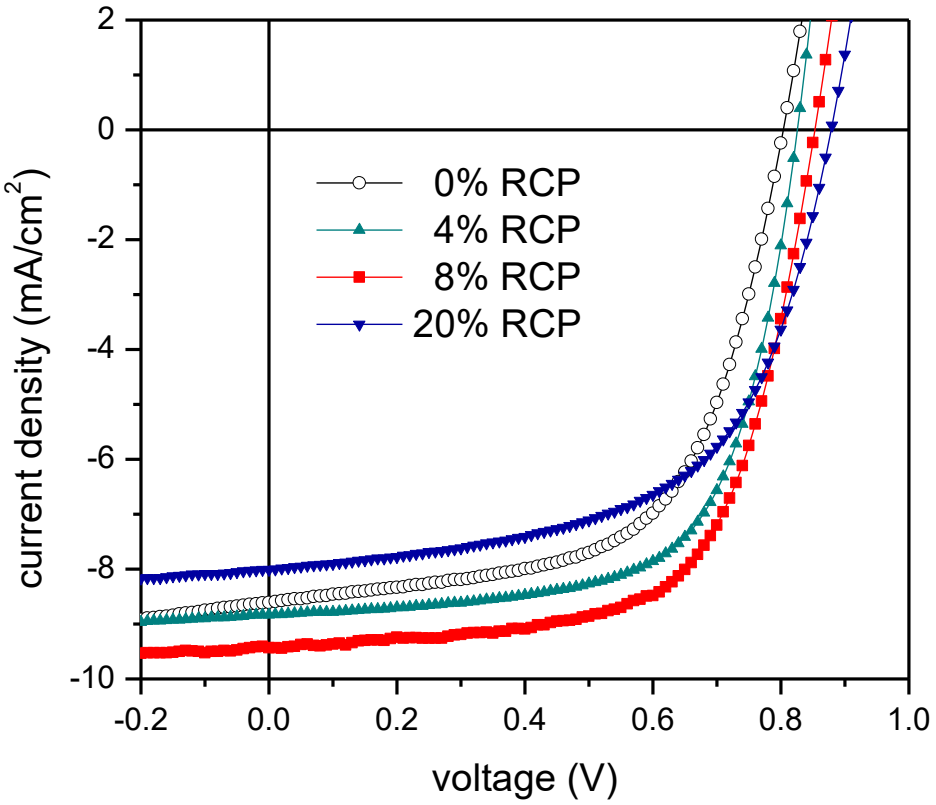

Figure 2.4 Representative J-V curves under illumination for devices fabricated from a range of RCP loadings (wt.%). The curves for 0% RCP (◦) and 8% RCP (▪) represent the performances of the reference and champion devices, respectively.

Table 2.1 Summary of device characteristics for different copolymer concentrations.

f_{RCP} (wt. %)	V_{OC} (V)	J_{SC} (mA cm^{-1})	FF	PCE (%)
0	0.79 (±0.02)	8.7 (±0.4)	0.61 (±0.01)	4.2 (±0.2)
2	0.81 (±0.01)	8.4 (±0.3)	0.65 (±0.01)	4.4 (±0.2)
4	0.82 (±0.02)	8.3 (±0.2)	0.67 (±0.01)	4.5 (±0.1)
6	0.83 (±0.02)	8.8 (±0.4)	0.66 (±0.01)	4.8 (±0.2)
8	0.84 (±0.01)	9.1 (±0.2)	0.65 (±0.01)	5.0 (±0.1)
10	0.85 (±0.02)	9.1 (±0.3)	0.62 (±0.01)	4.7 (±0.1)
15	0.86 (±0.01)	8.6 (±0.2)	0.62 (±0.01)	4.6 (±0.1)
20	0.88 (±0.01)	8.0 (±0.2)	0.59 (±0.02)	4.2 (±0.1)

Carrier generation/recombination for reference (0% RCP) and champion (8% RCP) devices were characterized using photo-CELIV. Following laser pulse excitation, the transient current was measured at various delay times t to obtain photo-generated carrier density $n(t)$, shown in **Figure 2.5**. The recombination coefficient β was calculated by fitting the measured carrier densities to a bimolecular decay law for nondispersive recombination: $n(t) = n(0)[1 + (t/\tau_B)]^{-1}$, where $\tau_B = [n(0)\beta]^{-1}$.[45] From this analysis, the reference device was found to have $n(0)$ = (1.70 ± 0.3) x 10^{-16} cm^{-3} and β = (10.2 ± 0.1) x 10^{-13} cm^3 s^{-1}, while the champion device exhibited $n(0)$ = (1.11 ± 0.1) x 10^{-16} cm^{-3} and β = (8.4 ± 0.1) x 10^{-13} cm^3 s^{-1}, indicating a reduction in both initial carrier generation and non-geminate recombination. It is important to note that while the bimolecular model provides a fairly good fit for the champion device, it significantly underestimates the rate of carrier decay in the reference device at longer delay times (> 100 μs). This discrepancy suggests that the lower performance of the reference P3HT:ICBA devices may originate from additional recombination losses not described by bimolecular mechanism, such as trap-assisted or surface recombination. These findings will be revisited in the context of the active layer morphology, following the discussion of structural characterization.

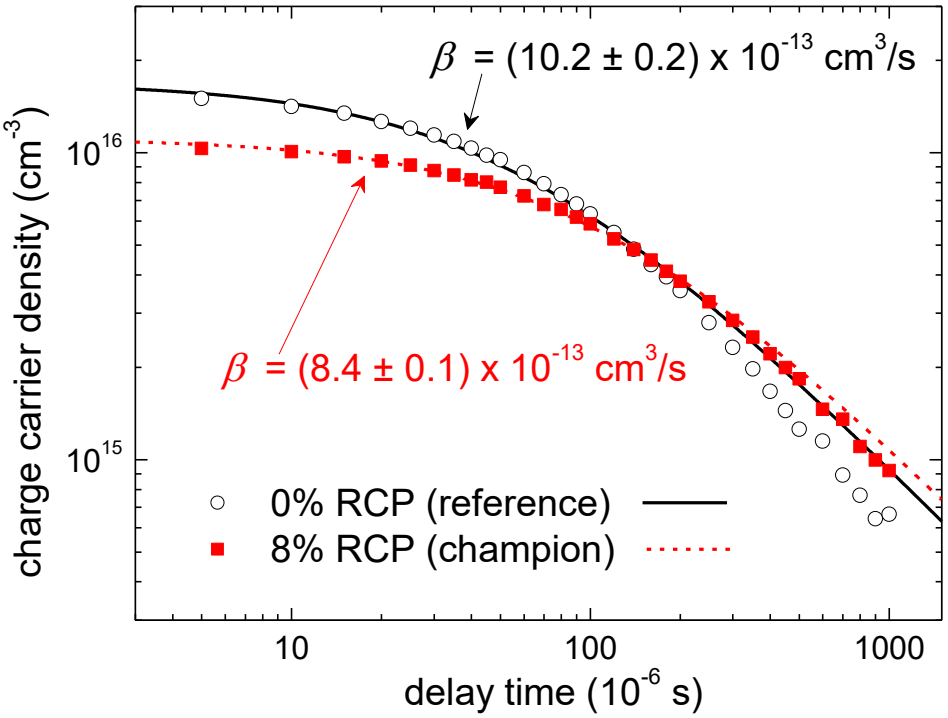

Figure 2.5 Carrier densities $n(t)$ measured by photo-CELIV for the reference (◦) and champion (▪) devices following a delay of t after laser pulse excitation. The curves are the fits to a bimolecular decay law with recombination coefficient β.

2.3.3. Bulk Heterojunction Morphological Characterization

The bulk internal morphologies of device active layers were studied using energy-filtered transmission electron microscopy (EFTEM), taking advantage of the different electron energy-loss spectra (EELS) of P3HT and ICBA to distinguish polymer and fullerene-rich domains/phases.[46,47] Unfortunately, the minority fraction of the RCP could not be identified in the EFTEM images, due to its similar chemical structure to P3HT and nearly identical EELS. However, a qualitative comparison of the images in **Figure 2.6** reveals that the active layer of the champion device (Figure 2.6b) displays more distinct and numerous P3HT fibrils (the dark features) and clearer contrast between the P3HT and ICBA-rich phases compared to the reference sample (Figure 2.6a). The relative difference in phase purities was semi-quantitatively evaluated by analyzing the local EELS of P3HT and ICBA-rich regions, as described in the

Experimental Section. Based on the plasmon peak energies, the incorporation of RCP appears to have slightly improved the relative purity of the P3HT domains (although the difference is small compared to the range of error) but significantly increased the relative purity of the ICBA-rich phase; the higher purity is consistent with the visually clearer contrast in the EFTEM image. This result suggests that in the reference sample, the fibrils are sparse, but they are already relatively pure in P3HT. With addition of the RCP to the champion sample, more of the P3HT "precipitated" out of the intermixed regions (thereby purifying the ICBA-rich phase) and aggregated into the more numerous fibrils.

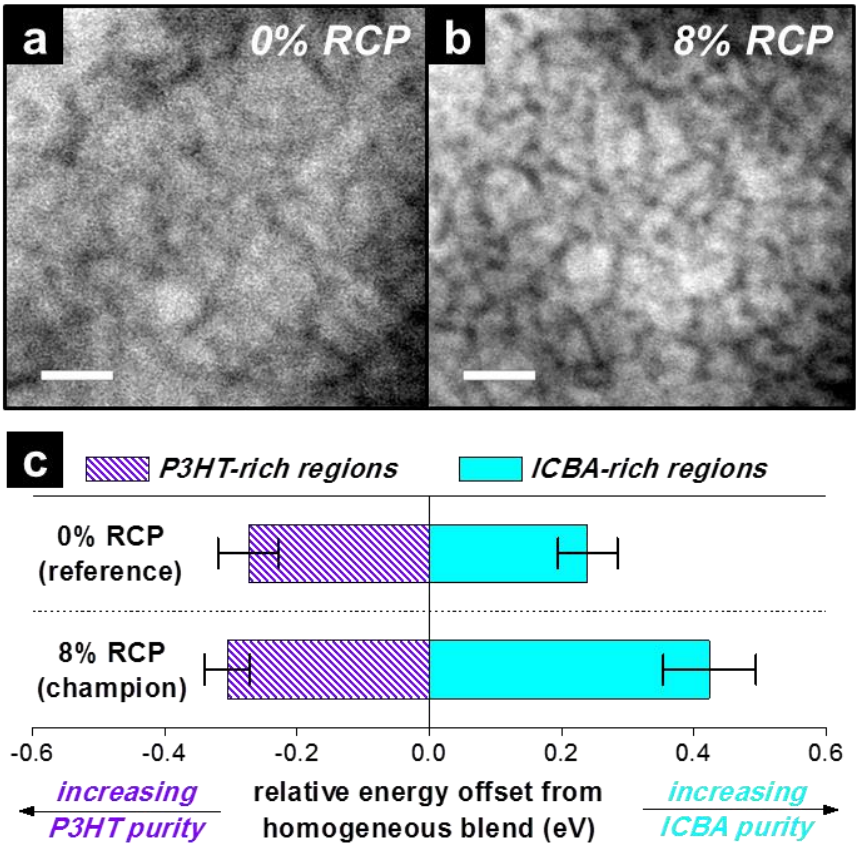

Figure 2.6 EFTEM images of the 0% RCP (a) and 8% RCP (b) active layers, taken at an energy-loss interval 31 ± 3 eV, such that the dark features correspond to P3HT-rich domains/fibrils and the bright regions correspond to the ICBA-rich phase (scale bar = 50 nm). The plot in (c) shows the difference in the plasmon peak energies between the overall EELS of the entire imaged area and the local EELS of P3HT- and ICBA-rich regions, respectively. A larger deviation from the overall EELS (corresponding to an averaged, homogenous blend) reflects higher phase purity.

Although the RCP cannot be spatially located in the EFTEM images, we can use polymer physics and thermodynamics to rationalize its influence on the phase behavior of the blend. It is well-established that, in order to minimize free energy, copolymers in amorphous polymer blends tend to either segregate to interfaces (between phases and/or at the surfaces) or form micelles, due to differences in relative interactions between each copolymer constituent and the components of the host blend.[48,49] In a mixture of two immiscible polymers, the presence of the copolymer (with appropriately-selected constituents) at the phase boundaries lowers the interfacial tension between the two phases, which inhibits macro-scale phase separation and stabilizes the morphology; for this reason, copolymers have often employed in low concentrations as surfactants or compatibilizers for immiscible blends.[50,51] It is worth noting that the systems investigated in this study differ in some respects from aforementioned immiscible polymer/polymer blends, due to the inherently high degree of intermixing between the P3HT and ICBA,[36] along with the rigidity of conjugated polymer chains and the behavior of fullerene molecules. Nonetheless, we can reasonably infer that the RCP segregates to the interfacial regions between P3HT and ICBA-rich phases (there is little driving force for micelle formation, since the RCP possesses a random distribution of 3HT and 3HOMT units). At these interfaces, the 3HT components of the copolymer preferentially interact with the P3HT homopolymer, and as a result, the covalently-bound 3HOMT components are also restricted to the boundaries of P3HT domains. Although the precise mechanism is unclear, the "encapsulation" of P3HT domains by the RCP could exclude ICBA molecules from infiltrating the polymer phase, giving rise to the observed enhancement in polymer/fullerene phase separation (purity). A similar effect was reported in recent computational work by Kipp and Ganesan, in which the addition of block

copolymers to polymer/fullerene blends produced an increase in short-range phase separation in the equilibrium morphologies.[52]

As previously alluded, in addition to the boundaries between phases/domains, interfacial segregation can also occur at the substrate and/or free surface of the film; in a device configuration, these correspond to the bottom and deposited electrodes, respectively. As previously shown, the RCP exhibits lower surface energy compared to P3HT, so we focused our attention on the free surface of the active layer, which contacts the deposited LiF/Al cathode in completed devices. In **Figure 2.7**, the AFM friction maps (Figure 2.7a insets) reveal that the reference sample possesses a rougher and coarser surface compared to the 8% RCP sample, which exhibits a fine lamellar texture strikingly similar to that of the pure RCP film (Figure 2.2c,f). To complement these AFM measurements, XPS was performed to detect changes the composition of the active layer surface upon incorporation of the RCP. Both samples exhibited nearly identical, strong sulfur 2p peaks, consistent with studies which have shown the preferential surface segregation of P3HT in a polymer/fullerene blend.[53] Although the chemical compositions of the two samples were nearly identical, the RCP uniquely possesses oxygen atoms (in the 3HOMT side chains). The oxygen 2s peak was too weak/noisy to extract useful information; instead we analyzed the carbon 1s peak around 285 eV, applying a number of fittings to separate the signal into peaks corresponding to specific types of bonds (Figure 2.7a). We find a significant increase in C-O bond density at the surface of the 8% RCP sample (the C-O peak in the reference sample likely originates from surface contaminants and oxidized species). The combination of AFM and XPS measurements provide strong evidence that the RCP preferentially segregates to the free surface, resulting in a RCP-rich interfacial layer in contact with the deposited cathode (Figure 2.7b).

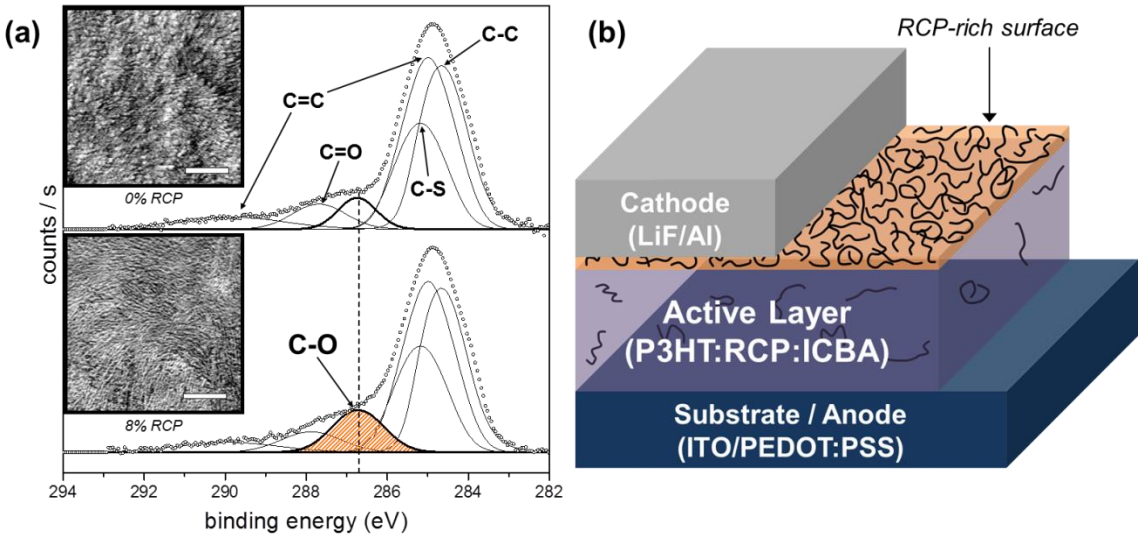

Figure 2.7 (a) Carbon 1s peak from XPS for the reference (0% RCP) and champion (8% RCP) devices, with corresponding AFM phase images shown in the insets (scale bar = 0.5 μm). The bolded curve with orange shading is the fitted peak corresponding to C-O ether bonds. (b) Diagram of the proposed surface segregation behavior of the RCP (represented by black lines) in the active layer of the device.

2.2.4. Connecting Device Performance with Morphology

Numerous studies have shown that differences in BHJ morphology have important consequences on photo-carrier generation and transport, which manifest as changes in the V_{OC}, J_{SC}, FF, and PCE of devices.[54,55] Simulations by Lyons et al. show that higher phase purity and sharper D/A interfaces reduces the available interfacial area for exciton dissociation, and thus the rate of carrier generation. Despite this, provided that the domains sizes are within the exciton diffusion length (~10 nm), this decrease is more than compensated by a much higher carrier collection efficiency due to reduced bimolecular recombination.[56] These computational results are consistent with our EFTEM images and carrier recombination measurements – clearer contrast between P3HT and ICBA domains and a greater degree of structural order are correlated with a lower initial carrier density but slower recombination rate in the champion device. Furthermore, while the reference P3HT:ICBA device appears to suffer from recombination losses beyond the bimolecular mechanism, the champion device does not. One way to rationalize

this observation is that in the reference device, not only does the higher degree of intermixing increase bimolecular recombination via the larger donor/acceptor interface, it also results in greater structural disorder which produces more gap states for trap-assisted recombination. The enhanced phase separation and improved structural order after incorporating the RCP led to a corresponding decrease in energetic disorder and trap density, thereby mitigating those losses. However, as previously discussed, the RCP is less conductive than P3HT homopolymer, so at high concentrations, excess copolymer impedes carrier transport and undermines the benefits conferred by the improved morphology. These competing phenomena contribute to the existence of an optimal RCP loading fraction.

While tailoring BHJ morphology can yield significant reductions in "bulk" recombination occurring within the active layer, changes to the film's interfacial structure and composition also play a critical role in carrier collection at the electrodes. For the P3HT:ICBA devices in this study, fabricated in the conventional architecture, it is therefore highly probable that the RCP-rich surface layer had a strong influence on carrier transport from the active layer to the cathode. Indeed, in a complementary study, Ma et al. used the interfacial (substrate) segregation of an amine-functionalized fullerene to create a self-assembled cathode interlayer for inverted devices.[57] In context of the carrier recombination findings from photo-CELIV, we propose that the enhanced device performance of the RCP-containing champion device is at least partly due to suppression of surface recombination at the cathode. Recall that the accelerated carrier decay in the reference device, which deviates from the bimolecular model prediction, occurred at longer delay times (onset ~100 μs); this time-lag could be associated with the time for photogenerated carriers to migrate to the cathode.

There are several mechanisms by which the surface-segregated RCP could aid in carrier extraction to reduce recombination at the interface. Its more amorphous character and the smoother film surface it forms could enable better physical contact with the cathode; another explanation could be that the oxygen-bearing side chains (weakly polar) of the RCP generate favorable interfacial dipoles. Although we do not exclude the possibility of these and other effects, in this study we focus on the influence of the copolymer on energy levels at the interface, employing Kelvin probe force microscopy (KPFM) to measure the surface potentials of active layers with and without RCP. Following the procedure described in the Experimental Section, the effective HOMO and LUMO energies of the blends were mapped, and the distributions of surface potential values plotted as a histogram in **Figure 2.8**, using a Gaussian fit to obtain representative HOMO/LUMO values for comparison (the corresponding KPFM images can be found in the Supporting Information). It is worth emphasizing that this technique is highly sensitive to the energies of the species at the surface, but the measured potentials are influenced by the underlying film. Thus, the surface potentials of the blends cannot be directly correlated to the HOMO/LUMO of individual species, but are averaged to some extent over all the constituents of the blend; for this reason, the surface potentials measured for the blends are higher than the pure polymers, being shifted to higher energies by the HOMO of ICBA.

From this analysis, we found that the HOMO of the champion RCP-containing sample shows a significant downward shift of ~0.1 eV from the reference P3HT:ICBA sample. This offset closely mirrors the difference between the measured HOMO energies for films of pure P3HT and RCP (Figure 2.8 inset), which strongly suggests that the lower HOMO of the champion blend is due to the surface-segregated RCP. On the other hand, the LUMO energies of the two samples mostly overlapped, and while the RCP-containing sample showed a broader

distribution of surface potentials, the peak values were almost identical. The broadening of surface LUMO energies could be ascribed to the more amorphous/disordered behavior of RCP chains, or to different electronic interactions between the molecular orbitals of RCP and ICBA, although the rigorous explanation is still unclear.

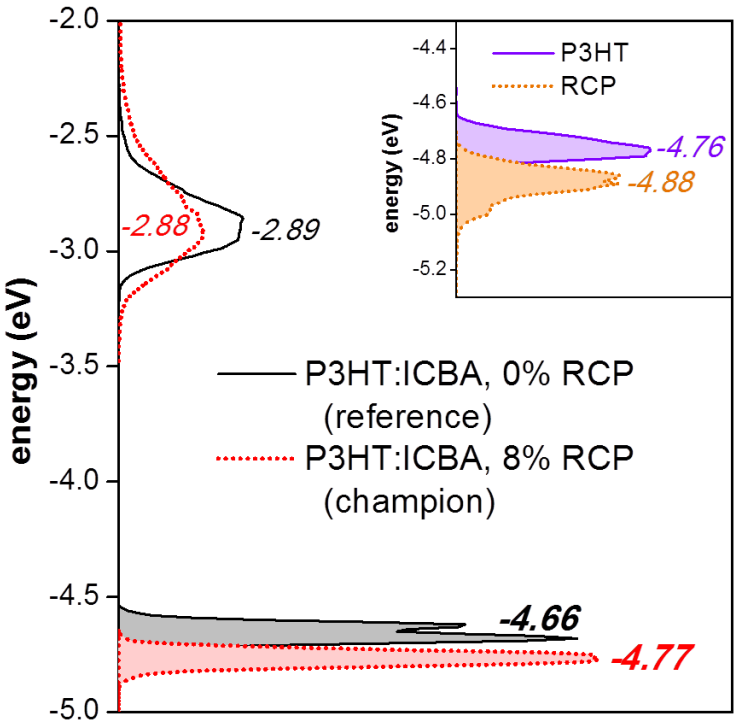

Figure 2.8 Surface potentials of the P3HT:ICBA active layer with and without RCP; the values measured at each pixel of the KPFM images are plotted as a histogram. The shaded distributions (lower) correspond to HOMO measurements and the unshaded distributions (upper) correspond to LUMO measurements. The values shown represent the energies of the peaks (from a Gaussian fit) of the respective HOMO/LUMO distributions. The inset histogram shows the HOMO surface potentials for pristine P3HT and RCP films.

Nonetheless, based on the offset in HOMO levels, we propose that the surface-segregated RCP helps to suppress surface recombination by curbing migration of positive charge carriers to the cathode. Holes transported along the conjugated polymer domains/chains encounter the deeper HOMO of the RCP if they approach the interface. Under this scenario, this downward band bending decreases the probability of holes reaching the cathode and undergoing surface

recombination with dissociated electrons. Although the RCP (and conjugated polymers in general) is primarily a hole-transporting material, electron extraction has been shown to be relatively unhindered provided that the polymer-rich interfacial layer is thin.[58] A sufficient amount of copolymer is required to populate the internal and external interfaces, so the optimal loading of 8% RCP could be associated with the threshold concentration at which the polymer/fullerene interfaces become saturated and the cathode contact is fully wetted. As even more RCP is added to the blend, besides potentially increasing the bulk series resistance of the device, further surface segregation may produce an excessively thick interfacial layer that acts as a barrier to electron extraction.

2.4. CONCLUSIONS

Having synthesized and characterized a fully-conjugated random copolymer, P(3HT-*r*-3HOMT), we incorporated it as an interfacially-active additive for P3HT:ICBA bulk heterojunction solar cells, achieving a 20% increase in PCE at the optimal loading concentration of 8 wt.%. The influence of the copolymer on the active layer morphology was studied in detail, employing a wide range of techniques to investigate the film's internal morphology as well as interfacial structure and composition. The enhanced device performance is credited to a combination of two main structural factors: 1) a superior microphase-separated BHJ morphology that reduced internal bimolecular recombination losses and 2) a copolymer-rich active layer/cathode interface that suppressed surface recombination and improved charge collection efficiency. These findings present new insights and opportunities for to take advantage of the self-organizing behavior of copolymers to tune the morphology and properties of polymeric thin films for OPVs and other applications.

REFERENCES

1. N. D. Treat, M. A. Brady, G. Smith, M. F. Toney, E. J. Kramer, C. J. Hawker, and M. L. Chabinyc: Interdiffusion of PCBM and P3HT Reveals Miscibility in a Photovoltaically Active Blend. *Adv. Energy Mater.* **1,** 82–89 (2011).
2. N. D. Treat, A. Varotto, C. J. Takacs, N. Batara, M. Al-Hashimi, M. J. Heeney, A. J. Heeger, F. Wudl, C. J. Hawker, and M. L. Chabinyc: Polymer-Fullerene Miscibility: A Metric for Screening New Materials for High-Performance Organic Solar Cells. *J. Am. Chem. Soc.* **134,** 15869–15879 (2012).
3. J. A. Bartelt, Z. M. Beiley, E. T. Hoke, W. R. Mateker, J. D. Douglas, B. A. Collins, J. R. Tumbleston, K. R. Graham, A. Amassian, H. Ade, J. M. J. Fréchet, M. F. Toney, and M. D. McGehee: The Importance of Fullerene Percolation in the Mixed Regions of Polymer–Fullerene Bulk Heterojunction Solar Cells. *Adv. Energy Mater.* **3,** 364–374 (2013).
4. D. Chen, A. Nakahara, D. Wei, D. Nordlund, and T. P. Russell: P3HT/PCBM Bulk Heterojunction Organic Photovoltaics: Correlating Efficiency and Morphology. *Nano Lett.* **11,** 561–567 (2011).
5. W. Ma, J. R. Tumbleston, M. Wang, E. Gann, F. Huang, and H. Ade: Domain Purity, Miscibility, and Molecular Orientation at Donor/Acceptor Interfaces in High Performance Organic Solar Cells: Paths to Further Improvement. *Adv. Energy Mater.* n/a–n/a (2013). doi:10.1002/aenm.201200912
6. C. Groves: Developing understanding of organic photovoltaic devices: kinetic Monte Carlo models of geminate and non-geminate recombination, charge transport and charge extraction. *Energy Environ. Sci.* (2013). doi:10.1039/C3EE41621F
7. J. Peet, A. J. Heeger, and G. C. Bazan: 'Plastic' Solar Cells: Self-Assembly of Bulk Heterojunction Nanomaterials by Spontaneous Phase Separation. *Acc. Chem. Res.* **42,** 1700–1708 (2009).
8. J. Peet, J. Y. Kim, N. E. Coates, W. L. Ma, D. Moses, A. J. Heeger, and G. C. Bazan: Efficiency enhancement in low-bandgap polymer solar cells by processing with alkane dithiols. *Nat. Mater.* **6,** 497–500 (2007).
9. J. K. Lee, W. L. Ma, C. J. Brabec, J. Yuen, J. S. Moon, J. Y. Kim, K. Lee, G. C. Bazan, and A. J. Heeger: Processing Additives for Improved Efficiency from Bulk Heterojunction Solar Cells. *J. Am. Chem. Soc.* **130,** 3619–3623 (2008).
10. A. Pivrikas, H. Neugebauer, and N. S. Sariciftci: Influence of processing additives to nano-morphology and efficiency of bulk-heterojunction solar cells: A comparative review. *Sol. Energy* **85,** 1226–1237 (2011).
11. G. Li, Y. Yao, H. Yang, V. Shrotriya, G. Yang, and Y. Yang: 'Solvent Annealing' Effect in Polymer Solar Cells Based on Poly(3-hexylthiophene) and Methanofullerenes. *Adv. Funct. Mater.* **17,** 1636–1644 (2007).
12. L. Chang, H. W. A. Lademann, J.-B. Bonekamp, K. Meerholz, and A. J. Moulé: Effect of Trace Solvent on the Morphology of P3HT:PCBM Bulk Heterojunction Solar Cells. *Adv. Funct. Mater.* **21,** 1779–1787 (2011).
13. J. A. Amonoo, E. Glynos, X. C. Chen, and P. F. Green: An Alternative Processing Strategy for Organic Photovoltaic Devices Using a Supercritical Fluid. *J. Phys. Chem. C* **116,** 20708–20716 (2012).
14. A. M. Hiszpanski and L. Loo: Directing the film structure of organic semiconductors via post-deposition processing for transistor and solar cell applications. *Energy Environ. Sci.* (2013). doi:10.1039/C3EE42615G

15. K. Sivula, Z. T. Ball, N. Watanabe, and J. M. J. Fréchet: Amphiphilic Diblock Copolymer Compatibilizers and Their Effect on the Morphology and Performance of Polythiophene:Fullerene Solar Cells. *Adv. Mater.* **18,** 206–210 (2006).
16. C. Yang, J. K. Lee, A. J. Heeger, and F. Wudl: Well-defined donor–acceptor rod–coil diblock copolymers based on P3HT containing C60: the morphology and role as a surfactant in bulk-heterojunction solar cells. *J. Mater. Chem.* **19,** 5416–5423 (2009).
17. J. U. Lee, J. W. Jung, T. Emrick, T. P. Russell, and W. H. Jo: Morphology control of a polythiophene–fullerene bulk heterojunction for enhancement of the high-temperature stability of solar cell performance by a new donor–acceptor diblock copolymer. *Nanotechnology* **21,** 105201 (2010).
18. Z. Sun, K. Xiao, J. K. Keum, X. Yu, K. Hong, J. Browning, I. N. Ivanov, J. Chen, J. Alonzo, D. Li, B. G. Sumpter, E. A. Payzant, C. M. Rouleau, and D. B. Geohegan: PS-b-P3HT Copolymers as P3HT/PCBM Interfacial Compatibilizers for High Efficiency Photovoltaics. *Adv. Mater.* **23,** 5529–5535 (2011).
19. C. Renaud, S.-J. Mougnier, E. Pavlopoulou, C. Brochon, G. Fleury, D. Deribew, G. Portale, E. Cloutet, S. Chambon, L. Vignau, and G. Hadziioannou: Block Copolymer as a Nanostructuring Agent for High-Efficiency and Annealing-Free Bulk Heterojunction Organic Solar Cells. *Adv. Mater.* **24,** 2196–2201 (2012).
20. Y. Tao, B. McCulloch, S. Kim, and R. A. Segalman: The relationship between morphology and performance of donor–acceptor rod–coil block copolymer solar cells. *Soft Matter* **5,** 4219 (2009).
21. R. A. Segalman, B. McCulloch, S. Kirmayer, and J. J. Urban: Block Copolymers for Organic Optoelectronics. *Macromolecules* **42,** 9205–9216 (2009).
22. N. Sary, F. Richard, C. Brochon, N. Leclerc, P. Lévêque, J.-N. Audinot, S. Berson, T. Heiser, G. Hadziioannou, and R. Mezzenga: A New Supramolecular Route for Using Rod-Coil Block Copolymers in Photovoltaic Applications. *Adv. Mater.* **22,** 763–768 (2010).
23. A. Yassar, L. Miozzo, R. Gironda, and G. Horowitz: Rod–coil and all-conjugated block copolymers for photovoltaic applications. *Prog. Polym. Sci.* **38,** 791–844 (2013).
24. E. F. Palermo, H. L. van der Laan, and A. J. McNeil: Impact of π-conjugated gradient sequence copolymers on polymer blend morphology. *Polym. Chem.* **4,** 4606 (2013).
25. E. F. Palermo, S. B. Darling, and A. J. McNeil: π-Conjugated gradient copolymers suppress phase separation and improve stability in bulk heterojunction solar cells. *J. Mater. Chem. C* (2014). doi:10.1039/c3tc32512a
26. L.-M. Chen, Z. Xu, Z. Hong, and Y. Yang: Interface investigation and engineering – achieving high performance polymer photovoltaic devices. *J. Mater. Chem.* **20,** 2575–2598 (2010).
27. Y. S. Eo, H. W. Rhee, B. D. Chin, and J.-W. Yu: Influence of metal cathode for organic photovoltaic device performance. *Synth. Met.* **159,** 1910–1913 (2009).
28. V. D. Mihailetchi, P. W. M. Blom, J. C. Hummelen, and M. T. Rispens: Cathode dependence of the open-circuit voltage of polymer:fullerene bulk heterojunction solar cells. *J. Appl. Phys.* **94,** 6849–6854 (2003).
29. B. Qi and J. Wang: Open-circuit voltage in organic solar cells. *J. Mater. Chem.* **22,** 24315–24325 (2012).
30. R. Po, C. Carbonera, A. Bernardi, and N. Camaioni: The role of buffer layers in polymer solar cells. *Energy Environ. Sci.* **4,** 285–310 (2011).

31. G. Heimel, L. Romaner, E. Zojer, and J.-L. Brédas: Toward Control of the Metal−Organic Interfacial Electronic Structure in Molecular Electronics: A First-Principles Study on Self-Assembled Monolayers of π-Conjugated Molecules on Noble Metals. *Nano Lett.* **7,** 932–940 (2007).
32. C. He, C. Zhong, H. Wu, R. Yang, W. Yang, F. Huang, G. C. Bazan, and Y. Cao: Origin of the enhanced open-circuit voltage in polymer solar cells via interfacial modification using conjugated polyelectrolytes. *J. Mater. Chem.* **20,** 2617–2622 (2010).
33. H. Wang, E. D. Gomez, Z. Guan, C. Jaye, M. F. Toney, D. A. Fischer, A. Kahn, and Y.-L. Loo: Tuning Contact Recombination and Open-Circuit Voltage in Polymer Solar Cells via Self-Assembled Monolayer Adsorption at the Organic–Metal Oxide Interface. *J. Phys. Chem. C* (2013). doi:10.1021/jp406625e
34. Y. He, H.-Y. Chen, J. Hou, and Y. Li: Indene−C 60 Bisadduct: A New Acceptor for High-Performance Polymer Solar Cells. *J. Am. Chem. Soc.* **132,** 1377–1382 (2010).
35. G. Zhao, Y. He, and Y. Li: 6.5% Efficiency of Polymer Solar Cells Based on poly(3-hexylthiophene) and Indene-C60 Bisadduct by Device Optimization. *Adv. Mater.* **22,** 4355–4358 (2010).
36. Y.-H. Lin, Y.-T. Tsai, C.-C. Wu, C.-H. Tsai, C.-H. Chiang, H.-F. Hsu, J.-J. Lee, and C.-Y. Cheng: Comparative study of spectral and morphological properties of blends of P3HT with PCBM and ICBA. *Org. Electron.* **13,** 2333–2341 (2012).
37. J. R. Locke and A. J. McNeil: Syntheses of Gradient π-Conjugated Copolymers of Thiophene. *Macromolecules* **43,** 8709–8710 (2010).
38. H. Hoppe, T. Glatzel, M. Niggemann, A. Hinsch, M. C. Lux-Steiner, and N. S. Sariciftci: Kelvin Probe Force Microscopy Study on Conjugated Polymer/Fullerene Bulk Heterojunction Organic Solar Cells. *Nano Lett.* **5,** 269–274 (2005).
39. K. Maturová, M. Kemerink, M. M. Wienk, D. S. H. Charrier, and R. A. J. Janssen: Scanning Kelvin Probe Microscopy on Bulk Heterojunction Polymer Blends. *Adv. Funct. Mater.* **19,** 1379–1386 (2009).
40. Y. Zhou, C. Fuentes-Hernandez, J. Shim, J. Meyer, A. J. Giordano, H. Li, P. Winget, T. Papadopoulos, H. Cheun, J. Kim, M. Fenoll, A. Dindar, W. Haske, E. Najafabadi, T. M. Khan, H. Sojoudi, S. Barlow, S. Graham, J.-L. Bredas, S. R. Marder, A. Kahn, and B. Kippelen: A Universal Method to Produce Low-Work Function Electrodes for Organic Electronics. *Science* **336,** 327–332 (2012).
41. S. Ko, E. T. Hoke, L. Pandey, S. Hong, R. Mondal, C. Risko, Y. Yi, R. Noriega, M. D. McGehee, J.-L. Brédas, A. Salleo, and Z. Bao: Controlled Conjugated Backbone Twisting for an Increased Open-Circuit Voltage while Having a High Short-Circuit Current in Poly(hexylthiophene) Derivatives. *J. Am. Chem. Soc.* **134,** 5222–5232 (2012).
42. G. H. Fredrickson and J. P. Donley: Influence of broken conformational symmetry on the surface enrichment of polymer blends. *J. Chem. Phys.* **97,** 8941–8946 (1992).
43. M. Sikka, N. Singh, A. Karim, F. S. Bates, S. K. Satija, and C. F. Majkrzak: Entropy-driven surface segregation in block copolymer melts. *Phys. Rev. Lett.* **70,** 307–310 (1993).
44. P. Brant, A. Karim, J. F. Douglas, and F. S. Bates: Surface Composition of Amorphous and Crystallizable Polyethylene Blends As Measured by Static SIMS. *Macromolecules* **29,** 5628–5634 (1996).
45. A. J. Mozer, N. S. Sariciftci, L. Lutsen, D. Vanderzande, R. Österbacka, M. Westerling, and G. Juška: Charge transport and recombination in bulk heterojunction solar cells studied by

the photoinduced charge extraction in linearly increasing voltage technique. *Appl. Phys. Lett.* **86,** 112104 (2005).
46. L. F. Drummy, R. J. Davis, D. L. Moore, M. Durstock, R. A. Vaia, and J. W. P. Hsu: Molecular-Scale and Nanoscale Morphology of P3HT:PCBM Bulk Heterojunctions: Energy-Filtered TEM and Low-Dose HREM †. *Chem. Mater.* **23,** 907–912 (2011).
47. D. R. Kozub, K. Vakhshouri, L. M. Orme, C. Wang, A. Hexemer, and E. D. Gomez: Polymer Crystallization of Partially Miscible Polythiophene/Fullerene Mixtures Controls Morphology. *Macromolecules* **44,** 5722–5726 (2011).
48. T. P. Russell: Copolymers at surfaces and interfaces. *Curr. Opin. Colloid Interface Sci.* **1,** 107–115 (1996).
49. M. D. Lefebvre, C. M. Dettmer, R. L. McSwain, C. Xu, J. R. Davila, R. J. Composto, S. T. Nguyen, and K. R. Shull: Effect of Sequence Distribution on Copolymer Interfacial Activity. *Macromolecules* **38,** 10494–10502 (2005).
50. L. Leibler: Emulsifying effects of block copolymers in incompatible polymer blends. *Makromol. Chem. Macromol. Symp.* **16,** 1–17 (1988).
51. S. H. Anastasiadis, I. Gancarz, and J. T. Koberstein: Compatibilizing effect of block copolymers added to the polymer/polymer interface. *Macromolecules* **22,** 1449–1453 (1989).
52. D. Kipp and V. Ganesan: Influence of Block Copolymer Compatibilizers on the Morphologies of Semiflexible Polymer/Solvent Blends. *J. Phys. Chem. B* (2014). doi:10.1021/jp501207y
53. Z. Xu, L.-M. Chen, G. Yang, C.-H. Huang, J. Hou, Y. Wu, G. Li, C.-S. Hsu, and Y. Yang: Vertical Phase Separation in Poly(3-hexylthiophene): Fullerene Derivative Blends and its Advantage for Inverted Structure Solar Cells. *Adv. Funct. Mater.* **19,** 1227–1234 (2009).
54. A. Maurano, R. Hamilton, C. G. Shuttle, A. M. Ballantyne, J. Nelson, B. O'Regan, W. Zhang, I. McCulloch, H. Azimi, M. Morana, C. J. Brabec, and J. R. Durrant: Recombination Dynamics as a Key Determinant of Open Circuit Voltage in Organic Bulk Heterojunction Solar Cells: A Comparison of Four Different Donor Polymers. *Adv. Mater.* **22,** 4987–4992 (2010).
55. D. Credgington and J. R. Durrant: Insights from Transient Optoelectronic Analyses on the Open-Circuit Voltage of Organic Solar Cells. *J. Phys. Chem. Lett.* **3,** 1465–1478 (2012).
56. B. P. Lyons, N. Clarke, and C. Groves: The relative importance of domain size, domain purity and domain interfaces to the performance of bulk-heterojunction organic photovoltaics. *Energy Environ. Sci.* **5,** 7657–7663 (2012).
57. D. Ma, M. Lv, M. Lei, J. Zhu, H. Wang, and X. Chen: Self-Organization of Amine-Based Cathode Interfacial Materials in Inverted Polymer Solar Cells. *ACS Nano* (2014). doi:10.1021/nn4059067
58. H. Wang, M. Shah, V. Ganesan, M. L. Chabinyc, and Y.-L. Loo: Tail State-Assisted Charge Injection and Recombination at the Electron-Collecting Interface of P3HT:PCBM Bulk-Heterojunction Polymer Solar Cells. *Adv. Energy Mater.* **2,** 1447–1455 (2012).

CHAPTER III:
MACROSCOPIC ALIGNMENT OF POLYMER CHAINS

Reprinted with permission from:

A. Li, D. Bilby, B. X. Dong, J. Amonoo, J. Kim, P. F. Green: Macroscopic alignment of poly(3-hexylthiophene) for enhanced long-range collection of photogenerated carriers. *J. Polym. Sci. Part B: Polym. Phys.* (2015). doi:10.1002/polb.23888

3.1. INTRODUCTION

Semiconducting polymers have tantalized the scientific community with their potential as versatile active materials for low-cost photovoltaics, organic electronics, and sensor applications. Despite significant progress made in the laboratory over the past two decades, their full potential has yet to be realized, and further advances are needed for them to have more important industrial and commercial impact.[1,2] One of the primary drawbacks of conjugated polymers and other disordered organic semiconductors is that their poor charge carrier mobilities typically limit device thicknesses/dimensions to 200 nm or less, which can pose a challenge for large-scale fabrication, and in the case of photovoltaics, necessitate a trade-off between light absorption and charge transport.[3–5] Although there have been a few reported examples of specially designed donor polymers exhibiting high mobilities (0.01 to 1 $cm^2V^{-1}s^{-1}$), incorporating thicker films (> 300 nm) to improve light absorption has yet to yield commensurate increases in the harvested photocurrent.[6–9]

One approach to address this challenge is to manipulate the morphologies of polymers to exploit their anisotropic properties.[10,11] Charge conduction in π-conjugated materials is enhanced by structural order, which enables greater delocalization of adjacent π orbitals and thereby facilitating carrier transport. For polymers, the most favorable transport occurs along the π-conjugated backbone of a single chain.[12] Greater linearity/planarity of the chain improves electronic coupling and carrier transport, whereas bends/twists disrupt backbone conjugation and hinder transport. Interchain transport can also occur with reasonable facility within ordered aggregates/crystallites via overlapping orbitals in the π-stacking direction. Conjugated polymers are semicrystalline, and because conventionally-fabricated films lack long-range order, macroscopic charge migration requires combination of intrachain and interchain transport through both crystalline and amorphous regions. Recently it has been proposed that above a minimum threshold fraction of ordered domains and sufficiently long chains, carriers can efficiently travel from one highly-ordered phase to another, using interconnecting tie chains to traverse the disordered regions.[13,14]

To further improve carrier mobilities and enable long-range transport in conjugated polymers, a growing number of creative strategies have been developed to align chains over extended length scales. This would allow carriers to travel larger distances following the most efficient intrachain pathways. Large-area alignment can be achieved using casting techniques such as directional solidification, solution shearing, and microchannel confinement, yielding anisotropic, and in some cases substantially improved, carrier mobilities.[10,15–17] Mechanical post-processing techniques such as stamping, rubbing, and straining have also been shown to induce polymer chains to adopt highly aligned configurations.[18–22] Molecular design of polymers

exhibiting liquid crystalline behavior has also been used to supplement the effectiveness of alignment techniques.[16,23]

The aforementioned macroscopic alignment techniques focus on in-plane alignment, but for some applications, such as organic photovoltaics, transport along the out-of-plane or "vertical" direction is of greater interest. Vertical alignment of polymer chains, however, is difficult to achieve because the backbones tend to favor in-plane orientations due to interactions with the substrate.[24,25] Template-based techniques have been successfully employed to induce vertical-alignment of polymer chains, such as nanoimprint lithography and infiltration of nano-porous anodized aluminum oxide.[26–30] While these novel strategies are promising, additional fabrication challenges are introduced by the necessity of nano-patterned templates or molds.

In this study, we demonstrate a facile strategy for achieving macroscopic uniaxial alignment of the well-known conjugated polymer poly(3-hexylthiophene) (P3HT), using a combination of solvent additive-induced epitaxy and off-center spincoating. These aligned polymer films were incorporated into bilayer solar cells to experimentally probe the effect of long-range order on the transport of photo-generated charge carriers. Using photoconductive atomic force microscopy (pc-AFM), it was discovered that photo-generated charges were capable of migrating remarkable distances of hundreds of micrometers away from the site of photoexcitation; such length scales are far beyond what has typically been considered for organic semiconductors. Our results provide experimental validation for directed alignment as an effective strategy to enhance carrier transport capabilities of conjugated polymers by exploiting their inherent anisotropic properties. These insights open up new possibilities for polymer-based electronics, such as novel device geometries or dimensions that exceed traditional limitations.

3.2. EXPERIMENTAL

3.2.1. Fabrication and Optical Characterization of Aligned Polymer Films

Poly(3-hexylthiophene) (P3HT) was used as-received (Rieke Metals, RMI-001 EE) to prepare solutions 10 mg/mL in chlorobenzene (CB). Following the work of Müller et al., the crystallizable solvent 1,3,5-trichlorobenzene (TCB) was added at a concentration of 4 vol% to the P3HT/CB solution to induce epitaxial crystallization with the polymer chains radially-oriented relative to the TCB nucleation sites.[31] The TCB-induced epitaxial crystallization is supplemented with an off-center spin-coating technique similar to the one described by Yuan et al.[32,33] Two 0.5" x 0.5" substrates are taped onto either end of a supporting 3-inch glass slide, which is centered on the spincoater stage. The P3HT solution is dropped onto the smaller taped substrates and the assembly is subsequently spun at 500 rpm for 30 s (diagram shown in Supporting Information Figure S1). The directional shear produced by spin-casting reproducibly yields films with two sections or "grains": one at the outer edge of the substrate with alignment parallel to the spinning direction, and one large grain with alignment perpendicular to the spinning direction. The unaligned P3HT films were cast conventionally from CB only, with the substrate centered directly on the spincoater (1000 rpm/30s), yielding film thicknesses ~70 nm.

The absorption anisotropy was characterized using a Varian Cary 50 Bio UV-Visible spectrophotometer. A polarizer film was placed between the sample and excitation light source; baseline and sample absorption scans were taken for each orientation (parallel and perpendicular polarizations). The absorbance (A) was calculated from the transmittance (T) using the relation $A = -\log(T)$. Optical microscopy was performed using an Olympus BX-50 microscope with polarized visible or UV light sources. Photoluminescence was also characterized using a Photon Technologies International Spectrophotometer with excitation and emission monochromators.

3.2.2. Fabrication and Photoconductive AFM Characterization of Bilayer Solar Cells

The bilayer solar cells used in this study were fabricated in an inverted architecture. ITO-coated glass (Delta Technologies, CG-50IN-S107) was cleaned by sonication in isopropanol and acetone for 10 min each, followed by a 10 min UV-ozone treatment. A cathode buffer layer of ethoxylated polyethyleneimine (PEIE) was spin-cast onto the ITO surface (0.4 wt% in methoxyethanol, 3000 rpm/30s) and dried at 100 °C for 10 minutes.[34] Next, phenyl-C_{61} butyric acid methyl ester (PCBM, American Dye Source, ASD61BFA) was spin-cast (30 mg/mL chlorobenzene, 1000 rpm/30s) and annealed at 150°C for 15 minutes, yielding a layer thickness of c.a. 85 nm. Since P3HT cannot be directly cast onto the PCBM layer due to similar solubility characteristics, we used a contact film transfer process to assemble the bilayer devices.[35] For this procedure, P3HT films were spin-cast on glass substrates pre-coated with a sacrificial layer of poly(sodium 4-styrenesulfonate) (PSS) (10 wt% in water, 4000 rpm/30s). Then the P3HT film is clamped onto the previously prepared PCBM film cofacially, with an edge exposed to allow the PSS layer to dissolve upon immersion in DI water. Finally, the original glass substrate for the P3HT film was slid off, and the completed device was dipped in water once more to remove residual PSS (diagram shown in Supporting Information Figure S2).

Photoconductive AFM (pc-AFM) was performed simultaneously with topographical scans using an Asylum Research MFP-3D in contact mode with a PtIr5-coated probe (NanoWorld) under short-circuit conditions (applied bias of 0 V). For each sample, a preliminary scan was performed in the dark to determine the current offset (typically ~125 pA) required to correct the dark current to zero; this offset is maintained for all subsequent measurements on the sample. Photoexcitation was provided by bottom illumination through the glass/ITO side using a 532 nm laser with an intensity of ~1 W/cm^2 and spot diameter of ~50 μm. The spot position was

adjusted by the built-in optics of the AFM stage; the distance between the beam spot and probe tip was approximated to an accuracy of ± 10 μm as viewed by the optical camera in the AFM head.

3.3.3. Thin Film Transistor Measurements

Thin film transistors were fabricated in top-contact configurations on substrates of highly doped Si with 300 nm of thermally-grown SiO_2 (Encompass Inc.), which were cleaned by sonicating in soap, DI water, acetone, Hellmanex solution (Sigma), isopropanol and boiling isopropanol for 5 min each. Cleaned substrates were UV-ozone treated for 20 min before immersing into a mixture of octadecyltrichlorosilane (OTS) and hexadecane (1:250 by volume) for 14 hours to grow a self-assembled monolayer of OTS. After OTS treatment, the substrates are further sonicated in toluene and isopropanol for 1 min each and then blow-dried under purified nitrogen gas to remove residual solvents. The treated substrates exhibited a contact angle of ~90^o with a water droplet, confirming hydrophobicity of the surface after OTS treatment. P3HT films were transferred onto the treated substrates using the same contact film transfer procedure previously described to assemble bilayer solar cells. Source and drain electrodes made of silver (Kurt J. Lesker) were vacuum deposited on top of the P3HT layer, using a shadow mask to produce transistor channel length and width of 50 μm and 500 μm, respectively. All TFT measurements were performed in an oxygen and moisture-free N_2-filled glove box.

3.3. RESULTS AND DISCUSSION

3.3.1. Morphology and Optical Characteristics of Aligned P3HT Films

By supplementing the TCB-induced epitaxy with directional shear generated by off-center spin-coating, we confined the nucleation of spherulites to the edges of the substrate,

yielding large “semi-spherulites” exhibiting centimeter-scale regions of uniaxially-aligned fibers as seen in **Figure 3.1** (a). These aligned P3HT films were viewed under optical microscopy, revealing a rough, grainy texture consisting of micron-scale fibrous structures (Fig. 3.1b). Additionally, the optical anisotropy of the aligned films is qualitatively evident from the contrast between images taken with the orientation of the polarizer parallel, versus perpendicular, to the alignment direction. The transmittance is much lower, due to greater light absorption, when the light is polarized parallel to the fibers. Since the π-π* transition occurs along the P3HT backbone, this indicates that the polymer chain alignment coincides with the direction of the fiber axes.[36]

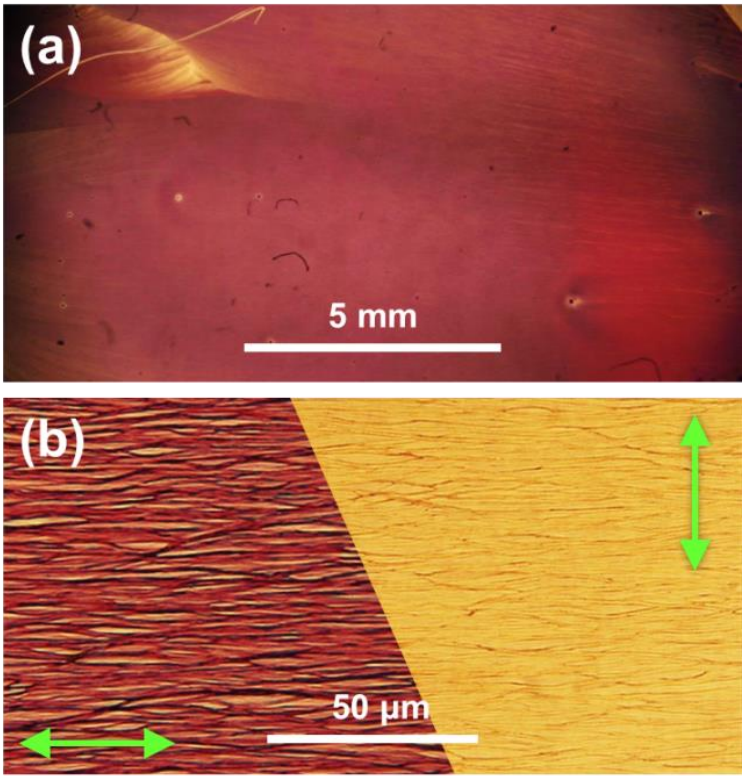

Figure 3.1 Polarized optical microscopy images taken at two different magnifications. At lower magnification (a), horizontal striations across image show alignment extending over a centimeter-scale region. At higher magnification (b), the non-uniform morphology becomes apparent, revealing the rough and fibrous microstructure. The left-hand side and right-hand side of the image correspond to the same region viewed with polarizer oriented parallel and perpendicular (indicated by the green arrows) to the fiber alignment.

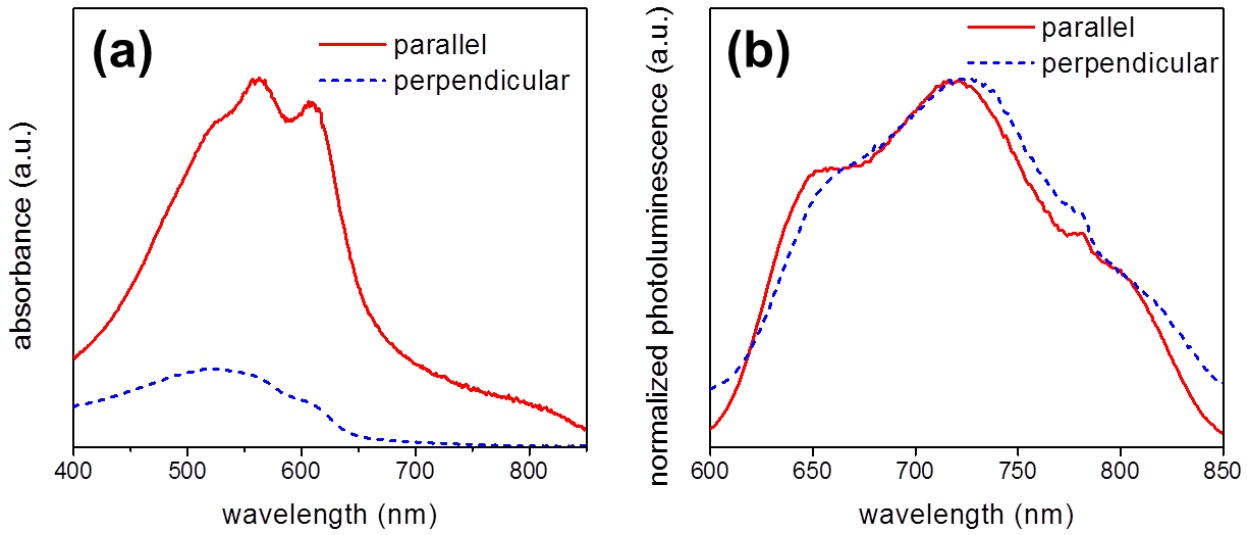

Figure 3.2 UV-vis absorption spectra of aligned P3HT films (a) with the light source polarized parallel or perpendicular to the alignment. The normalized photoluminescence emission spectra (b) with the shows a sharper peak at 645 nm (corresponding to the pure π-π* electronic transition of P3HT) when the excitation is parallel to the alignment.

One measure of the degree of alignment is the dichroic ratio between perpendicular absorption polarizations. The UV-visible absorption spectra in **Figure 3.2** quantitatively confirms that the P3HT film absorbs much more strongly when light is polarized along the alignment direction, with a dichroic ratio of 4.9 at 550 nm near the peak absorbance and 8.5 at 610 nm peak, indicative of a high degree of alignment. The appearance of a new absorption band near 850 nm for the parallel polarization appears to be a scattering-induced feature originating from the roughness of the film, and does not influence the electrical characteristics. If this new band were due to a change in the P3HT chromophore, one would expect to see a change in the shape of the photoluminescence. The normalized photoluminescence (PL) emission spectra shown in Figure 3.2b are similar in shape for excitations parallel and perpendicular to the alignment, and there is no peak near 850 nm. On the other hand, the PL peak near 650 nm (corresponding to the 1.9 eV bandgap of P3HT) is noticeably sharper for parallel light excitation. This is consistent with having well-aligned chains because this peak corresponds to the pure

electronic transition of the polymer rather than a vibronic or ordering band.[37] An exciton on an aligned backbone is more mobile than one on a twisted backbone, so it can more easily find a low-energy site on the backbone (from which it will emit) rather than transferring to a different chromophore (vibronic, etc.).

A closer examination of the microstructure using atomic force microscopy (**Figure 3.3**) revealed a morphology consisting of thick (diameter ~1 μm) fibers or bundles/aggregates of multiple smaller fibrils, separated by gaps in which there exists only a sparse matting of fibrils. In this highly heterogeneous structure, the thickness of the film ranges from over 200 nm on top of the thick fibers to ~10 nm within the inter-fiber gaps. Müller et al. have investigated the molecular orientation within P3HT spherulites cast from CB/TCB solution using GIWAXS; their findings suggest that crystallites exhibit comparable face-on and edge-on orientations.[31]

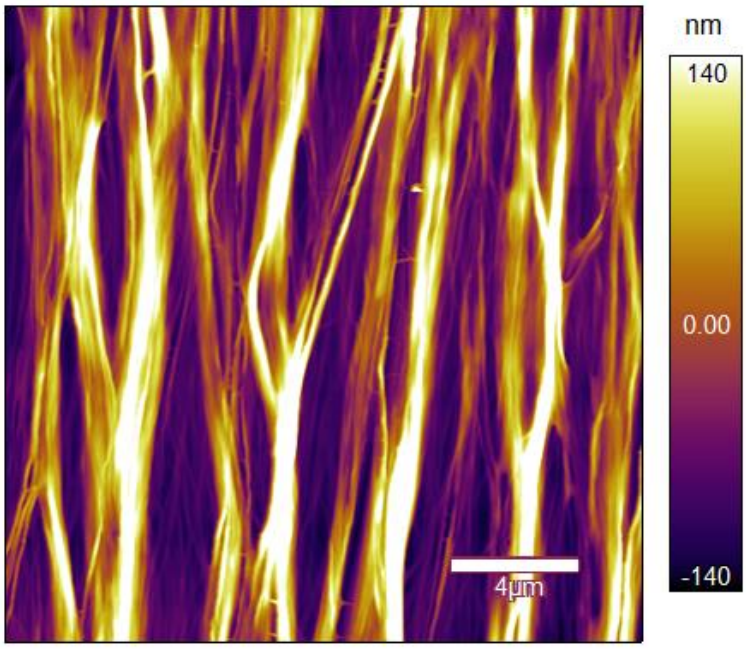

Figure 3.3 Topography of aligned P3HT film produced by off-center spincoating combined with TCB-induced epitaxy.

3.3.2. Long-Range Photocurrent in P3HT/PCBM Bilayer Solar Cells

Polymer alignment and absorption anisotropy both have important implications for photovoltaic device operation and performance. In order to isolate and investigate the effect of polymer alignment, we fabricated and characterized bilayer P3HT/PCBM solar cells (details in Experimental section). Although the planar heterojunction device architecture yields poor performance compared to the bulk heterojunction, casting the donor and acceptor layers separately helps to deconvolute the effect of polymer alignment from differences in donor/acceptor mixing and interfacial area that arise from the method of fabrication of aligned polymer films. In a prior study, Gupta et al. fabricated aligned polymer photodiodes and characterized the transient photocurrent behavior.[10] They reported photocurrent anisotropy in terms of the rates at which charges were swept out and extracted when fields were applied parallel versus perpendicular to the alignment direction. We employed a different approach, using photoconductive atomic force microscopy (pc-AFM), to map the local steady-state photocurrent under short-circuit conditions, while adjusting the distance between the laser spot (carrier excitation) and conductive probe (charge extraction). Upon exciton dissociation at the P3HT/PCBM planar heterojunction, electrons may take the direct path to the cathode (fully-coated ITO/PEIE substrate) whereas holes must travel, not only vertically (out-of-plane) to reach the top surface, but also laterally (in-plane) when the laser spot is offset from the AFM tip. Since the exciton diffusion length (~10 nm) is small in comparison to the laser spot size (~50 μm diameter) and laser-probe separation distances (100-400 μm), we consider exciton dissociation and free carrier generation to occur effectively within the laser spot. Under this assumption, any measured long-range photocurrent is primarily due to the migration of free carriers (holes) through the P3HT layer.

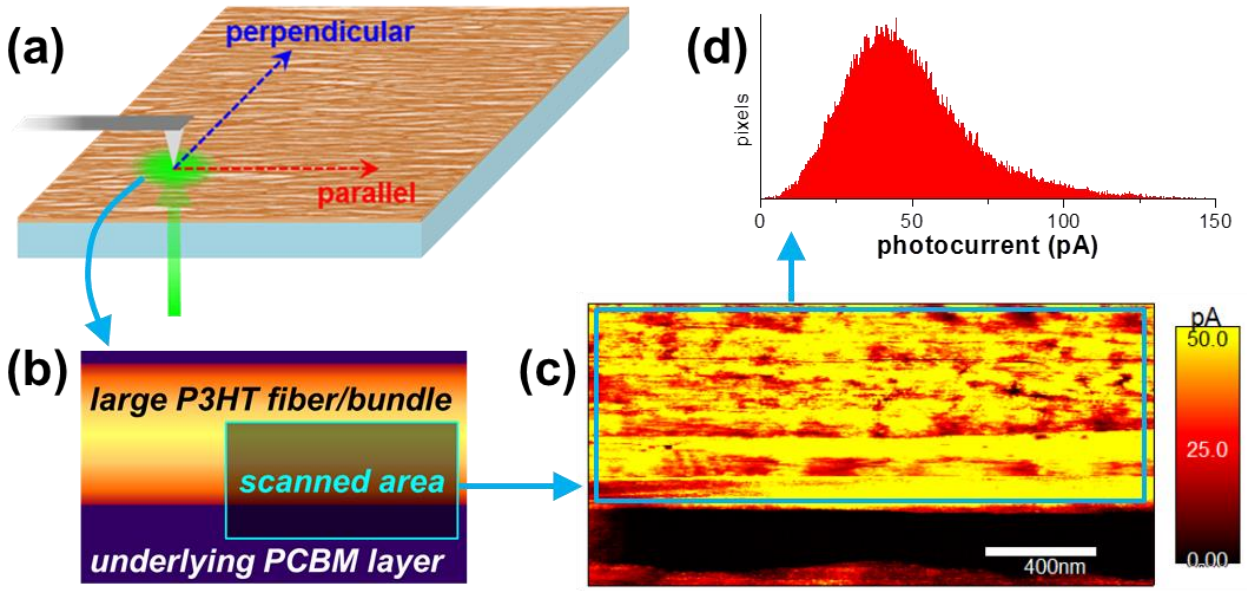

Figure 3.4 Schematic of the photoconductive AFM measurement setup (a), in which laser illumination from below can be focused on a spot directly on the scan region or displaced from it. For the measurements on the aligned device, the scan region was on the edge of a large fiber as illustrated in (b), and the photocurrent map under direct illumination is shown in (c). The distribution of photocurrent values measured at each pixel (excluding the off-fiber PCBM region) is plotted as a histogram in (d).

For pc-AFM measurements, illustrated schematically in **Figure 3.4**, we focused upon a small area at the edge of a large fiber (or bundle), identified by a steep drop in height observed in the simultaneously imaged topography. Scanning this area under direct laser illumination revealed a high level of photocurrent from the fiber and virtually none from the off-fiber region. The topography and photocurrent together suggested that, for this selected area, the off-fiber region is essentially devoid of P3HT and consists of only the underlying PCBM layer, which does not contribute to hole generation or transport. We infer that the contact film transfer process resulted in the removal of portions of the thin sublayer of P3HT between the larger fibers (present in the as-cast aligned film shown in Fig. 3.3), thereby exposing the PCBM.

After the photocurrent measurements under direct illumination were complete, the laser was refocused on a spot away from the AFM tip in the direction parallel to the alignment; the

same region of the sample was sequentially scanned with the laser spot approximately 200 μm and 400 μm away (distances estimated from the center of the laser spot to the center of the scanned region). The laser spot was then returned to its original position (focused directly on the AFM tip), and the zero-offset scan was repeated, yielding photocurrent values that were similar to those of the original scan. This indicated that device degradation and tip wearing/fouling were relatively insignificant within the span of the experiment. Subsequently, photocurrent scans were performed for perpendicular laser offsets of 200 μm and 400 μm. Finally, as a baseline comparison, a third series of measurements were performed on a reference device with an unaligned P3HT layer. Shorter laser-tip separations of 100 μm and 140 μm were used, because the photocurrent decayed to near undetectable values at larger distances. Additionally, due to the in-plane isotropy of the unaligned polymer, there was no distinction between parallel and perpendicular orientations.

To extract quantitative characteristic values from these scans, histograms were generated from the distributions of photocurrent values measured at each pixel of the region of the image on the fiber (the off-fiber region with essentially zero photocurrent was excluded). The histogram distributions were fitted with a Gaussian function to approximate the peak photocurrent value for each laser-probe separation distance; these representative values are compiled and plotted in **Figure 3.5**. At first glance, the most noticeable difference between the devices is the photocurrent value at a distance $d = 0$ (under direct laser illumination), which is over four times larger for the aligned than the unaligned sample. However, it is important to recall that this is a localized measurement, and the high photocurrent extracted directly from a fiber, which benefits from locally enhanced light absorption (locally higher crystallinity and thickness as compared to the uniform unaligned film), is not maintained across the entire aligned film (recall from Figure

4c that there is virtually no photocurrent from the off-fiber region). Since the aim of this study is to investigate the long-range photo-carrier transport, rather than their generation, we focus instead upon the rate at which the photocurrent decays with increasing distance from the site of photo-excitation.

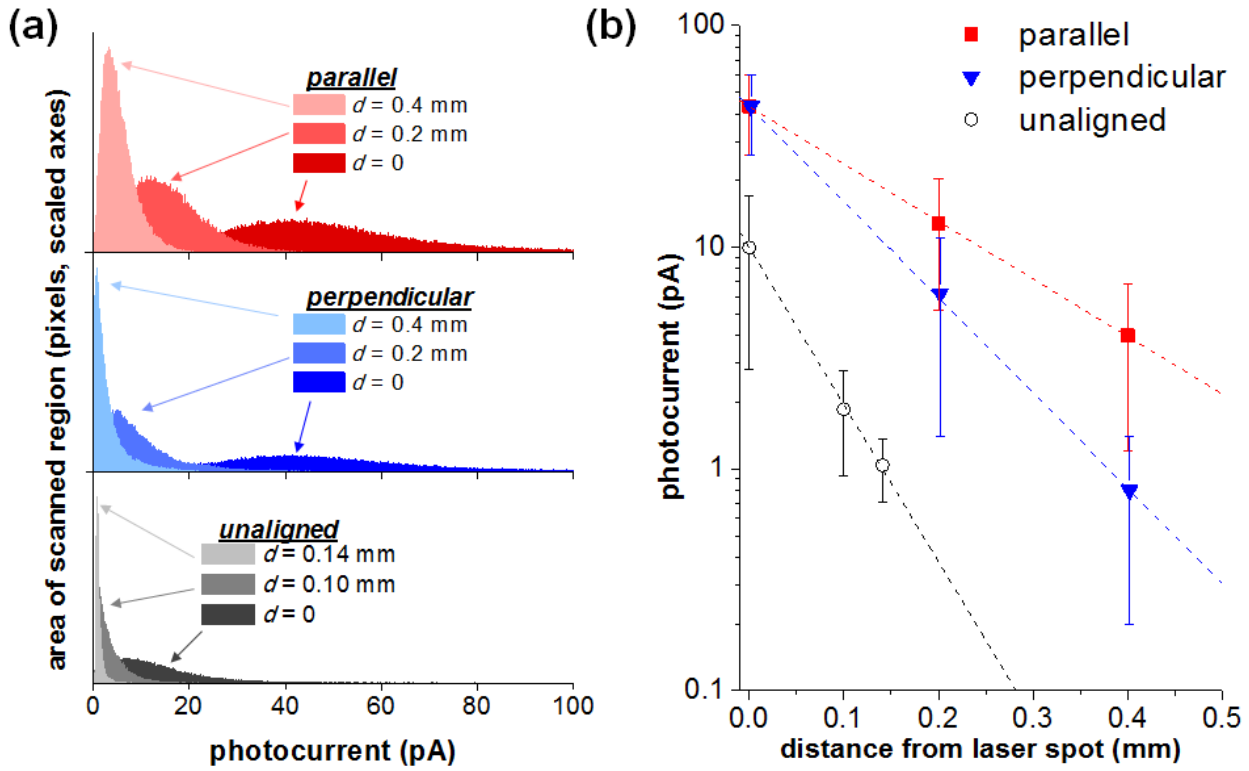

Figure 3.5 (a) Histograms of the distributions of photocurrents measured at varying distances from the laser spot for the parallel and perpendicular directions to the fibers in the aligned sample, and the unaligned sample (no distinction for parallel vs perpendicular). Representative photocurrent values for each case are plotted together in (b), in which the data points and error bars correspond to the peaks and standard deviations, respectively, calculated from Gaussian fittings to the histogram distributions. The dotted lines are fits to an exponential decay.

In the reference device possessing an unaligned P3HT layer, the photocurrent unsurprisingly decreases sharply with increasing distance from the photoexcitation, falling below 10% of its "original" value (measured within the laser spot) at a distance of c.a. 140 μm. In contrast, for the device possessing an aligned P3HT layer, the photocurrent retains 30% of its

original value at a distance of 200 μm (parallel to the alignment direction) from the laser spot, and does not fall to 10% until a distance of nearly 400 μm. The spatial decay is anisotropic, with more rapid decrease in photocurrent along the direction perpendicular to the alignment, but it is still less severe than in the unaligned case. In all three cases, the decrease in photocurrent with increasing distance appears to follow a trend of exponential decay, which can potentially be explained by a charge diffusion model. Since the electric field within the device is defined by and concentrated between the two electrodes (ITO substrate and AFM tip), it is orthogonal to the in-plane/lateral hole transport.[38]

Given negligible in-plane electric-field, diffusion of photo-generated carriers would thus be expected to follow an exponential decay with lateral distance from the excitation source.[39] By fitting an exponential function to each set of data, we can extract the decay coefficients to semi-quantitatively compare their respective efficiencies of long-range photo-carrier transport. As an analogy to the dichroic ratio for optical absorbance, the "anisotropy factor" from a simple ratio of parallel to perpendicular decay coefficients is ~1.7. In contrast, the decay coefficient for the unaligned case is nearly three times larger than that of the aligned-parallel case. It may initially seem contradictory that photocurrent decays more rapidly in the unaligned polymer than in the perpendicular direction of the aligned polymer.

We hypothesize that long-range carrier migration perpendicular to the macroscopic alignment is facilitated by the high degree of interconnectivity between fibers. As previously shown in the AFM morphology (Fig. 3.3), although the fibers exhibit clear overall uniaxial alignment, locally they are not perfectly parallel to one another. There are many junctions where adjacent fibers contact/merge with each other, or conversely, branching points where one fiber splits into two. Previous work on aligned P3HT cast from CB/TCB solution have found a

significant fraction of edge-on crystallites,[31] which would provide π-stacked chains for interchain transport across fiber axes or between adjacent fibers.[40,41] This would enable carriers to follow a zig-zag route, using the fiber interconnections to travel from one to another, while taking advantage of the highly efficient intrachain pathways along the fibers to reach the next junction. **Figure 3.6** this proposed carrier transport scenario, where a combination of intrachain transport along fibers and interchain transport across/between fibers yields net migration in perpendicular to the macroscopic alignment.

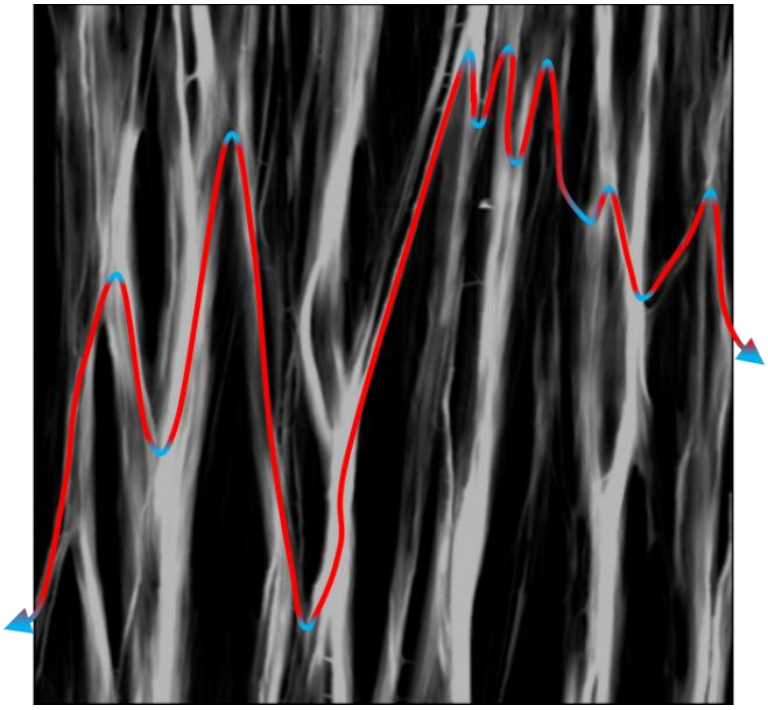

Figure 3.6 Proposed pathway for carrier migration perpendicular to the direction of alignment, overlaying the fiber morphology previously shown in Figure 3. The straight portions of this pathway (red) occur along individual fibers and are dominated by rapid intrachain transport. The bends (blue) require interchain transport along π-stacked chains.

To verify that the enhanced photocurrent collection following P3HT alignment was indeed due to increased long-range charge carrier diffusion, we performed photoluminescence optical microscopy to investigate the possibility of optical waveguiding effects through the fibers. The same 532 nm laser used for pc-AFM experiments was directed onto an aligned P3HT

film under a microscope in a non-normal reflection geometry, using light filters to separately image the incident laser spot and photoluminescent emission. As shown in **Figure 3.7**, the aligned fibrous P3HT film is only photoluminescent within the region under direct laser illumination. Furthermore, the emission exhibits no pronounced luminescence at fiber junctions or imperfections in the vicinity of the excitation, which would be expected if waveguide effects significantly contributed to long-range energy migration. Based on this test, we conclude that light-trapping effects are not the primary reason for the large increase in long-range charge collection.

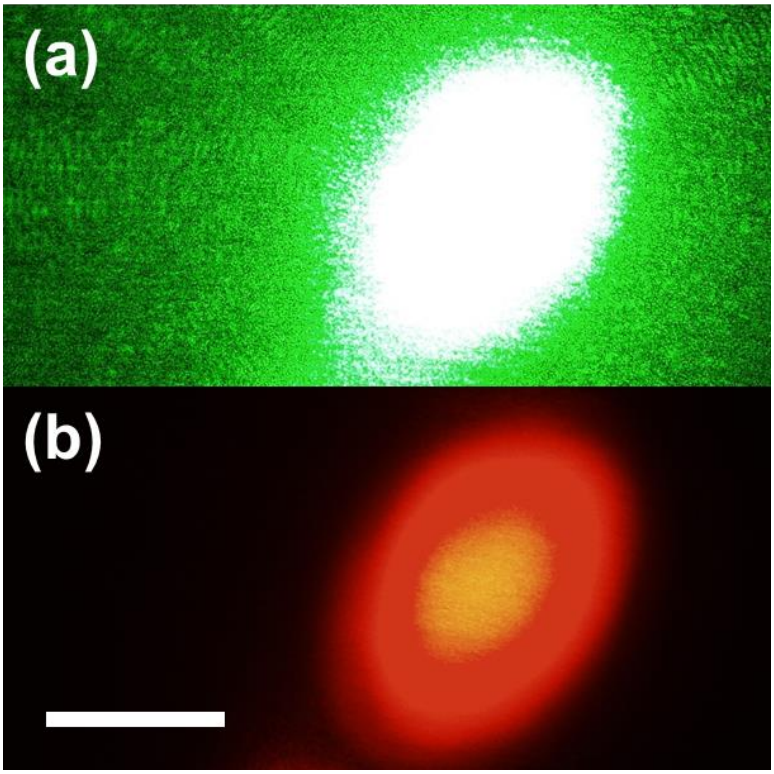

Figure 3.7 Photoluminescence optical microscopy of the aligned P3HT films showing (a) the incident laser spot and (b) the photoluminescent emission (scale bar is 500 μm). The spot is elliptical and much larger than in the photocurrent measurement due to the non-normal angle of the incident beam, longer traveled distance, and absence of the focusing optics provided by the AFM system.

3.3.3. In-Plane Hole Mobility of P3HT Transistors

Since the mobility and diffusion coefficient for charge carriers are proportional according to the Einstein relation, we expected that the anisotropy observed in the long-range photocurrent should be reflected in the carrier mobilities. To this end, we fabricated TFTs for both the aligned and unaligned P3HT, placing the polymer films onto OTS-treated silicon substrates using the same contact film transfer procedure in order to replicate the conditions under which the solar cells were fabricated. For the aligned samples, the source and drain electrodes were deposited such that the span of the transistor channel was either parallel or perpendicular to the alignment. The mobilities were extracted from the current measured at the drain (I_{DS}) by fitting the transfer curves in the saturation regime (drain voltage V_D = -80 V) according to:

$$I_{DS} = \frac{W C_i}{2L} \mu \left(V_g - V_t\right)^2$$

where W and L are the channel width and length (W = 500 μm, L = 50 μm), and C_i is the capacitance per unit area (C_i = 10 nF/cm^2 for 300 nm insulating SiO_2 layer).[42]

From these measurements, we obtain the hole mobility of the aligned P3HT in the parallel direction μ_{para} = 2.6 x 10^{-4} cm^{2}V^{-1}s^{-1} (±44%) and the mobility in the perpendicular direction μ_{perp} = 7.5 x 10^{-5} cm^{2}V^{-1}s^{-1} (±32%) (see Figure S6 for transfer curves). The ratio of μ_{para} and μ_{para} yields an anisotropy factor of ~3.5, which is larger but of comparable magnitude to the ~1.7 anisotropy factor found in the exponential decay coefficient for the photocurrent. This relatively moderate degree of anisotropy (one order of magnitude or less) is consistent with several previous studies on the in-plane mobilities of well-aligned conjugated polymers, where transport is dominated by either intrachain transport along the backbone or interchain transport along the π-stacking direction.[10,43,44] It is important, however, to recognize the limitations of these quantitatively measured mobilities, since the inhomogeneous morphology of the aligned films

make it difficult to accurately assess the effective channel lengths and widths. Nonetheless, these results suggest a relationship between the anisotropic mobility of macroscopically-aligned conjugated polymers and the long-range lateral migration of photo-excited carriers.

The unaligned P3HT was found to have a mobility of 3.2×10^{-2} $cm^2V^{-1}s^{-1}$, more than two orders of magnitude larger than the parallel and perpendicular mobilities of the aligned sample. This unexpectedly high mobility would appear at odds with the pc-AFM measurements, in which the unaligned device showed the steepest decline in photocurrent with increasing distance from the spot excited by the laser. There are several factors that may account for these seemingly contradictory observations. Following the earlier discussion, the surface roughness and non-uniformity of the aligned P3HT films could lead to an underestimation of their actual mobilities. This might arise from poor contact/coverage with the electrodes and substrate, as well as the aforementioned inaccuracies in channel length/width. Fundamental differences between the pc-AFM and TFT measurements could also complicate comparisons of the long-range photocurrent and mobilities. The photocurrents were measured in the absence of external fields, allowing carriers to freely drift/diffuse both laterally and vertically. In TFT measurements, carriers are pulled across the channel by the source-drain voltage difference, and transport is confined to the vicinity (~10 nm) of the substrate due to the applied gate voltage.[45] As a result, the TFT mobilities are much more sensitive to interfacial morphology and substrate interactions, which are expected to be quite different for the aligned and unaligned P3HT films.

These uncertainties highlight some of the challenges associated with correlating mobility with long-range charge migration in aligned P3HT fibers. They do not, however, detract from the pc-AFM measurements that directly illustrate the impressive degree of long-range carrier transport that is possible when conjugated polymer chains macroscopically aligned. Future work

on other polymer species or processing techniques may yield highly-oriented films without sacrificing smoothness/uniformity. This would help to elucidate some of these fundamental questions about carrier transport in conjugated polymers.

3.4. CONCLUSIONS

Using a combination of an epitaxy-inducing solvent additive and off-center spin-coating, we fabricated films consisting of macroscopic, uniaxially-aligned P3HT fibers. The high degree of alignment was verified by polarized optical spectroscopy, showing dichroic ratios of 4.9 and 8.5 at 550 nm and 610 nm, respectively. Aligned films were incorporated into bilayer solar cells, which were characterized by local photocurrent measurements using conductive AFM. Our results indicate that alignment of the conjugated polymer greatly enhances the ability of photo-generated carriers to migrate long distances from the site of charge generation. The enhancement was found to be strongest along the direction parallel to the alignment, where 10% of the original photocurrent was measured 400 μm away. To rationalize the behavior of these solar cells under a charge diffusion model, the carrier mobilities were measured for thin film transistor device analogues. A comparison of the mobilities along the parallel and perpendicular orientations of the aligned polymer revealed an anisotropy factor of ~3.5. Our findings highlight the connection between conjugated polymer morphology and carrier collection efficiency in photovoltaic devices, and demonstrate that macroscopic alignment can be a powerful strategy for enabling long-range carrier transport in traditionally low-mobility disordered organic semiconductors. This work motivates further development of polymer alignment techniques which would allow novel device architectures and configurations unconstrained by traditional limitations on active layer dimensions and geometries.

REFERENCES

1. D. Angmo and F. C. Krebs: Upscaling of Indium Tin Oxide (ITO)-Free Polymer Solar Cells : Performance, Scalability, Stability, and Flexibility. (2014).
2. C. J. Mulligan, M. Wilson, G. Bryant, B. Vaughan, X. Zhou, W. J. Belcher, and P. C. Dastoor: A projection of commercial-scale organic photovoltaic module costs. *Sol. Energy Mater. Sol. Cells* **120, Part A,** 9–17 (2014).
3. J. S. Moon, J. Jo, and A. J. Heeger: Nanomorphology of PCDTBT:PC70BM Bulk Heterojunction Solar Cells. *Adv. Energy Mater.* **2,** 304–308 (2012).
4. S. H. Park, A. Roy, S. Beaupré, S. Cho, N. Coates, J. S. Moon, D. Moses, M. Leclerc, K. Lee, and A. J. Heeger: Bulk heterojunction solar cells with internal quantum efficiency approaching 100%. *Nat. Photonics* **3,** 297–302 (2009).
5. G. Li, Y. Yao, H. Yang, V. Shrotriya, G. Yang, and Y. Yang: 'Solvent Annealing' Effect in Polymer Solar Cells Based on Poly(3-hexylthiophene) and Methanofullerenes. *Adv. Funct. Mater.* **17,** 1636–1644 (2007).
6. J. Peet, L. Wen, P. Byrne, S. Rodman, K. Forberich, Y. Shao, N. Drolet, R. Gaudiana, G. Dennler, and D. Waller: Bulk heterojunction solar cells with thick active layers and high fill factors enabled by a bithiophene-co-thiazolothiazole push-pull copolymer. *Appl. Phys. Lett.* **98,** 043301 (2011).
7. W. Li, K. H. Hendriks, W. S. C. Roelofs, Y. Kim, M. M. Wienk, and R. A. J. Janssen: Efficient Small Bandgap Polymer Solar Cells with High Fill Factors for 300 nm Thick Films. *Adv. Mater.* **25,** 3182–3186 (2013).
8. L. Murphy, W. Hong, H. Aziz, and Y. Li: Organic photovoltaics with thick active layers (~800 nm) using a high mobility polymer donor. *Sol. Energy Mater. Sol. Cells* **114,** 71–81 (2013).
9. B. Lim, K.-J. Baeg, H.-G. Jeong, J. Jo, H. Kim, J.-W. Park, Y.-Y. Noh, D. Vak, J.-H. Park, J.-W. Park, and D.-Y. Kim: A New Poly(thienylenevinylene) Derivative with High Mobility and Oxidative Stability for Organic Thin-Film Transistors and Solar Cells. *Adv. Mater.* **21,** 2808–2814 (2009).
10. M. J. Lee, D. Gupta, N. Zhao, M. Heeney, I. McCulloch, and H. Sirringhaus: Anisotropy of Charge Transport in a Uniaxially Aligned and Chain-Extended, High-Mobility, Conjugated Polymer Semiconductor. *Adv. Funct. Mater.* **21,** 932–940 (2011).
11. B. T. O'Connor, O. G. Reid, X. Zhang, R. J. Kline, L. J. Richter, D. J. Gundlach, D. M. DeLongchamp, M. F. Toney, N. Kopidakis, and G. Rumbles: Morphological Origin of Charge Transport Anisotropy in Aligned Polythiophene Thin Films. *Adv. Funct. Mater.* **24,** 3422–3431 (2014).
12. D. S. Pearson, P. A. Pincus, G. W. Heffner, and S. J. Dahman: Effect of molecular weight and orientation on the conductivity of conjugated polymers. *Macromolecules* **26,** 1570–1575 (1993).
13. R. Noriega, J. Rivnay, K. Vandewal, F. P. V. Koch, N. Stingelin, P. Smith, M. F. Toney, and A. Salleo: A general relationship between disorder, aggregation and charge transport in conjugated polymers. *Nat. Mater.* **12,** 1038–1044 (2013).
14. S. Himmelberger and A. Salleo: Engineering semiconducting polymers for efficient charge transport. *MRS Commun.* **FirstView,** 1–13 (2015).
15. M. Brinkmann and J.-C. Wittmann: Orientation of Regioregular Poly(3-hexylthiophene) by Directional Solidification: A Simple Method to Reveal the Semicrystalline Structure of a Conjugated Polymer. *Adv. Mater.* **18,** 860–863 (2006).

16. B.-G. Kim, E. J. Jeong, J. W. Chung, S. Seo, B. Koo, and J. Kim: A molecular design principle of lyotropic liquid-crystalline conjugated polymers with directed alignment capability for plastic electronics. *Nat. Mater.* **12,** 659–664 (2013).
17. H.-R. Tseng, H. Phan, C. Luo, M. Wang, L. A. Perez, S. N. Patel, L. Ying, E. J. Kramer, T.-Q. Nguyen, G. C. Bazan, and A. J. Heeger: High-Mobility Field-Effect Transistors Fabricated with Macroscopic Aligned Semiconducting Polymers. *Adv. Mater.* **26,** 2993–2998 (2014).
18. B. O'Connor, R. J. Kline, B. R. Conrad, L. J. Richter, D. Gundlach, M. F. Toney, and D. M. DeLongchamp: Anisotropic Structure and Charge Transport in Highly Strain-Aligned Regioregular Poly(3-hexylthiophene). *Adv. Funct. Mater.* **21,** 3697–3705 (2011).
19. L. Hartmann, K. Tremel, S. Uttiya, E. Crossland, S. Ludwigs, N. Kayunkid, C. Vergnat, and M. Brinkmann: 2D Versus 3D Crystalline Order in Thin Films of Regioregular Poly(3-hexylthiophene) Oriented by Mechanical Rubbing and Epitaxy. *Adv. Funct. Mater.* **21,** 4047–4057 (2011).
20. O. Awartani, M. W. Kudenov, R. J. Kline, and B. T. O'Connor: In-Plane Alignment in Organic Solar Cells to Probe the Morphological Dependence of Charge Recombination. *Adv. Funct. Mater.* n/a–n/a (2015). doi:10.1002/adfm.201403377
21. L. Biniek, N. Leclerc, T. Heiser, R. Bechara, and M. Brinkmann: Large Scale Alignment and Charge Transport Anisotropy of pBTTT Films Oriented by High Temperature Rubbing. *Macromolecules* **46,** 4014–4023 (2013).
22. L. Biniek, S. Pouget, D. Djurado, E. Gonthier, K. Tremel, N. Kayunkid, E. Zaborova, N. Crespo-Monteiro, O. Boyron, N. Leclerc, S. Ludwigs, and M. Brinkmann: High-Temperature Rubbing: A Versatile Method to Align π-Conjugated Polymers without Alignment Substrate. *Macromolecules* **47,** 3871–3879 (2014).
23. H. Sirringhaus, R. J. Wilson, R. H. Friend, M. Inbasekaran, W. Wu, E. P. Woo, M. Grell, and D. D. C. Bradley: Mobility enhancement in conjugated polymer field-effect transistors through chain alignment in a liquid-crystalline phase. *Appl. Phys. Lett.* **77,** 406–408 (2000).
24. B. Huang, E. Glynos, B. Frieberg, H. Yang, and P. F. Green: Effect of Thickness-Dependent Microstructure on the Out-of-Plane Hole Mobility in Poly(3-Hexylthiophene) Films. *ACS Appl. Mater. Interfaces* **4,** 5204–5210 (2012).
25. B. X. Dong, B. Huang, A. Tan, and P. F. Green: Nanoscale Orientation Effects on Carrier Transport in a Low-Band-Gap Polymer. *J. Phys. Chem. C* **118,** 17490–17498 (2014).
26. K. M. Coakley, B. S. Srinivasan, J. M. Ziebarth, C. Goh, Y. Liu, and M. D. McGehee: Enhanced Hole Mobility in Regioregular Polythiophene Infiltrated in Straight Nanopores. *Adv. Funct. Mater.* **15,** 1927–1932 (2005).
27. M. Aryal, K. Trivedi, and W. (Walter) Hu: Nano-Confinement Induced Chain Alignment in Ordered P3HT Nanostructures Defined by Nanoimprint Lithography. *ACS Nano* **3,** 3085–3090 (2009).
28. J. S. Kim, Y. Park, D. Y. Lee, J. H. Lee, J. H. Park, J. K. Kim, and K. Cho: Poly(3-hexylthiophene) Nanorods with Aligned Chain Orientation for Organic Photovoltaics. *Adv. Funct. Mater.* **20,** 540–545 (2010).
29. D. Chen, W. Zhao, and T. P. Russell: P3HT Nanopillars for Organic Photovoltaic Devices Nanoimprinted by AAO Templates. *ACS Nano* **6,** 1479–1485 (2012).
30. Y. Yang, K. Mielczarek, M. Aryal, A. Zakhidov, and W. Hu: Nanoimprinted Polymer Solar Cell. *ACS Nano* **6,** 2877–2892 (2012).

31. C. Müller, M. Aghamohammadi, S. Himmelberger, P. Sonar, M. Garriga, A. Salleo, and M. Campoy-Quiles: One-Step Macroscopic Alignment of Conjugated Polymer Systems by Epitaxial Crystallization during Spin-Coating. *Adv. Funct. Mater.* **23,** 2368–2377 (2013).
32. Y. Yuan, G. Giri, A. L. Ayzner, A. P. Zoombelt, S. C. B. Mannsfeld, J. Chen, D. Nordlund, M. F. Toney, J. Huang, and Z. Bao: Ultra-high mobility transparent organic thin film transistors grown by an off-centre spin-coating method. *Nat. Commun.* **5,** (2014).
33. H. Wang, L. Chen, R. Xing, J. Liu, and Y. Han: Simultaneous Control over both Molecular Order and Long-Range Alignment in Films of the Donor–Acceptor Copolymer. *Langmuir* **31,** 469–479 (2015).
34. Y. Zhou, C. Fuentes-Hernandez, J. Shim, J. Meyer, A. J. Giordano, H. Li, P. Winget, T. Papadopoulos, H. Cheun, J. Kim, M. Fenoll, A. Dindar, W. Haske, E. Najafabadi, T. M. Khan, H. Sojoudi, S. Barlow, S. Graham, J.-L. Bredas, S. R. Marder, A. Kahn, and B. Kippelen: A Universal Method to Produce Low-Work Function Electrodes for Organic Electronics. *Science* **336,** 327–332 (2012).
35. A. Tada, Y. Geng, Q. Wei, K. Hashimoto, and K. Tajima: Tailoring organic heterojunction interfaces in bilayer polymer photovoltaic devices. *Nat. Mater.* **10,** 450–455 (2011).
36. M. C. Gurau, D. M. Delongchamp, B. M. Vogel, E. K. Lin, D. A. Fischer, S. Sambasivan, and L. J. Richter: Measuring Molecular Order in Poly(3-alkylthiophene) Thin Films with Polarizing Spectroscopies. *Langmuir* **23,** 834–842 (2007).
37. D. E. Motaung, G. F. Malgas, C. J. Arendse, S. E. Mavundla, and D. Knoesen: Structural and photo-physical properties of spin-coated poly(3-hexylthiophene) thin films. *Mater. Chem. Phys.* **116,** 279–283 (2009).
38. Z. Liu, N. Jiao, Z. Wang, and Z. Dong: Analysis on 3-Dimensional spatial electric field of AFM based anodic oxidation. in *2012 7th IEEE Int. Conf. NanoMicro Eng. Mol. Syst. NEMS* 547–552 (2012). doi:10.1109/NEMS.2012.6196835
39. R. Widenhorn, A. Weber-Bargioni, M. M. Blouke, A. J. Bae, and E. Bodegom: Charge diffusion in the field-free region of charge-coupled devices. *Opt. Eng.* **49,** 044401–044401–7 (2010).
40. R. J. Kline, M. D. McGehee, E. N. Kadnikova, J. Liu, J. M. J. Fréchet, and M. F. Toney: Dependence of Regioregular Poly(3-hexylthiophene) Film Morphology and Field-Effect Mobility on Molecular Weight. *Macromolecules* **38,** 3312–3319 (2005).
41. D. Kajiya, S. Ozawa, T. Koganezawa, and K. Saitow: Enhancement of Out-of-plane Mobility in P3HT Film by Rubbing: Aggregation and Planarity Enhanced with Low Regioregularity. *J. Phys. Chem. C* **119,** 7987–7995 (2015).
42. G. Horowitz: Organic Field-Effect Transistors. *Adv. Mater.* **10,** 365–377 (1998).
43. L. H. Jimison, M. F. Toney, I. McCulloch, M. Heeney, and A. Salleo: Charge-Transport Anisotropy Due to Grain Boundaries in Directionally Crystallized Thin Films of Regioregular Poly(3-hexylthiophene). *Adv. Mater.* **21,** 1568–1572 (2009).
44. D. Gupta, T. J. K. Brenner, S. Albert-Seifried, M. J. Lee, M. Heeney, I. McCulloch, and H. Sirringhaus: Photoconductivity anisotropy study in uniaxially aligned polymer based planar photodiodes. *Org. Electron.* **13,** 36–42 (2012).
45. F. Dinelli, M. Murgia, P. Levy, M. Cavallini, F. Biscarini, and D. M. de Leeuw: Spatially Correlated Charge Transport in Organic Thin Film Transistors. *Phys. Rev. Lett.* **92,** 116802 (2004).

CHAPTER IV:
CARRIER TRANSPORT IN DISORDERED MORPHOLOGIES

Reprinted with permission from:

A. Li, B. X. Dong, P. F. Green: Influence of Morphological Disorder on In- and Out-of-Plane Charge Transport in Conjugated Polymer Films. *MRS Comm.* (2015).

4.1. INTRODUCTION

Conjugated polymers are a widely-studied class of semicrystalline organic semiconductors, exhibiting very different morphologies and physical properties, depending on their method of fabrication. Typically, thin polymer films are deposited from solution, which is the simplest strategy and most amenable for high-throughput, low-cost fabrication. However, there are a number of situations wherein vacuum-based deposition provides advantages, such as creating patterned or multi-layered architectures, or in cases where the desired substrate or surface has poor wettability.[1,2] Conventional physical vapor deposition techniques are unsuitable, as they involve large energy input which generally degrades polymeric materials. In recent years however, an increasing number of groups have successfully fabricated polymer films using an analogue of pulsed laser deposition known as Matrix-Assisted Pulsed Laser Evaporation (MAPLE).[3–5] Rather than directly ablating solid polymer, the MAPLE process utilizes a frozen dilute solution of the polymer and volatile solvent. Under ideal circumstances, laser energy is

almost entirely absorbed by the host solvent "matrix", thereby preventing photochemical degradation of the guest polymer.

The MAPLE technique affords access to films with unique morphologies, associated with physical properties/phenomena, such as density and glass transition temperature, that differ from that of normal solvent cast films.[6,7] While interesting and promising findings have been reported for MAPLE-deposited conjugated polymers and nanocomposites for solar cells and other optoelectronic devices,[8–11] the fundamental relationships between morphology and electronic properties in such films remain poorly understood. Herein, we investigate the carrier transport characteristics of MAPLE-deposited P3HT films, both in-plane and out-of-plane, connecting the unusual behaviors with the unique morphologies. Whereas the in-plane carrier mobilities of MAPLE-deposited films are comparable to those of spin-cast analogues, the out-of-plane mobilities are an order of magnitude lower. The out-of-plane carrier transport is rationalized in terms of the well-established Gaussian Disorder Model (GDM), which describes carriers traversing through an environment characterized by both positional disorder, associated with the morphology, and energetic disorder (broadening of the density of states, originating from a distribution of conjugation lengths). Our results provide new insights into the role of structural and energetic disorder on the in-plane and out-of-plane carrier transport in conjugated polymer thin films.

4.2. RESULTS AND DISCUSSION

4.2.1. Matrix-Assisted Pulsed Laser Evaporation

Since the early development of the technique, the majority of MAPLE systems employed excimer lasers emitting UV wavelengths. Later it has been shown that UV lasers could degrade the dilute polymer guest; even when the chemical functionality was preserved, a reduction in

molecular weight (due to chain fragmentation) was often observed in the deposited material. Photochemical degradation is of particular concern for conjugated polymers, whose absorption extends all the way into the visible spectrum. To circumvent this problem, we employed resonant infrared (RIR-MAPLE).[12] Our MAPLE system (PVD Products) is equipped with an Er:YAG laser (Quantel) that produces a wavelength of 2.94 μm, well beyond the absorption edge of conjugated polymers and resonant with the vibrational stretching mode of hydroxyl bonds, making water the ideal solvent matrix. Since most conjugated polymers are not water-soluble, including the poly(3-hexylthiophene) (P3HT) used in this study (Rieke Metals, mol. wt. 50-70 kDa), we adopted an emulsion-based approach pioneered by the Stiff-Roberts group.[9,13] In this strategy, the polymer is first dissolved in a good organic solvent (5 mg/mL P3HT in 1,2-dichlorobenzene), then mixed with benzyl alcohol and DI water (containing 0.005 wt.% sodium dodecyl sulfate surfactant) at a 1:0.3:3 ratio, then shaken and ultrasonicated to generate a homogeneous emulsion. The emulsion is injected into a pre-cooled target cup (c.a. -170°C), and once it has been fully frozen, the chamber is pumped to high vacuum (< 2 x 10^{-5} torr). During deposition, the target is kept at a constant rotation while the laser (fluence of ~1.3 J/cm^2 at repetition rate of 5 Hz) is rastered across the surface for uniform ablation. The substrates are suspended face-down 5.5 cm above the target, and are also kept at a constant rotation to maintain uniform deposition.

4.2.2. Morphology and Optical Absorbance of MAPLE-Deposited Polymer Films

Atomic force microscopy (AFM) was used to characterize the morphologies of the MAPLE-deposited films. As shown in **Figure 4.1**, the surface of the film is quite rough and consists of globular features a distribution of sizes (diameters ranging from 50-200 nm). This

type of inhomogeneous globular morphology is consistent with those reported in previous MAPLE studies, arising from the mechanisms of target ablation and material transport to the substrate.[14,15] Films cast on Si substrates were floated by etching away the native oxide layer, via immersion in dilute hydrofluoric acid, and picked up onto new substrates with the formerly buried interface now exposed at the surface. AFM scans of these flipped films showed very similar globular features on the underside, suggesting that this type of morphology persists across the entire thickness of the film, again consistent with previously reported work.[7,16]

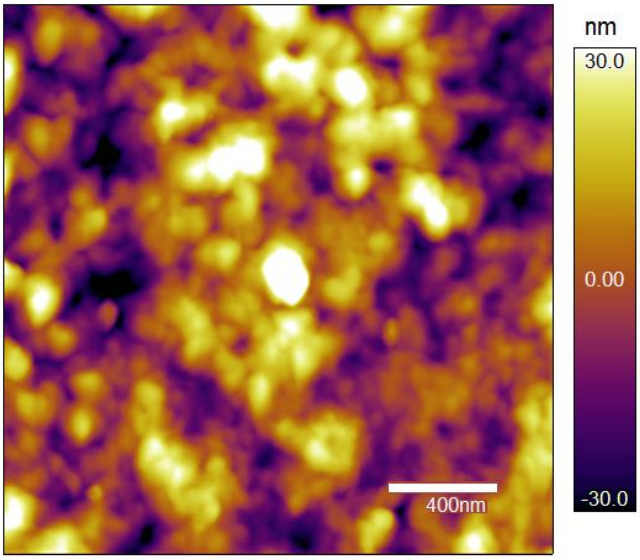

Figure 4.1. AFM topography (2 x 2 μm) of a MAPLE-deposited P3HT film.

The optical properties of spin-cast and MAPLE-deposited films (both with average thicknesses of c.a. 55 nm), were measured using UV-visible absorbance spectroscopy. In spite of the very different morphologies, compared to spin-cast films, the absorption spectrum of the MAPLE-deposited films are qualitatively similar, as shown in **Figure 4.2**. The total absorption can be deconvoluted into individual peaks by applying the Spano model, from which the exciton bandwidth W and Gaussian disorder parameter σ can be calculated.[17,18] Interestingly, although the σ value for the MAPLE-deposited film is larger than the spin-cast counterpart (82 versus 76

meV), the exciton bandwidths *W* are almost identical (107 meV) and comparable to values reported in literature for P3HT spin-cast from high boiling point solvents.[17,19] In the limit of weak excitonic coupling between cofacially-packed P3HT chains, the interchain coupling leads to the formation of vibronic bands characterized by an exciton bandwidth *W*. An increase in the conjugation length leads to greater exciton delocalization across polymer chains and reduces *W*.[20,21] The closely-matched values of *W* therefore suggest similar conjugation lengths, on average, between spin-cast and MAPLE-deposited samples. The larger magnitude of the disorder parameter σ, however, indicates a wider distribution of conjugation lengths, which most likely stems from a higher degree structural disorder and inhomogeneity (as suggested from the distribution of globule sizes) in MAPLE-deposited sample.

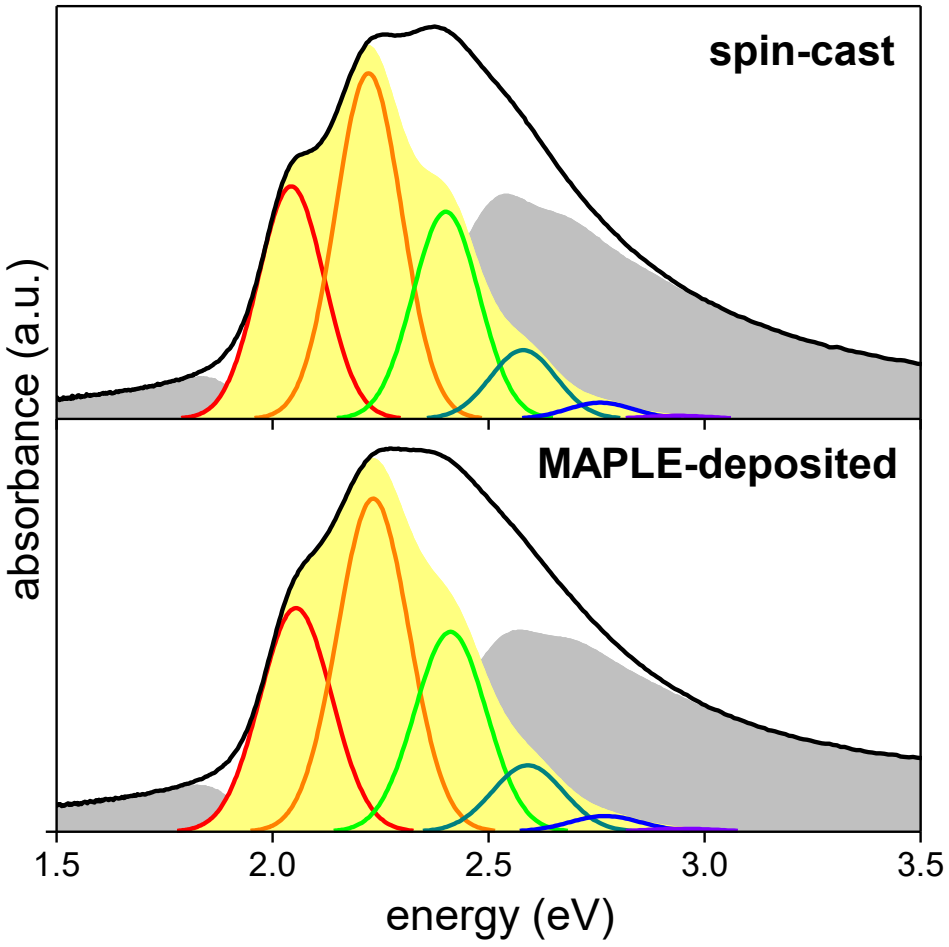

Figure 4.2 UV-vis absorption spectra for spin-cast and MAPLE-deposited P3HT films. The total absorption is shown by the black curve, and the yellow and gray shaded regions represent contributions from aggregate and amorphous fractions, respectively. Aggregate absorption is further decomposed into individual peaks (colored curves) fitted to the Spano model.

4.2.3. In-Plane Mobilities of Thin Film Transistors

To quantify the in-plane charge transport characteristics of P3HT films, thin film transistors (TFTs) were fabricated in top-contact, bottom-gate configuration on substrates of highly-doped Si with 300 nm of thermally-grown SiO_2 (Encompass Inc.). Prior to polymer deposition, substrates were cleaned by ultrasonication in soap, DI water, acetone, hot Hellmanex solution, isopropanol and boiling isopropanol for 5 min each, followed by UV-ozone cleaning for 20 min. Self-assembly monolayers of octadecyltrichlorosilane (OTS) (Sigma-Aldrich) were grown on the SiO_2 surface by immersing substrates in a mixture of OTS and hexadecane (1:250 by volume) for 14 hours while stirring. After depositing of polymer films (c.a. 50 nm thick), source and drain gold electrodes (Kurt J. Lesker, 99.99%) were vacuum-deposited on top of the polymer film at a rate of 0.5 A/s, using a shadow mask to generate transistor channel length and width of 50 μm and 500 μm, respectively. All TFT measurements were performed in an oxygen and moisture-free N_2-filled glove box using the Agilent 4156C Parameter Analyzer. The hole mobility μ was extracted from the drain current I_D by fitting the transfer curve in the saturation regime (V_D = -80 V) according to:

$$I_D = \frac{WC_i}{2L}\mu\left(V_g - V_t\right)^2 \tag{4.1}$$

where W and L are the channel width and length, C_i = 10 nF/cm^2 is the capacitance per unit area of the insulating SiO_2 layer, V_g and V_t are the gate and threshold voltages.

Shown in **Figure 4.3** are the transfer and output characteristics of TFTs fabricated from MAPLE-deposited P3HT films. Samples deposited on bare and OTS-treated substrates both show transfer curves with a clear onset of current and I_{on} / I_{off} ratio > 10^4. The output current

(Fig. 4.3 inset) also exhibits the typical transistor characteristics, showing a transition from linear to saturation behavior with increasing drain voltage. Transistor parameters for devices with spin-cast and MAPLE-deposited P3HT films are compared in **Table 4.1**.

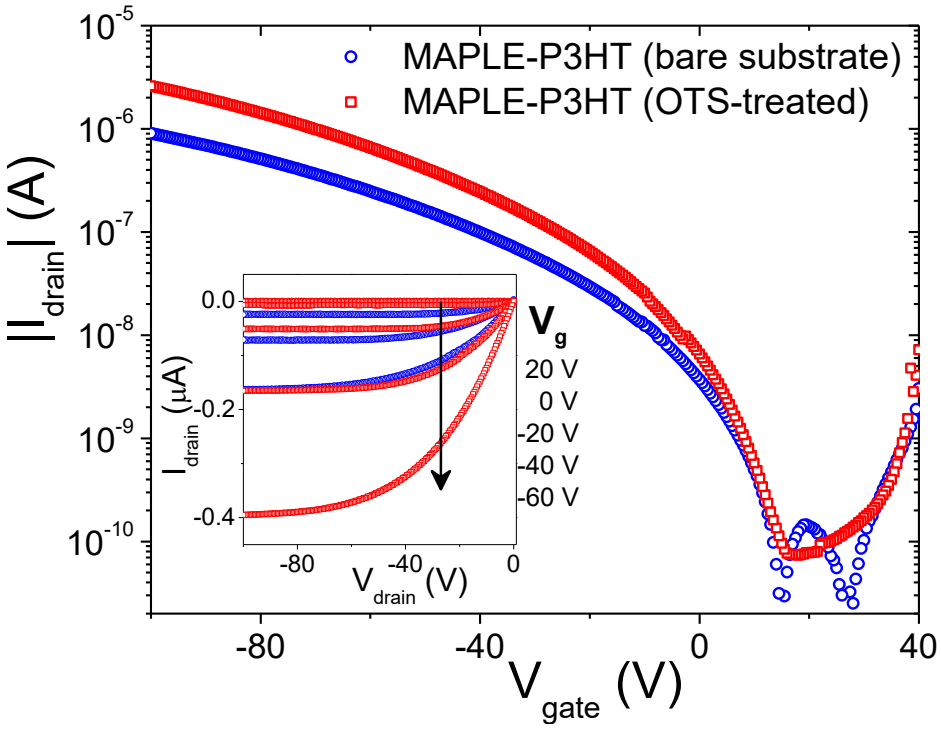

Figure 4.3 Transfer and output (inset) characteristics of transistors made from MAPLE-deposited P3HT on bare and OTS-treated substrates.

As shown in **Table 1**, the in-plane mobilities of MAPLE-deposited P3HT samples are comparable to those of spin-cast counterparts. In TFT measurements, the applied gate voltage draws carriers towards the substrate, and thus in-plane transport is primarily sensitive to the region of elevated carrier density within a few nanometers of the dielectric interface.[22] For the spin-coated devices, OTS treatment of the SiOx substrate produces nearly an order of magnitude increase in the hole mobility. This improvement is similar to results reported elsewhere, and has been attributed to improved ordering of polymer chains at the buried interface due to favorable interactions between the alkyl side chains and the self-assembled monolayer.[23,24] The MAPLE-

deposited devices, on the other hand, show less than a threefold enhancement in mobility following OTS treatment, which suggests that the morphology of MAPLE-deposited films is less sensitive to the chemistry of the surface upon which they are deposited.

Table 4.1 Summary of transistor parameters: on/off ratio (I_{on} / I_{off}), hole mobility (μ), threshold voltage (V_t) and subthreshold slope (S) for spin-cast and MAPLE-deposited devices, on bare and OTS-treated substrates. The values reported here were averaged over five different samples.

P3HT type	I_{on} / I_{off}	μ ($cm^2V^{-1}s^{-1}$)	V_t (V)	S (V/decade)*
spin-cast (bare substrate)	10^5	$(6.7 \pm 0.2) \times 10^{-4}$	-3 ± 1	-
spin-cast (OTS-treated)	10^4 - 10^5	$(5.5 \pm 0.3) \times 10^{-3}$	-3 ± 2	5.6
MAPLE (bare substrate)	10^5	$(2.7 \pm 0.2) \times 10^{-3}$	-16 ± 4	-
MAPLE (OTS-treated)	10^4 - 10^5	$(8.3 \pm 0.8) \times 10^{-3}$	-22 ± 3	6.4

* Subthreshold slope could not be fitted for devices on bare substrates due to nonlinearity

Another notable characteristic of MAPLE-deposited transistors, for both bare and OTS-treated substrates, is the large threshold voltage (V_t), calculated from the intercept of the linear regime with the voltage axis, as illustrated in the plot of $|I_{drain}|^{1/2}$ versus gate voltage in **Figure 4.4**. The subthreshold regime is ubiquitous in OFET transfer curves, and is associated with the presence of carrier traps or tail states within the band gap. In this regime mobility increases with the magnitude of V_g, as the rising carrier density fills trap states allowing more carriers to access delocalized states near the transport level. When V_g is sufficient to fill the density of states to the transport level mobility becomes constant.[25] The larger subthreshold slope S (reciprocal of the slope of $|I_D|^{1/2}$ vs V_g) and broader subthreshold regime of the MAPLE-deposited device reflect a more gradual turn-on transition while trap states are filled This is consistent with the larger degree of disorder indicated by UV-vis, which would produce a broader density of states and

require additional driving force from V_g to fill trapped tail states extending deeper into the band gap.

In spite of the larger subthreshold regime, we would like to emphasize that the linear regime mobilities of MAPLE-deposited P3HT samples are comparable to or higher than their spin-cast counterparts. This apparent decoupling of disorder and carrier mobilities is rather unusual, and may provide fresh insight regarding the extent to which structural disorder impacts charge transport. Indeed, the paradigm for engineering high-mobility polymers has evolved significantly over the past few years; in a recent review, Himmelberger and Salleo suggest that inevitable structural disorder in polymeric semiconductors does not necessarily prohibit efficient transport, and that future design of these materials should focus on "resilience" to disorder rather than trying to suppress it.[26]

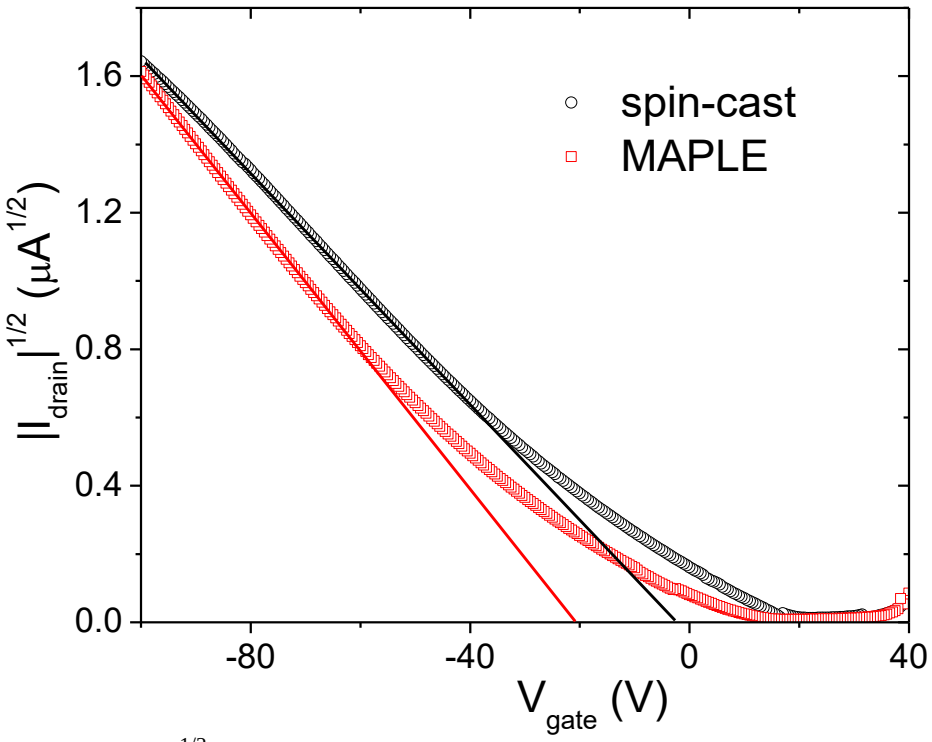

Figure 4.4 Plots of $|I|^{1/2}$ versus V_{gate} comparing MAPLE-deposited and spin-cast P3HT transistors (both on OTS-treated substrates). The solid lines represent the linear regimes from which mobilities are calculated.

4.2.4. Out-of-Plane Mobilities Measured by CELIV

For out-of-plane carrier mobility measurements, the technique of Charge Extraction by Linearly Increasing Voltage (CELIV) was employed.[27,28] CELIV holds advantages over traditional techniques such as Time of Flight (TOF) or Space Charged Limited Current (SCLC) measurements because of its ability to measure mobilities in films of submicron thickness films and films with defects and unintentional doping.[29,30] Triangle voltage ramps were generated by a BK Precision 4075 function generator, and the responded current was then amplified using a FEMTO amplifier before recorded by a Tektronix digital oscilloscope. All CELIV measurements were conducted in a vacuum cryostat (Janis Inc.). Shown in **Figure 4.5** are representative curves of current density versus time for spin-cast and MAPLE-deposited samples. In a CELIV measurement, there are two major contributions to the responded current: the displacement current $j(0)$ arising from the geometric capacitance of the sample, and the transient drift current $\Delta j = j - j(0)$ resulting from the extraction and flow of charge carriers within the film. The hole mobility μ is calculated using the drift current Δj, the displacement current $j(0)$, the film thickness h (c.a. 100 nm), the ramping rate A and the time t_{max} at which the current reaches a maximum value using the relation[31]

$$\mu = \frac{2h^2}{3At_{\max}^2(1+0.36\frac{\Delta j}{j(0)})} \tag{4.2}$$

To preface the discussion of out-of-plane carrier mobilities, it is important to recognize that CELIV and TFT measurements probe different regions of the film (bulk vs dielectric interface), which will necessarily lead to different results from in-plane mobilities. It can be immediately observed from the raw CELIV data that the time $t_{\max}$ corresponding to the peak of the transient current is longer for the MAPLE-deposited sample, corresponding to lower out-of-

plane carrier mobility according to Equation 4.2. The MAPLE sample also exhibits a pronounced broadening of the transient current, indicative of more dispersive transport than the spin-cast sample; this is consistent with higher structural disorder and a larger density of trap states. The electric field dependencies of mobilities (shown in the Fig. 4.5 inset) were determined by changing the voltage ramping rates, A (electric field $E = At_{max}/h$). Although the mobilities of the MAPLE-deposited sample are lower than those of the spin-cast sample, they both exhibit linear dependence on $E^{1/2}$, $\mu = \mu_{E=0} \exp(\beta E^{1/2})$, represented by the dashed lines in the plot. Additionally, the CELIV measurement reveals a weaker electric field dependence of out-of-plane mobility in the MAPLE-deposited sample (β = -3.6 x 10^{-3} $cm^{1/2}V^{-1/2}$ versus β = -7.0 x 10^{-3} $cm^{1/2}V^{-1/2}$ for spin-cast).

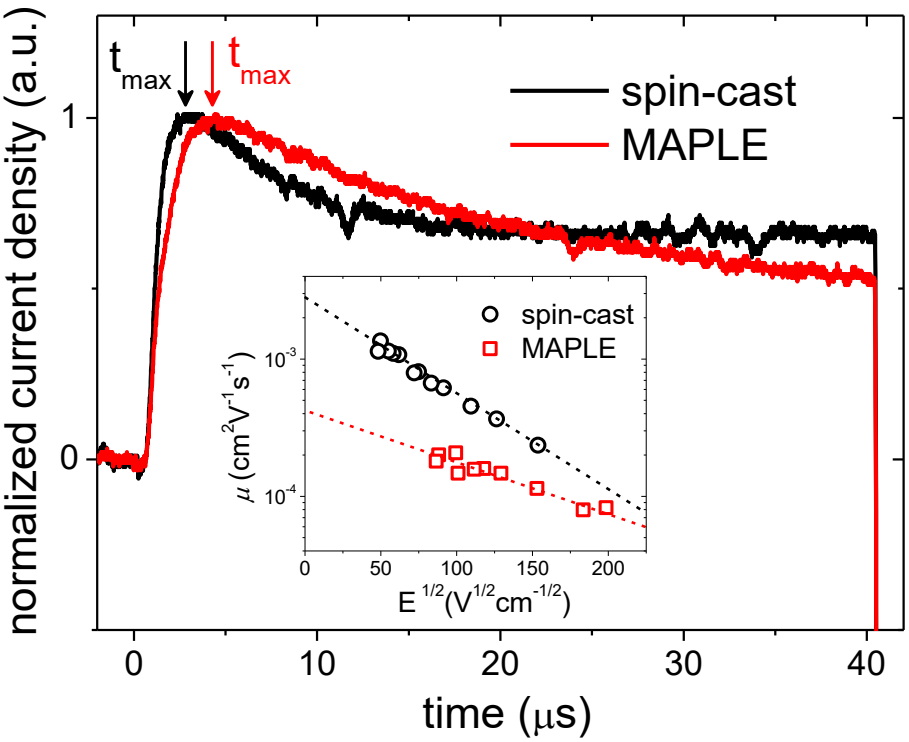

Figure 4.5 Representative current transients measured by CELIV for spin-cast and MAPLE-deposited P3HT films (ramping rate A = 25,000 V/s), and inset showing the electric field dependence of carrier mobilities.

We can rationalize these trends using the well-established Gaussian Disorder Model (GDM), which describes carriers traversing through an environment characterized by both positional and energetic disorder.[32] In a system with a high degree of positional disorder, there exist both fast (high mobility) and slow (low mobility) carrier transport pathways. Due to their structural anisotropy, semicrystalline morphologies, and the presence of both intramolecular and intermolecular transport mechanisms, conjugated polymers are almost always dominated by positional disorder. At low fields, it is more favorable for carriers to travel along fast pathways through strongly-coupled transport sites with low energetic barriers, even if it requires following longer, more tortuous routes. Under higher electric fields, however, carriers are increasingly forced to travel along more direct but energetically unfavorable pathways, leading to a lower mobility and hence the negative dependence of the mobility on electric field.[28,33,34]

Energetic disorder, on the other hand, is associated with electrostatic effects and a broadening of the density of states, originating from a distribution of conjugation lengths arising from distortions in the polymer backbone. When energetic disorder is dominant, the applied external field lowers the activation energy for forward hopping of carriers, resulting in a positive dependence of carrier mobility on electric field. The negative field dependence of mobility in the MAPLE-deposited P3HT sample indicates that positional disorder remains dominant, but the weaker dependence compared to the spin-cast sample may reflect a higher degree of energetic order. This would be consistent from the disorder parameter σ obtained from the Spano analysis of the optical absorption, as well as the higher trap densities suggested by the larger threshold voltages in the TFT output characteristics.

Returning to the out-of-plane carrier mobilities, the zero-field mobility $\mu_{E=0}$ of the MAPLE-deposited sample was extrapolated to be 4.1 x 10^{-4} $cm^2V^{-1}s^{-1}$, nearly an order of

magnitude lower than that of the spin cast sample (2.7 x 10^{-3} $cm^2V^{-1}s^{-1}$). This is a marked contrast to the comparable or even slightly higher in-plane mobilities measured in TFTs. As previously noted, this apparently divergent trend could be a direct consequence of the differences between the two measurement techniques. Unlike TFT measurements, in which carrier density is greatly enhanced within transport region near the dielectric interface, CELIV extracts intrinsic carriers throughout the bulk of the film. Since the effective carrier densities are much lower in the CELIV measurement of the out-of-plane mobilities, there would be correspondingly higher densities of unfilled trap states that impede carrier transport. Another reason for lower out-of-plane mobilities in the MAPLE-deposited samples could be that the polymer chains adopt orientations predominantly parallel to the substrate. Under this scenario, out-of-plane carrier migration relies more heavily upon interchain transport, which is more sensitive to structural disorder than intrachain transport.[35,36] Given the evidence of more disordered morphologies produced by MAPLE deposition, it follows that the out-of-plane transport in these films would be impacted more significantly than the spin-cast analogues. We attempted to characterize the backbone orientations of MAPLE-deposited P3HT films using spectroscopic ellipsometry, but the high surface roughness complicated data modeling/interpretation.[34] In future experiments, we plan to improve film smoothness and increase the size of the multi-sample analysis of optical constants.

4.3. CONCLUSIONS

We deposited thin films of P3HT using emulsion-based RIR-MAPLE, and took advantage of the unique resulting morphologies to study the effect of structural disorder, on both in- and out-of-plane charge transport. Optical spectroscopy and carrier transport measurements all show signatures of higher degrees of energetic disorder in MAPLE-deposited films compared

to the spin-cast analogues. Interestingly, the increased disorder did not reduce the in-plane transistor mobilities, but had a significant detrimental impact on the out-of-plane mobilities. This striking contrast may, in part, be connected to the unequal sensitivities to disorder of intrachain and interchain transport, which have different relative contributions to in-plane versus out-of-plane carrier pathways. We also rationalize the different field-dependencies of out-of-plane carrier transport in terms of the Gaussian Disorder Model, which describes charges traversing through an environment characterized by both positional and energetic disorder. Our findings provide important insight on the effect of disorder on the different mechanisms of charge transport in conjugated polymers.

REFERENCES

1. P. K. Wu, B. R. Ringeisen, J. Callahan, M. Brooks, D. M. Bubb, H. D. Wu, A. Piqué, B. Spargo, R. A. McGill, and D. B. Chrisey: The deposition, structure, pattern deposition, and activity of biomaterial thin-films by matrix-assisted pulsed-laser evaporation (MAPLE) and MAPLE direct write. *Thin Solid Films* **398–399,** 607–614 (2001).
2. A. P. Caricato and A. Luches: Applications of the matrix-assisted pulsed laser evaporation method for the deposition of organic, biological and nanoparticle thin films: a review. *Appl. Phys. A* **105,** 565–582 (2011).
3. R. A. McGill, D. B. Chrisey, A. Pique, and T. E. Mlsna: Matrix-assisted pulsed-laser evaporation (MAPLE) of functionalized polymers: applications with chemical sensors. in **3274,** 255–266 (1998).
4. A. Piqué, R. A. McGill, D. B. Chrisey, D. Leonhardt, T. E. Mslna, B. J. Spargo, J. H. Callahan, R. W. Vachet, R. Chung, and M. A. Bucaro: Growth of organic thin films by the matrix assisted pulsed laser evaporation (MAPLE) technique. *Thin Solid Films* **355–356,** 536–541 (1999).
5. D. B. Chrisey, Piqué A., R. A. McGill, J. S. Horwitz, B. R. Ringeisen, D. M. Bubb, and P. K. Wu: Laser Deposition of Polymer and Biomaterial Films. *Chem. Rev.* **103,** 553–576 (2003).
6. Y. Guo, A. Morozov, D. Schneider, J. W. Chung, C. Zhang, M. Waldmann, N. Yao, G. Fytas, C. B. Arnold, and R. D. Priestley: Ultrastable nanostructured polymer glasses. *Nat. Mater.* **11,** 337–343 (2012).
7. K. B. Shepard, Y. Guo, C. B. Arnold, and R. D. Priestley: Nanostructured morphology of polymer films prepared by matrix assisted pulsed laser evaporation. *Appl. Phys. A* **110,** 771–777 (2013).
8. A. Gutiérrez-Llorente, G. Horowitz, R. Pérez-Casero, J. Perrière, J. L. Fave, A. Yassar, and C. Sant: Growth of polyalkylthiophene films by matrix assisted pulsed laser evaporation. *Org. Electron.* **5,** 29–34 (2004).
9. R. Pate, K. R. Lantz, and A. D. Stiff-Roberts: Tabletop Resonant Infrared Matrix-Assisted Pulsed Laser Evaporation of Light-Emitting Organic Thin Films. *IEEE J. Sel. Top. Quantum Electron.* **14,** 1022–1030 (2008).
10. R. D. McCormick, J. Lenhardt, and A. D. Stiff-Roberts: Effects of Emulsion-Based Resonant Infrared Matrix Assisted Pulsed Laser Evaporation (RIR-MAPLE) on the Molecular Weight of. *Polymers* **4,** 341–354 (2012).
11. W. Ge, A. Atewologun, and A. D. Stiff-Roberts: Hybrid nanocomposite thin films deposited by emulsion-based resonant infrared matrix-assisted pulsed laser evaporation for photovoltaic applications. *Org. Electron.* **22,** 98–107 (2015).
12. J. A. Greer: Design challenges for matrix assisted pulsed laser evaporation and infrared resonant laser evaporation equipment. *Appl. Phys. A* **105,** 661–671 (2011).
13. W. Ge, R. D. McCormick, G. Nyikayaramba, and A. D. Stiff-Roberts: Bulk heterojunction PCPDTBT:PC71BM organic solar cells deposited by emulsion-based, resonant infrared matrix-assisted pulsed laser evaporation. *Appl. Phys. Lett.* **104,** 223901 (2014).
14. E. Leveugle and L. V. Zhigilei: Molecular dynamics simulation study of the ejection and transport of polymer molecules in matrix-assisted pulsed laser evaporation. *J. Appl. Phys.* **102,** 074914 (2007).
15. K. B. Shepard, C. B. Arnold, and R. D. Priestley: Transport and Stability of Laser-Deposited Amorphous Polymer Nanoglobules. *ACS Macro Lett.* **3,** 1046–1050 (2014).

16. K. B. Shepard, C. B. Arnold, and R. D. Priestley: Origins of nanostructure in amorphous polymer coatings via matrix assisted pulsed laser evaporation. *Appl. Phys. Lett.* **103,** 123105 (2013).
17. F. C. Spano: Modeling disorder in polymer aggregates: The optical spectroscopy of regioregular poly(3-hexylthiophene) thin films. *J. Chem. Phys.* **122,** 234701 (2005).
18. F. C. Spano: Absorption in regio-regular poly(3-hexyl)thiophene thin films: Fermi resonances, interband coupling and disorder. *Chem. Phys.* **325,** 22–35 (2006).
19. J. Clark, J.-F. Chang, F. C. Spano, R. H. Friend, and C. Silva: Determining exciton bandwidth and film microstructure in polythiophene films using linear absorption spectroscopy. *Appl. Phys. Lett.* **94,** 163306 (2009).
20. J. Gierschner, Y.-S. Huang, B. V. Averbeke, J. Cornil, R. H. Friend, and D. Beljonne: Excitonic versus electronic couplings in molecular assemblies: The importance of non-nearest neighbor interactions. *J. Chem. Phys.* **130,** 044105 (2009).
21. F. C. Spano and C. Silva: H- and J-Aggregate Behavior in Polymeric Semiconductors. *Annu. Rev. Phys. Chem.* **65,** 477–500 (2014).
22. F. Dinelli, M. Murgia, P. Levy, M. Cavallini, F. Biscarini, and D. M. de Leeuw: Spatially Correlated Charge Transport in Organic Thin Film Transistors. *Phys. Rev. Lett.* **92,** 116802 (2004).
23. A. Salleo, R. J. Kline, D. M. DeLongchamp, and M. L. Chabinyc: Microstructural Characterization and Charge Transport in Thin Films of Conjugated Polymers. *Adv. Mater.* **22,** 3812–3838 (2010).
24. R. Joseph Kline, M. D. McGehee, and M. F. Toney: Highly oriented crystals at the buried interface in polythiophene thin-film transistors. *Nat. Mater.* **5,** 222–228 (2006).
25. H. Sirringhaus: 25th Anniversary Article: Organic Field-Effect Transistors: The Path Beyond Amorphous Silicon. *Adv. Mater.* **26,** 1319–1335 (2014).
26. S. Himmelberger and A. Salleo: Engineering semiconducting polymers for efficient charge transport. *MRS Commun.* **FirstView,** 1–13 (2015).
27. G. Juška, K. Arlauskas, M. Viliūnas, and J. Kočka: Extraction Current Transients: New Method of Study of Charge Transport in Microcrystalline Silicon. *Phys. Rev. Lett.* **84,** 4946–4949 (2000).
28. B. Huang, E. Glynos, B. Frieberg, H. Yang, and P. F. Green: Effect of Thickness-Dependent Microstructure on the Out-of-Plane Hole Mobility in Poly(3-Hexylthiophene) Films. *ACS Appl. Mater. Interfaces* **4,** 5204–5210 (2012).
29. P. W. M. Blom, M. J. M. de Jong, and J. J. M. Vleggaar: Electron and hole transport in poly(p-phenylene vinylene) devices. *Appl. Phys. Lett.* **68,** 3308–3310 (1996).
30. T. Kirchartz: Influence of diffusion on space-charge-limited current measurements in organic semiconductors. *Beilstein J. Nanotechnol.* **4,** 180–188 (2013).
31. G. Juška, K. Arlauskas, M. Viliūnas, K. Genevičius, R. Österbacka, and H. Stubb: Charge transport in π-conjugated polymers from extraction current transients. *Phys. Rev. B* **62,** R16235–R16238 (2000).
32. H. Bässler: Charge Transport in Disordered Organic Photoconductors a Monte Carlo Simulation Study. *Phys. Status Solidi B* **175,** 15–56 (1993).
33. A. J. Mozer and N. S. Sariciftci: Negative electric field dependence of charge carrier drift mobility in conjugated, semiconducting polymers. *Chem. Phys. Lett.* **389,** 438–442 (2004).
34. B. X. Dong, B. Huang, A. Tan, and P. F. Green: Nanoscale Orientation Effects on Carrier Transport in a Low-Band-Gap Polymer. *J. Phys. Chem. C* **118,** 17490–17498 (2014).

35. R. Noriega, J. Rivnay, K. Vandewal, F. P. V. Koch, N. Stingelin, P. Smith, M. F. Toney, and A. Salleo: A general relationship between disorder, aggregation and charge transport in conjugated polymers. *Nat. Mater.* **12,** 1038–1044 (2013).
36. S. A. Mollinger, B. A. Krajina, R. Noriega, A. Salleo, and A. J. Spakowitz: Percolation, Tie-Molecules, and the Microstructural Determinants of Charge Transport in Semicrystalline Conjugated Polymers. *ACS Macro Lett.* 708–712 (2015). doi:10.1021/acsmacrolett.5b00314

CHAPTER V:
CONCLUSIONS

5.1. SUMMARY

Conjugated polymers are a fascinating class of organic semiconductors, adopting diverse and complex morphologies which give rise to correspondingly complicated physical behaviors, particularly those associated with optical and electronic properties. The research presented in this dissertation is unified in the exploration of fundamental relationships between structure and charge transport, at varied length scales, in conjugated polymer-based thin films. Creative and unconventional strategies were utilized to create novel morphologies that served as model systems to experimentally probe deep scientific questions. These findings were then rationalized using complementary results from theory and simulation drawn from the existing knowledge base, thereby providing illuminating perspectives and important insights on the underlying physical processes within the context of energy conversion and charge transport.

The central theme of Chapter 2 was tailoring the nano-scale phase-separated morphology of photoactive blends in order to balance charge generation (exciton dissociation) and transport (carrier collection) to maximize overall power conversion efficiency. A novel all-conjugated random copolymer P(3HT-*r*-3HOMT) was employed as a nanostructure-inducing additive in polymer/fullerene blends (P3HT/ICBA) used as the active layer for solar cells. The copolymer's intermediate semicrystalline-amorphous character enabled it to modify polymer-fullerene interactions and enhance short-range phase separation. This yielded a more favorable

morphology retaining nano-scale domains but possessing a more well-defined fibrillar P3HT network and higher purity PCBM-rich phase, which mitigated bimolecular recombination losses. At the same time, the copolymer's surface segregation tendencies led to enrichment of the cathode interface and modification of electronic work functions in that sensitive region. This served to curb the undesirable migration of positive charge carriers to the electron-collecting cathode, thereby suppressing surface recombination. The combined effects of the copolymer on bulk and interfacial morphology yielded a significant improvement in overall power conversion efficiency of solar cell devices from 4.2% to 5.0%.

Going into Chapter 3, the focus shifted from the nano-structured photoactive blends to macroscopically-aligned pure polymer films. By using a creative combination of an epitaxy-inducing solvent additive and a modified off-center spincoating technique, centimeter-scale uniaxial alignment was achieved in fibrous P3HT films. When incorporated into bilayer solar cells, a remarkable degree (hundreds of micrometers) of long-range photocurrent propagation was observed, made possible by exploiting the anisotropic properties of conjugated polymers, maximizing the ability of carriers to follow the most efficient pathways. Both photocurrent and carrier mobilities exhibited only a moderate degree of anisotropy at the macroscopic level, which could be explained by local imperfections that allowed carriers to easily travel between fibers transverse to the overall alignment. These results of this investigation may help guide future endeavors to use directed alignment as an effective strategy to raise the carrier transport capabilities of conjugated polymers to become more competitive with crystalline inorganic semiconductors.

In contrast to the foregoing, Chapter 4 explored charge transport behavior in highly disordered polymer systems. Using the novel vacuum-based deposition technique, MAPLE,

P3HT films were created with fundamentally different types of morphologies compared to spin-cast analogues. In spite of the significantly larger degree of structural disorder in MAPLE-deposited films, the in-plane carrier mobilities of field effect transistors were very comparable to conventionally-cast devices, and were also much less sensitive to the effects of substrate surface treatments. On the other hand, the out-of-plane mobilities, measured by extracting intrinsic carriers, were significantly lower for MAPLE-deposited films than spin-cast counterparts. This unusual ensemble of characteristics is rationalized by the interplay between carrier densities and disorder-induced trap states. This work represents the first thorough experimental study of morphology and charge transport in conjugated polymers fabricated by this new and technologically-relevant strategy, and also provides important perspectives on the extent to which structural disorder impacts different charge transport mechanisms.

5.2. FUTURE WORK

The findings presented in this dissertation provide several important insights into morphology-property relationships in conjugated polymer-based systems, but also raise a number of new questions that warrant further investigation. In the following are outlined several directions for future research projects, some of which are already in progress.

In Chapter 2, it was shown that a random copolymer additive could be used to tailor both bulk and interfacial morphology of thin film blends, yielding significant improvements in solar cell performance. However, the physical underpinnings of the self-organization of the blend are not fully understood, motivating further studies on the phase behavior of these types of polymer/copolymer/fullerene ternary systems. In particular, experimental determination of interaction and χ parameters would provide extremely valuable information. Contact angle and/or viscosity measurements are some methods of obtaining physical values from which these

parameters may be derived, although in some cases the similar chemistries partial miscibility of different components would prohibit a straightforward analysis. Nevertheless, obtaining a stronger grasp of how copolymer chemistry/architecture affects the phase behavior of the host blend could provide a powerful tool for tailoring targeted aspects of the morphology, such as domain sizes, phase purities, and/or interfacial structure, depending on the desired application.

A natural extension to the work on copolymers as structure-modifying additives is to investigate potential copolymers as primary active components. Although the P(3HT-*r*-3HOMT) copolymer presented in Chapter 2 possessed inferior light absorption and conductivity compared to P3HT homopolymer, other moieties may possess more suitable characteristics. For example, the incorporation of selenophene-based monomer units produces copolymers with stronger aggregation tendencies and lower optical bandgaps, conferring solar cell benefits of improved thermal stability and broader spectral coverage, respectively. Furthermore, changing the copolymer architecture (block, random, gradient) results in very different bulk heterojunction morphologies (see Appendix G), which in turn yield very different device performances. Addressing issues such as morphological degradation and spectral absorption are crucial to the long-term viability of polymer solar cells and other devices, adding an element of urgency to further studies on this system. Furthermore, in ternary systems where all species are photoactive, there remain fundamental questions about where/how excitons are created and dissociated, and the subsequent pathways that carriers take through the multiphase blend. Probing these complex problems will require a combination of morphological characterization and dynamic spectroscopic techniques.

As discussed in Chapter 3, imperfections in the “uniaxial” alignment of P3HT fibers reduced the macroscopic anisotropy of photocurrent and carrier mobility, enabling significant

"leakage" transverse to the primary direction. Furthermore, the highly non-uniform fiber structures resulted in sub-optimal contact/coverage with the substrate and/or electrodes. Increasing the degree of uniaxial chain alignment, coupled with improving film smoothness/uniformity, should lead to superior unidirectional carrier transport. Both of these problems could potentially be mitigated by using polymers with liquid crystalline characteristics and lower aggregation tendencies. Besides epitaxy-inducing solvent additives and off-center spincoating, other processing strategies such as contact coating or mechanical rubbing may also be explored. From a scientific standpoint, further investigation of these highly-aligned systems would serve to bridge some gaps between theoretical carrier transport models and experimentally-measured electrical characteristics, and help elucidate the connections between intramolecular, intermolecular, and macroscopic motion of charges in long-chain polymers and macromolecules. In terms of device applications, enhanced long-range transport could be exploited in experiments involving unconventional device architectures such as lateral solar cells, which are not bound by the same constraints as the traditional stacked layer configuration.

The findings on MAPLE-deposited polymers presented in Chapter 4 represent a preliminary investigation connecting disordered morphology and carrier transport, but further questions remain regarding nano-scale and molecular structure of these films such as polymer chain configuration, degree of crystallinity, and crystallite size/orientation, which can have large impacts on local carrier transport. These structural details may be quantified using spectroscopic ellipsometry and X-ray scattering techniques. The MAPLE technique can also be applied to other types of conjugated polymers, such as more recently developed low-bandgap moieties, in which structural disorder produces different effects. As a tool for fabricating polymer films via vacuum deposition rather than casting from solution, the MAPLE technique opens up a host of new

possibilities. Free from the usual constraints of solvent-substrate wettability, films may be deposited upon virtually any surface. As mentioned in Chapter 4, the carrier mobilities of transistors fabricated from MAPLE-deposited films were comparatively insensitive to OTS treatment of substrates. By varying the surface coverage density and types of self-assembling monolayer species, it could be determined whether the morphology and electronic properties of these films remain similar irrespective of the underlying surface. Furthermore, vacuum-based deposition enables the creation of multilayered structures without the need for orthogonal solvents or film transfer techniques. These novel architectures would enable experimental probing of carrier transport at polymer interfaces in ways were never before possible.

In short, the foundations laid by this dissertation should serve as a launching point for many kinds of new and exciting studies on conjugated polymer systems. Combining morphological studies, optoelectronic measurements, and theoretical rationale into a holistic approach may yield new and valuable contributions to the field of polymer semiconductors.

APPENDIX A:
CHEMICAL CHARACTERIZATION OF P3HOMT AND RANDOM COPOLYMER

Reprinted with permission from:

A. Li, J. Amonoo, B. Huang, P. K. Goldberg, A. J. McNeil, P. F. Green: Enhancing photovoltaic performance using an all-conjugated random copolymer to tailor bulk and interfacial morphology of the P3HT:ICBA active layer. *Adv. Func. Mater.* **24(35)**, 5594-5602 (2014).

Table A.1 Summary of P(3HT-*r*-3HOMT) and P3HOMT chemical information

species	M_n [kDa]	PDI	x_{3HT} [%]	x_{3HOMT} [%]	regioregularity [%]
P3HOMT	16.2	2.19	0	100	97
P(3HT-*r*-3HOMT)	38.0	1.99	39	61	98

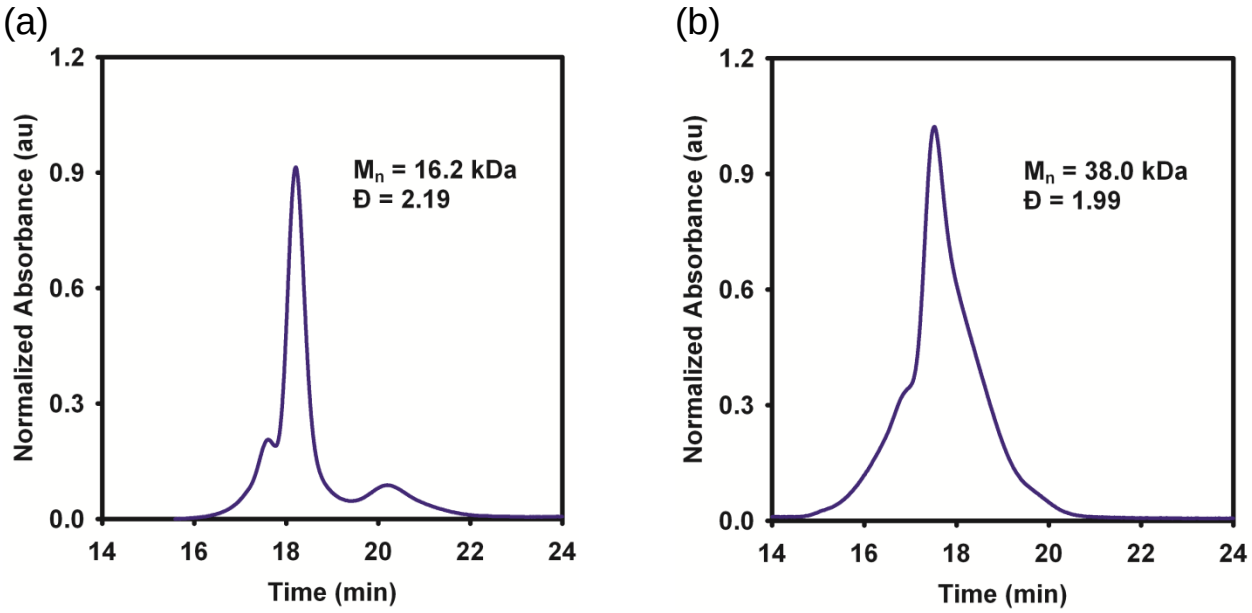

Figure A.1 GPC of P3HOMT (a) and P(3HT-r-3HOMT) (b).

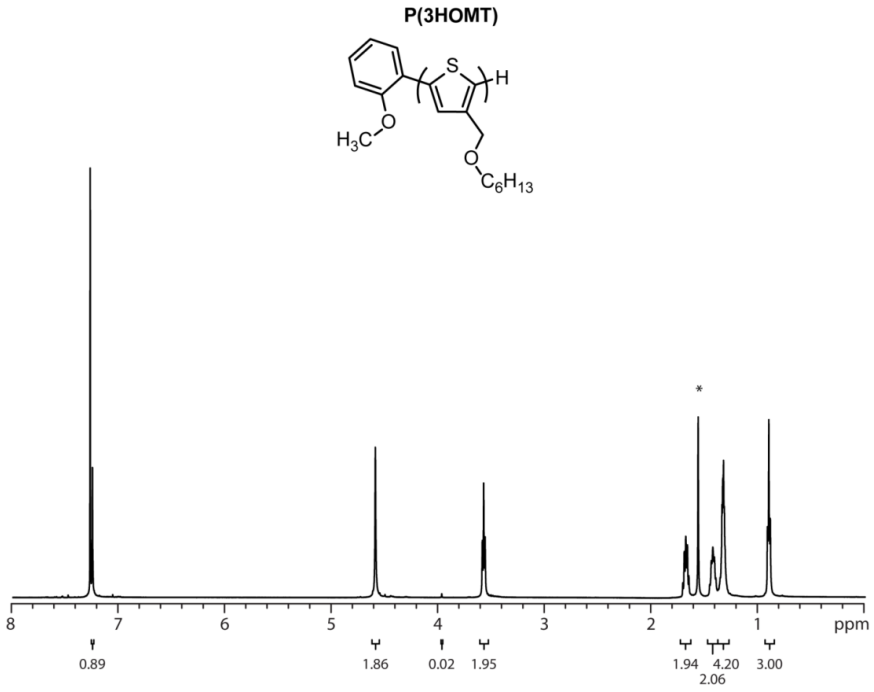

Figure A.2 1H NMR spectrum of P3HOMT: 1H (500 MHz, CDCl3) δ 7.24 (s, 1H), 4.58 (s, 2H), 3.98 (s, 0.02H), 3.57 (t, 2H), 1.68 (m, 2H), 1.42 (m, 2H), 1.32 (m, 4H), 0.89 (br, 3H). * denotes residual H2O

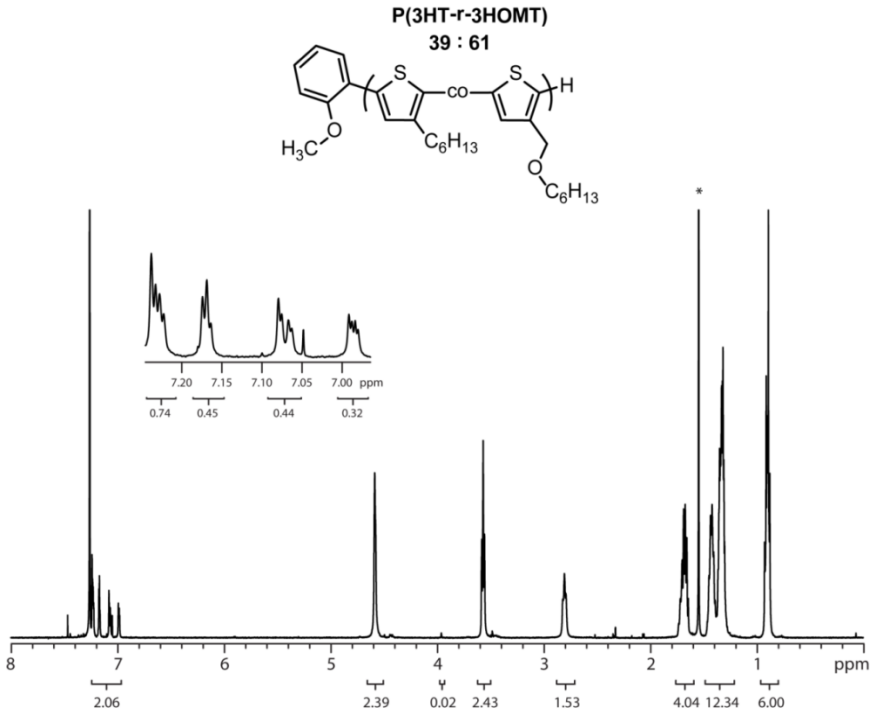

Figure A.3 ^{1}H NMR spectrum (bottom) of P(3HT-*r*-3HOMT): ^{1}H (500 MHz, $CDCl_3$) δ 7.24-6.98 (m, 2H), 4.58 (s, 2.4H), 3.98 (s, 0.02H), 3.57 (t, 2.4H), 2.81 (t,1.6H), 1.68 (m, 4H), 1.55-1.30 (br m, 12H), 0.90 (br, 6H), * denotes residual H_2O

APPENDIX B:
ENERGY-FILTERED TRANSMISSION ELECTRON MICROSCOPY

Energy-filtered transmission electron microscopy (EFTEM) is a powerful technique for generating image contrast in organic thin films, in which different chemical components are carbon-based (making it difficult to distinguish between different domains/phases using conventional TEM techniques). The majority of electrons are elastically scattered by matter; this makes up the dominant portion of the collected scattering intensity for bright-field TEM. Some electrons, however, undergo inelastic scattering with the matter, giving each material a unique electron energy loss spectrum (EELS). The elastically-scattered electrons produce a strong and sharp zero-loss peak, whereas ionization of electrons in core shells of atoms give rise to distinctive edges at high energy losses (useful for elemental mapping). Within the low loss regime is a broad peak(s) corresponding to plasmon resonances with molecular bonds. In some blends of polymers and other organic compounds, the plasmon peaks of the individual components are sufficiently different to allow distinguishing regions that are richer in one component or the other. Rather than collecting the entire spectrum of scattered electrons, EFTEM selectively collects those within a specific energy loss range. This is can be accomplished using a magnetic prism to stratify electrons exiting the column based on their energies; a slit positioned in front of the detector allows only those electrons of the selected energy range to pass through. By judicious selection of energy loss windows, it is possible to collect scattering contrast based on the heterogeneous composition of the polymer blend.

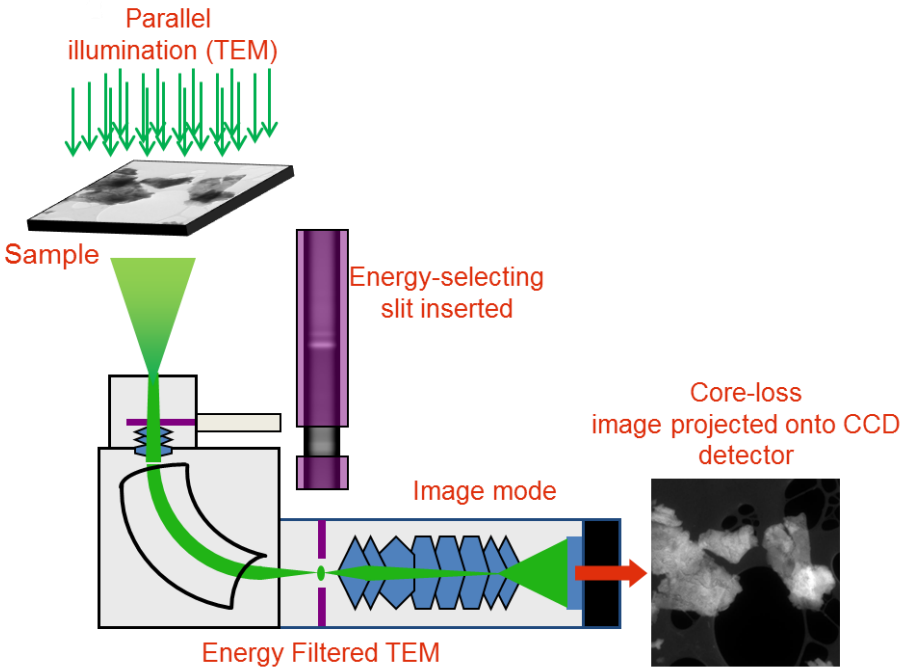

Figure B.1 Diagram of EFTEM configuration (http://www.gatan.com/techniques/eelseftem)

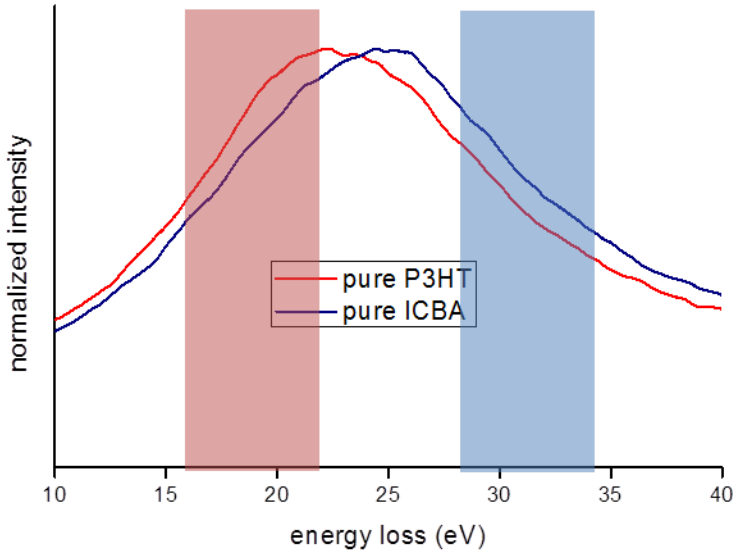

Figure B.2 Example of the offset plasmon peaks in the EELS of P3HT and ICBA. In the 16-22 eV energy loss range (shaded in red), P3HT scatters more strongly; in the 28-34 eV range, ICBA scatters more strongly. By taking images in one of these windows or the other, it is possible to generate image contrast in phase-separated blends.

APPENDIX C:
KELVIN PROBE FORCE MICROSCOPY

Reprinted (in part) with permission from:

A. Li, J. Amonoo, B. Huang, P. K. Goldberg, A. J. McNeil, P. F. Green: Enhancing photovoltaic performance using an all-conjugated random copolymer to tailor bulk and interfacial morphology of the P3HT:ICBA active layer. Adv. Func. Mater. **24(35)**, 5594-5602 (2014).

Kelvin probe force microscopy (KPFM) was used to map the surface potentials of P3HT:ICBA active layers for solar cells, as discussed in Chapter 2. The surface potentials are directly related to electronic work functions, which depending on nature of the underlying substrate, can be translated into effective HOMO or LUMO values. Below are the raw topography and surface potential maps for blends with and without the addition of random copolymer P(3HT-*r*-3HOMT) on substrates treated with high work function and low work function surface modifiers. The distribution of surface potentials across the images are plotted in the histogram in Figure 2.8.

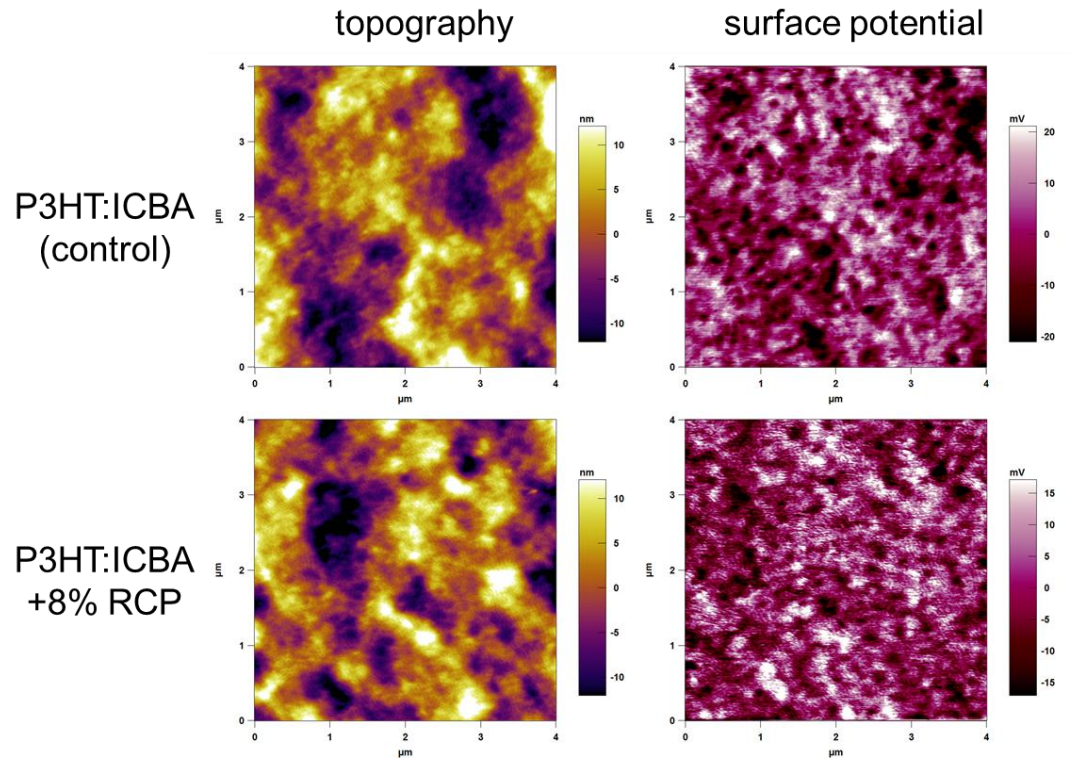

Figure C.1 Topography and surface potential maps (4 x 4 µm) of samples prepared on high work function ITO/PEDOT:PSS; surface potential values relate to effective HOMO levels.

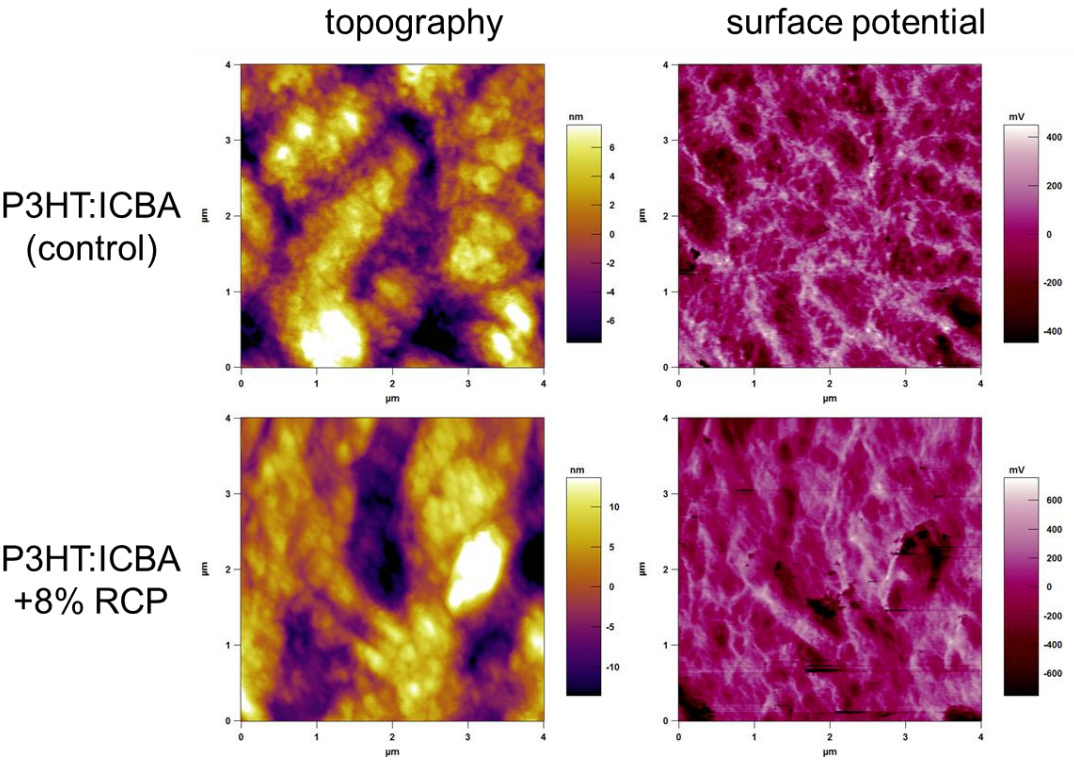

Figure C.2 Topography and surface potential maps (4 x 4 µm) of samples prepared on low work function ITO/PEIE; surface potential values relate to effective LUMO levels.

APPENDIX D:
THIN FILM TRANSISTOR TRANSFER CURVES

(a)

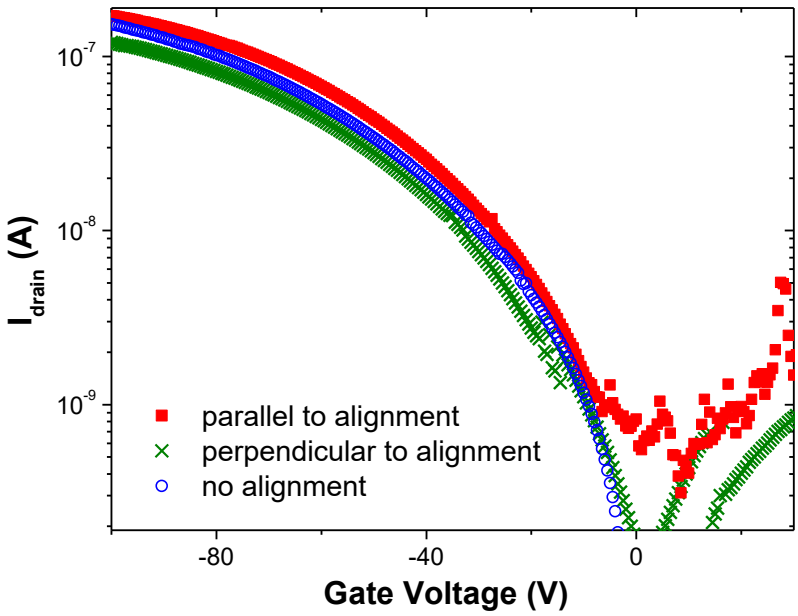

(b)

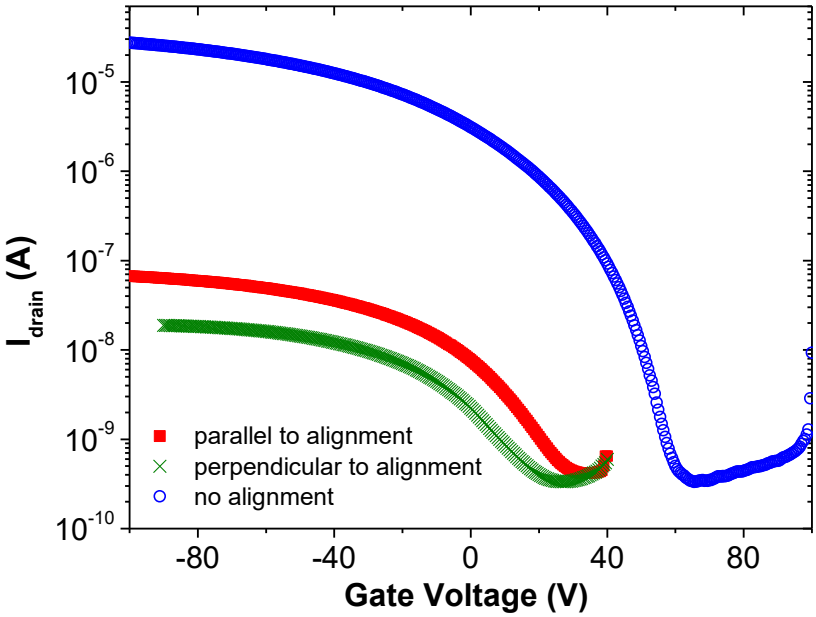

Figure D.1 Transfer curves from TFT measurements of directly-cast (a) and transferred (b) P3HT films.

APPENDIX E:
SPANO MODEL FOR UV-VIS ABSORPTION

The absorption spectrum of P3HT can be divided into contributions from two sources: a set of narrow absorption peaks at lower energies from π-stacked aggregates (interchain state), and a broad absorption at higher energies from the amorphous component (intrachain state). Within the limit of weak excitonic coupling, the cofacial interchain interactions of adjacent conjugated segments in P3HT leads to a formation of vibronic bands, which can be determined by applying the Frank-Condon principle according to the equation:

$$A_{\text{aggregate}} \propto \sum_{m=0} \left(\frac{S^m}{m!}\right) \times \left[1 - \frac{We^{-S}}{2E_{\text{p}}} \sum_{n \neq m} \frac{S^n}{n!\,(n-m)}\right]^2 \times e^{\frac{\left(E - E_0 - mE_0 - \frac{1}{2}WS^m e^{-S}\right)^2}{2\sigma^2}}$$

A is the absorption of the aggregates as a function of photon energy *E*, *S* is Huang-Rhys factor, representing the overlap between vibrational states (assumed to be 1), *m* corresponds to different energy levels, and E_{p} = 0.179 eV is the energy of the C=C symmetric stretch mode. In this equation, the two fitting parameters of interest are the exciton bandwidth *W* and the energetic disorder σ (Gaussian width of the absorption peaks).[1,2]

REFERENCES

1. F. C. Spano: Modeling disorder in polymer aggregates: The optical spectroscopy of regioregular poly(3-hexylthiophene) thin films. *J. Chem. Phys.* 122, 234701 (2005).
2. F. C. Spano: Absorption in regio-regular poly(3-hexyl)thiophene thin films: Fermi resonances, interband coupling and disorder. *Chem. Phys.* 325, 22–35 (2006).

APPENDIX F:
MATRIX-ASSISTED PULSED LASER EVAPORATION

Matrix-assisted pulsed laser evaporation (MAPLE) is a variant of conventional pulsed laser deposition, using a laser as the excitation source to vaporize target material under a high vacuum environment. What distinguishes MAPLE is the use of a frozen dilute solution rather than directly irradiating the material of interest. By choosing a solvent such that the laser is primarily absorbed by the frozen matrix, it is possible to mitigate photochemical degradation to sensitive guest materials such as polymers and other macromolecules. When the target is ablated by the laser, in addition to solvent vapor molecules, liquid ejecta in the form of solvent/polymer clusters are released. The substrates are positioned at a given distance away from the target; the volatile solvent is pumped away under the high vacuum environment during and after the processes of material transport and deposition onto the substrate. The resulting morphologies typically consist of heterogeneous globular features, vestiges of the droplets/clusters ejected by laser ablation.

The initial MAPLE configurations reported in literature primarily employed lasers with UV wavelengths. Later studies indicated that UV lasers possessed enough energy to degrade even dilute polymer guests, either destroying chemical functional groups or fragmenting the polymer chains. To avoid this problem, particularly for conjugated polymers which strongly absorb in the UV and visible range spectrum, it is necessary to select a lower energy wavelength.

For this reason, resonant infrared (RIR) MAPLE is a much gentler and more appropriate subclass of MAPLE for deposition of semiconducting polymers such as P3HT. The Er:YAG laser produces a wavelength of 2.94 μm, which is resonant with the O-H vibrational stretching mode. This makes water the ideal solvent matrix, although alcohols can also be used to a lesser effect. Unfortunately, many polymers of interest are not water-soluble, necessitating a modified strategy for target preparation.

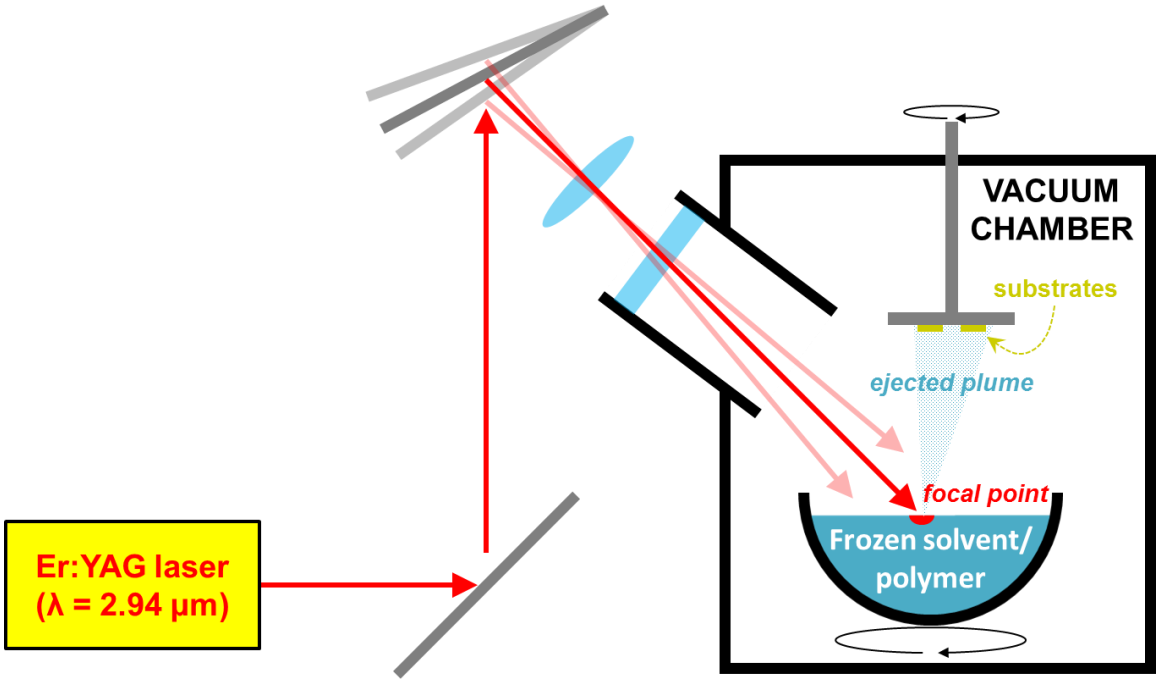

Figure F.1 Schematic diagram of the RIR-MAPLE configuration used to prepare samples described in Chapter 4.

The research group of Professor Adrienne Stiff-Roberts pioneered an emulsion-based RIR-MAPLE technique, wherein the target was prepared by first dissolving the polymer in a good organic solvent, and then mixing it with water and a bare minimum of surfactant to generate a stable emulsion (with sufficient standing time to persist through the time required for freezing).

The recipe used to prepare samples described in Chapter 4 used the following ingredients: (1) P3HT, dissolved at a concentration of 5 mg/mL in 1,2-dichlorobenzene (DCB), (2) Benzyl alchohol (BnOH), and (3) DI water containing 0.005 wt.% sodium dodecyl sulfate (SDS) surfactant. First the BnOH (aids in emulsification) is added to the P3HT/DCB solution at a 1:3 volume ratio. BnOH is a poor solvent for P3HT, so the solution must be heated/swirled to redissolve any aggregates/precipitates. Next, the 0.005% SDS/water solution is added to the mixture, such that the volume ratio of the original P3HT solution to water is 1:4. Immediately afterwards, the scintillation vial is alternately subjected to vigorous agitation and immersion in an ultrasonication bath, until a uniform milky consistency is achieved (typically after a few minutes). A small fraction of clearly visible un-emulsified solution almost always remains, and collects at the bottom of the vial when the solution is left standing. This fraction is not extracted from the vial when injecting solution into the deposition chamber for flash freezing.

APPENDIX G:
EFFECT OF COPOLYMER ARCHITECTURE ON BULK HETEROJUNCTION MORPHOLOGY

Reproduced by permission of The Royal Society of Chemistry:

J. Amonoo, A. Li, B. Huang, G. Purdum, M.E. Sykes, E. F. Palermo, A. J. McNeil, Y.-L. Loo, P. F. Green (2015). An All-Conjugated Gradient Copolymer Approach for Morphological Control of Polymer Solar Cells. *J. Mater. Chem. A* **3**, 20174–20184.

Synthesis of P(3HT-3HS) copolymers was performed using a nickel-catalyzed chain growth mechanism. By controlling the feed-in ratio of monomers, random, block, and gradient copolymer architectures were synthesized.

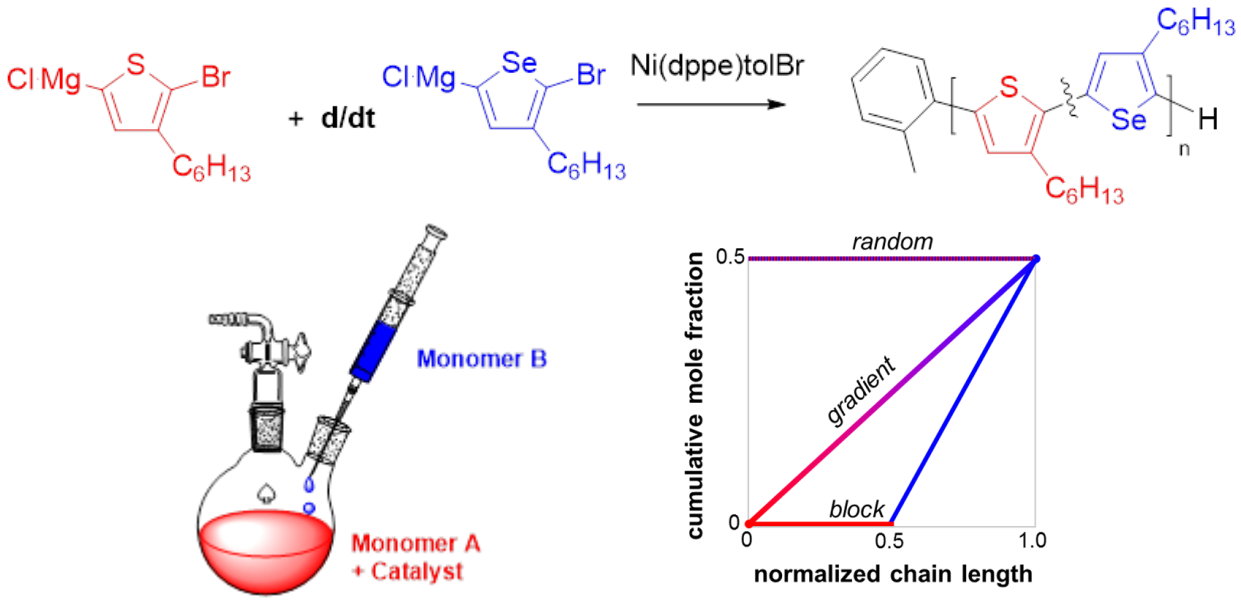

Figure G.1 Synthesis procedure for all-conjugated P(3HT-3HS) copolymers of varying architectures.

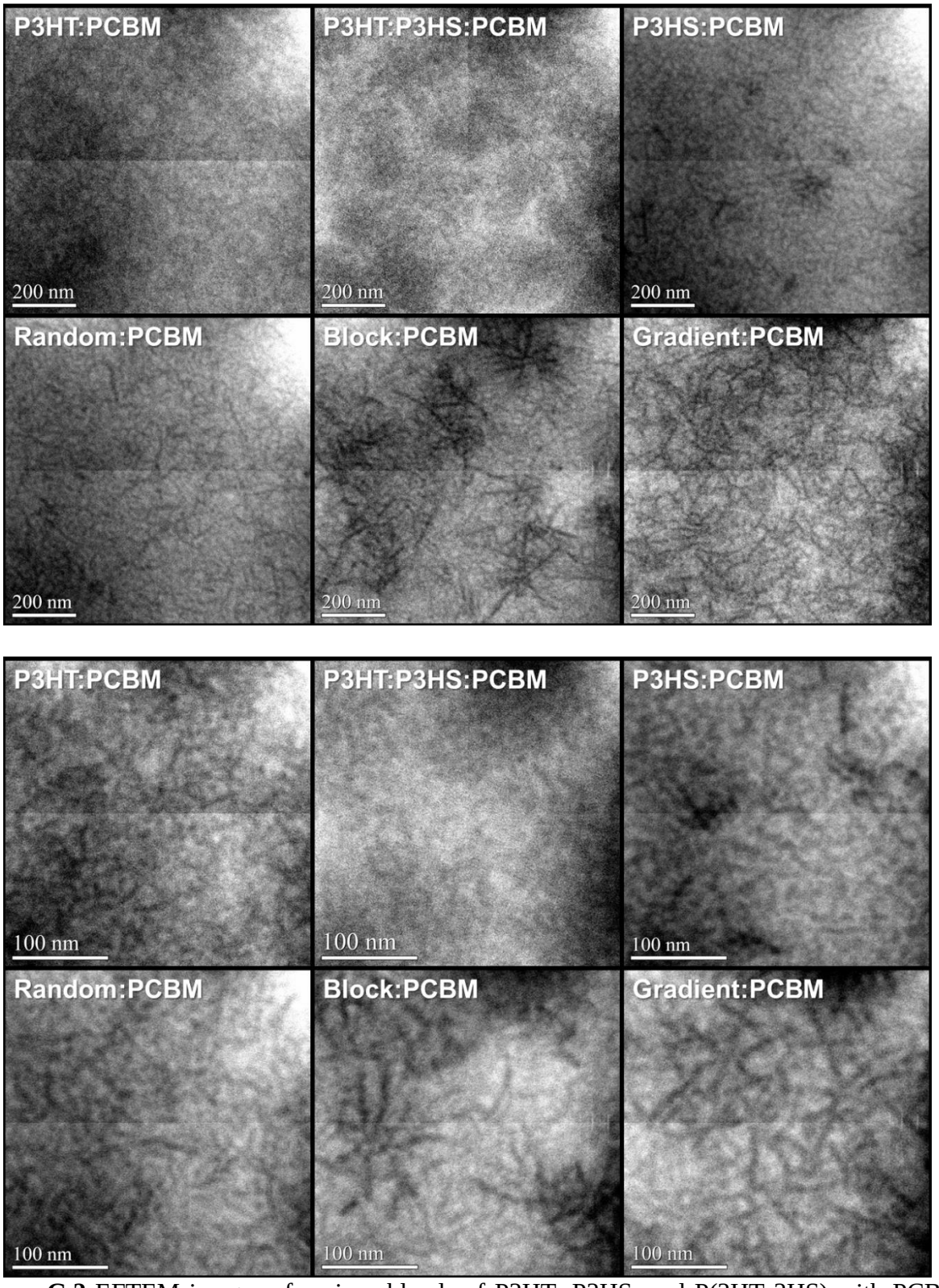

Figure G.2 EFTEM images of various blends of P3HT, P3HS, and P(3HT-3HS) with PCBM. Top and bottom sets of images were taken at lower and higher magnifications (as indicated by the scale bars), respectively.

APPENDIX H:
ACCOUNTING FOR CONTACT RESISTANCE IN ORGANIC FIELD EFFECT TRANSITORS

In organic thin film organic field effect transistors with metallic contacts and inorganic dielectric, the role of contact resistances can greatly increase the error of mobility calculations simply fitting to the linear regime of the square root of the drain current ($I_D^{1/2}$) versus gate voltage (V_G). Indeed, in many cases the contact resistance can exceed the channel resistance (by as much as a factor of 5 to 10), in which case the measured carrier mobilities are indicative of the contacts rather than the organic semiconducting material of interest.[1]

One way to extract contact resistances is the Transfer Line Method (TLM), where the circuit resistance is taken as a sum of the semiconductor resistance and the parasitic resistance R_P (assumed to be the source/drain contacts). The parasitic resistance can be calculated by measuring devices of varying channel lengths and then extrapolating to a channel length of zero. Although the principle is straightforward, fabricating multiple devices of different dimensions can be time-consuming and in some cases prohibitive. An alternative could be to employ KPFM (see Appendix C) to map the surface potentials of the transistor device, thereby directly measuring voltage drops at the source and drain electrodes (from which contact resistances can be calculated).[2]

Once the contact resistances have been found, using one of the previously described or other methods, the mobility μ can be corrected using the equation[3]

$$R_{ON} = \frac{V_D}{I_D} = \frac{L}{\mu W C_i (V_G - V_T)} + R_P$$

Another approach to accounting for contact resistances, as well as gate voltage-dependent mobilities, in OFETs has been developed by Natali et al.,[4] which can be accomplished solely through electrical measurements of a single device, and performing differential analysis of the transfer characteristic curves of drain current versus gate voltage. The mobility is assumed to have a power law dependence on V_G:

$$\mu = \mu_0 (V_G - V_T)^{\gamma}$$

The unknown parameters are μ_0, threshold voltage V_T and power law exponent γ. Accounting for non-Ohmic contacts with source-drain voltage V_D and series of contact resistances R_{SD}, the drain current can be expressed as:

$$I_D = \frac{K V_D (V_G - V_T)^{\gamma+1}}{1 + K R_{SD} (V_G - V_T)^{\gamma+1}}$$

where $K = \mu_0 C_i W/L$. From here, quantities z and w can be defined as

$$z = \frac{{I_D}^2}{I_D'}$$

$$w = \frac{\int_0^{V_G} z \, dV_G'}{z}$$

After a series of mathematical manipulations, it can be shown that

$$z = \frac{K}{\gamma + 1} (V_G - V_T)^{\gamma+2} V_D$$

$$w = \frac{1}{\gamma + 3} (V_G - V_T)$$

As can be seen, if the conditions under which this method is applicable (power law dependence of μ on V_G, constant R_{SD}) are met, w should be linear with a slope between 0 and

1/3, allowing the two unknowns V_T and γ to be easily extracted from a linear fit. These parameters can be substituted back into the expression for z to calculate the mobility μ_0. Lastly, the equation for I_D can be rearranged to solve for R_{SD}:

$$R_{SD} = \frac{V_D}{I_D} - \frac{1}{K(V_G - V_T)^{\gamma+1}}$$

which is effectively the difference between the total device resistance and that of the semiconductor itself $R_{SD} = R_{\text{tot}} - R_{\text{TFT}}$.

REFERENCES

1. H. Klauk, G. Schmid, W. Radlik, W. Weber, L. Zhou, C. D. Sheraw, J. A. Nichols, and T. N. Jackson: Contact resistance in organic thin film transistors. *Solid-State Electron.* **47,** 297–301 (2003).
2. M. J. Panzer and C. D. Frisbie. Contact Effects in Organic Field-Effect Transistors. In Z. Bao and J. Locklin (Eds.), *Organic Field-Effect Transistors*, 139-157, CRC Press (2007).
3. D. Gupta, M. Katiyar, and D. Gupta: An analysis of the difference in behavior of top and bottom contact organic thin film transistors using device simulation. *Org. Electron.* **10,** 775–784 (2009).
4. D. Natali, L. Fumagalli, and M. Sampietro: Modeling of organic thin film transistors: Effect of contact resistances. *J. Appl. Phys.* **101,** 014501 (2007).